Modeling of Hierarchical Solidification Microstructures in Metal Additive Manufacturing: Challenges and Opportunities

Supriyo Ghosh[a,*], Julien Zollinger[b], Miha Zaloznik[b], Dilip Banerjee[c], Christopher K. Newman[d], Raymundo Arroyave[e]

[a]*Department of Metallurgical and Materials Engineering, Indian Institute of Technology, Roorkee, UK 247667, India*
[b]*Equipe solidification, Institut Jean Lamour, Université de Lorraine, Nancy F-54011, France*
[c]*Materials Science and Engineering Division, National Institute of Standards and Technology, Gaithersburg, MD 20899, USA*
[d]*Fluid Dynamics and Solid Mechanics Group (T-3), Los Alamos National Laboratory, Los Alamos, NM 87545, USA*
[e]*Department of Materials Science and Engineering, Texas A&M University, College Station, TX 77843, USA*

Abstract

Metal-based additive manufacturing (AM) processes often produce parts with improved properties compared to conventional manufacturing and metal working routes. However, currently, only a few alloys can be reliably additively manufactured as the vast majority of the alloys in use today are not explicitly designed for this manufacturing route. This is because the highly non-equilibrium nature of melting and rapid solidification phenomena during AM leads to undesirable microstructures with complex growth morphologies and unpredictable microstructural inhomogeneities including solidification defects, leading to unwanted variability in final material properties. In this context, the review article discusses the underlying physical mechanisms of microstructure and associated defects formation during ultrarapid cooling rates typical of AM in order to suggest approaches to minimize and control microstructural heterogeneities for improved printability and microstructure robustness (and hence properties). In particular, the physical effects of cooling rates and alloy parameters on rapidly moving complex solid-liquid interface shapes and the nucleation behavior during non-steady thermal conditions in heterogeneous liquid during AM must be well-understood to control the solidification microstructure and grain morphology. Suitable integration of physics-rich macroscale melt-pool, microstructure, and atomic-scale nucleation models (but benchmarked by experimental measurements) could quantitatively simulate the above hierarchical AM solidification problems that extend across multiple length scales and associated chemical heterogeneities. To address the tremendous computational expense of the above solidification problems toward large part-scale or full-melt-pool simulation, exascale computing hardware and software has been leveraged as a part of the exascale computing project. Further, the AM solidification simulations would guide parameter-microstructure optimization *via* data-driven modeling and, ultimately, alloy and processing development to suit various envisaged applications in the AM community.

Keywords: Additive Manufacturing, Solidification, Dendrite, Eutectic, Peritectic, Defects, Nucleation

*Corresponding author.
Email address: supriyo.ghosh@mt.iitr.ac.in; gsupriyo2004@gmail.com (Supriyo Ghosh)

1. Introduction

Additive manufacturing (AM) processes are among the most rapidly growing technologies that use incremental material addition to build near-net-shape complex material geometries directly from the design (for recent reviews, see [1–3]). In AM of metallic materials, the metal feedstock is often melted using a high-energy heat source to generate a melt-pool, which undergoes rapid solidification and solid-state metallurgical reactions and joins layers of materials on top of each other until the component is complete. Such layer-by-layer processing allows the manufacturing of highly intricate and complex material geometries, which may be impossible to achieve by traditional materials processing methods either by casting, forging, welding, or powder metallurgical processes [4, 5]. Major advantages of AM include the consolidation of multiple parts (less joins between parts), reduced material waste, increased design complexity, and the possibility of customized designs for one-off or unique applications [2–6]. Thus, materials and components made by AM are increasingly becoming pervasive in modern applications, as summarized in Table 1.

Alloys	Key Applications
Ni-based alloys (Inconel 625, Inconel 718)	Gas turbines, Jet engines
Al-based alloys (Al-10Si-Mg)	Consumer, Aerospace, Automotive
Ti-based alloys (Ti-6Al-4V)	Aerospace, Biomedical
Stainless steels (304, 316, 316L, 17–4 PH)	Structural, Automotive

Table 1: Additively manufactured materials are widely used in targeted industrial applications.

The melting of feedstock material leads to melt-pool formation. The subsequent rapid cooling and solidification of the resulting melt-pool play a key role in determining the process-microstructure-property relationships that dictate component performance. In general, the melt-pool solidification conditions control the size, shape, and distribution of the microstructural grains and sub-grains; the growth morphology; the elemental segregation and precipitation; the grain/sub-grain boundary character; the solid-state phase transformation; and ultimately, the properties of the final product. Since AM parts are directly printed from a computer-aided design file using the layer-by-layer build technology, it permits ample opportunities to tailor the solidification microstructures required for a given application [7, 8]. Typical applications of tailored microstructures produced *via* AM include: (a) eutectic solidification-based nanoporous microstructures can be used as catalysts in compact reactors for H_2 production; (b) tailored heterogeneous solidification microstructures may allow for customizing materials properties and increasing the usage of lightweight parts primarily in aerospace and automotive sectors, reducing mass and fuel consumption; and (c) AM at the fidelity of the custom as-printed microstructures may bring possibilities of realizing novel properties beyond traditional approaches and materials [7, 9, 10]. Remarkably, these unique as-solidified microstructures could potentially negate the need for post-AM operations such as heat treatment, as they are intentionally designed

through computer models grounded in a profound understanding of the solidification mechanism. Therefore, predicting and controlling the solidification microstructure evolution during AM is essential.

Differing by the feedstock material (powder or wire) and heat source (laser, electron beam, or arc), metal-AM processes are broadly categorized as directed energy deposition (DED) and powder bed fusion (PBF). Typical solidification microstructures that result in these AM variants reveal predominantly inhomogeneous, extremely-fine columnar and cellular features extending across multiple solidified melt-pool layers that are primarily attributed to rapid solidification followed by the addition of material in a layer-by-layer fashion (Fig. 1). Due to the considerable similarities in microstructural processes in different metal-AM processes, and given that our aim is to review simple yet effective general approaches to predict and control solidification microstructures under rapid AM conditions, we primarily focus on a laser powder bed fusion (LPBF) metal-AM process.

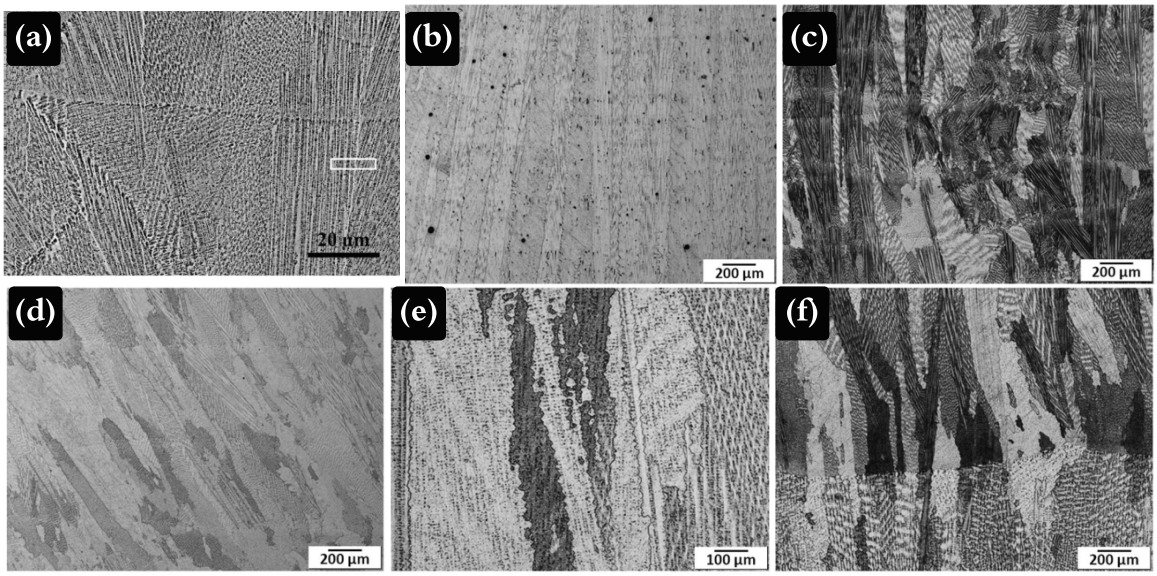

Figure 1: As-solidified microstructures of Inconel alloys that result in common fusion-based metal-AM processes: (a) Laser powder bed fusion (LPBF), (b) Electron beam powder bed fusion (EB-PBF), (c) Laser powder directed energy deposition (LP-DED), (d) Laser wire DED, (e) Wire arc DED, and (f) Electron beam wire DED. In all the images, build direction is vertical. Note that scales in the images vary to provide the best definition of the solidification microstructure. (a) is reproduced from [11], with permission from Elsevier. (b)-(f) are reproduced from [12] (open access).

The cooling rate and thus the production of components in AM depend on several factors including laser power, laser scanning speed, and laser scanning pattern. In the literature, the effect of these parameters on melt-pool solidification is widely reported. However, the limited information in each study regarding the laser processing parameters, the AM system used, and the part geometry fabricated makes it challenging to compare these studies. However, some general trends observed in the literature are as follows:

- As laser melts the feedstock, the resultant thermal history leads to directional solidification along the edge of the radius of the melt-pool, resulting in microstructure formation. The laser parameters (laser

power P and laser scan speed V) are microscopically linked to location-specific solidification conditions – temperature gradient G and solidification rate or solid-liquid interface growth velocity R (Fig. 2a). Thus, the directional cooling rate is often expressed by $\dot{T} = GR$.

- Solidification occurs with a rapid cooling rate (10^3 K/s to 10^8 K/s) that increases with laser parameters (P and V) and produces extremely fine-grained microstructures (nanometers to micrometers) (Fig. 2b).

- For a given alloy, the solidification parameter G/R determines the solidification mode or the solid-liquid interface morphology in AM. Solidification starts with a planar solid-liquid interface at the bottom of the melt-pool due to the high value of G/R ratio in this region and, as solidification proceeds, the interface evolves through a cellular to a dendritic and, eventually, to an equiaxed morphology due to the decrease of that ratio (Figs. 2b, 2c). Hence, G/R is often referred to as the morphology factor.

- AM solidification is a non-equilibrium phenomenon that leads to departure from local equilibrium conditions at the solid-liquid interface, resulting in microstructural heterogeneities such as microsegregation and formation of potentially harmful segregated intermetallic phases in the solid solution (Fig. 2d).

- As-deposited microstructures often possess higher yield and ultimate tensile strengths and reduced ductility when compared to the wrought or as-cast versions of the same alloy. The increase in strength is primarily due to the fine microstructure developed by high cooling rates in AM. The reduced ductility is primarily due to the typical trade-off between strength and ductility and the presence of internal defects in AM materials.

- The as-solidified microstructures often undergo solution heat treatment, such as annealing, to dissolve the desired/undesired segregated phases that develop during the late stages of solidification in order to modify the size, shape, and distribution of the final solid phases for improved properties such as ductility.

It is evident from the above discussion that laser AM processing enables manufacturing products from microstructurally complex solidified melt-pool. However, to meet the full potential that metal-based AM techniques can offer and the advances it has undergone over the past two decades, significant gaps are yet to be bridged in order to bring it to full maturity. The melt-pool solidification is characterized by a complex interplay of several chemical (phase transformations), physical (species diffusion), thermal (heat diffusion), and mechanical (residual stresses) phenomena, which occur across different length and time scales, leading to diverse microstructures [2, 3, 16]. Therefore, the solidification processes in AM are of hierarchical nature (Fig. 3). In which, the macroscale processes include the effect of process parameters at the scale of the melt-pool; mesoscale processes consist of phase transformations and grain structure evolution;

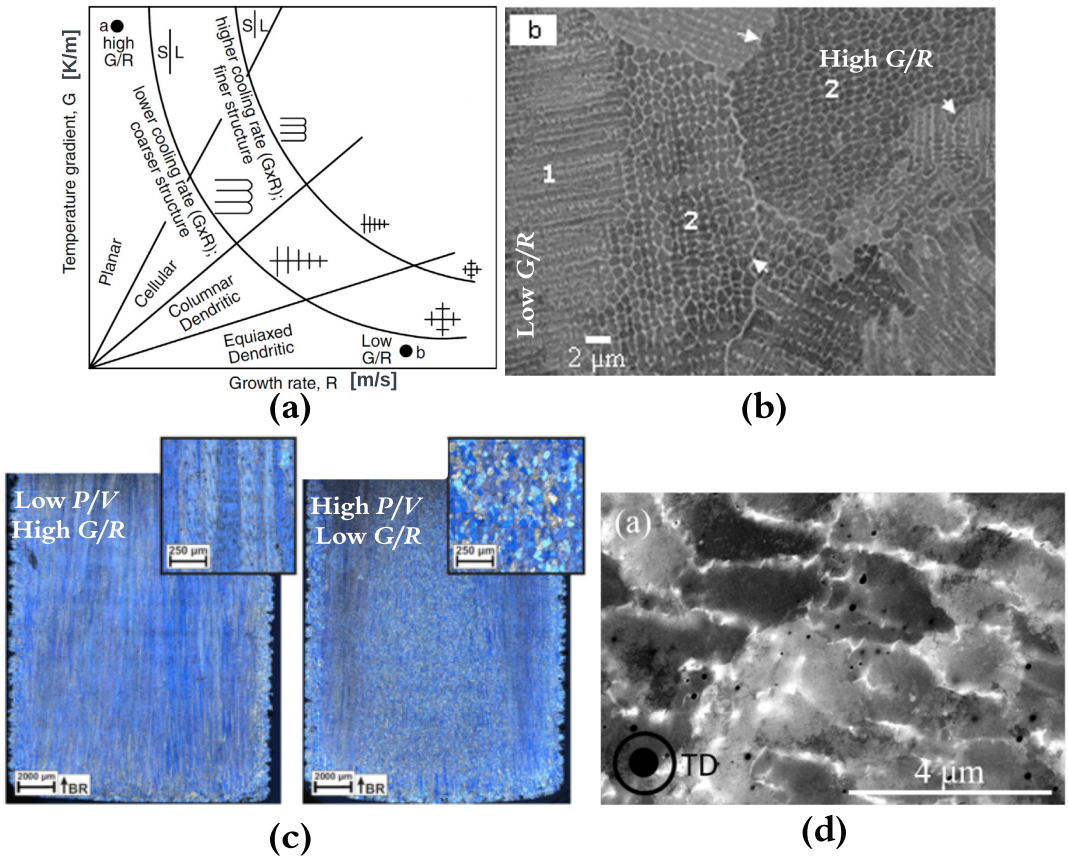

Figure 2: (Color online) (a) Schematically shown how a given combination of G and R determines the growth morphology and grain size. Increasing the cooling rate (GR) refines the solidification morphology. (b) Scanning electron microscopy (SEM) image shows the solidified melt-pool (grain and sub-grain) microstructural characteristics during the LPBF of an Inconel 718 alloy. The sub-grain cellular (region 1) and dendrite (region 2) morphologies are commonly observed within each solidified grain. The grain boundary (shown by arrows) separates grains with different orientations of the sub-grain-scale features (reproduced from [13], with permission from Elsevier). (c) The columnar-to-equiaxed transition (CET) results by increasing the laser process parameter P/V and/or decreasing the solidification parameter G/R (from [14]). (d) Field emission SEM image shows a typical cellular microstructure in which the interdendritic secondary phases (brightest features) form by microsegregation appear along the cellular sub-grain boundary (reproduced from [15], with permission from Elsevier).

and micro-to-atomic-scale processes influence the sub-grain-scale micro/nanostructure evolution, precipitate formation, diffusion behavior, interface structure, and nucleation and grain refinement mechanisms. The above physical effects, spanning from nanometer to sub-millimeter, have significant impact on the resulting hierarchical solidification microstructure and mechanical behavior of the material, as demonstrated experimentally in Refs. [7, 17, 18]. Despite such importance, the effects and interaction of the above hierarchical multiphysics events during AM solidification have seldom been studied in a comprehensive manner. Recently, the above complex AM solidification problems have been included as a critical challenge problem in the ExaAM project [19, 20], an initiative within the Exascale computing project (ECP) to conduct high-performance numerical simulations by leveraging exascale computing hardware and software to model process-microstructure-property relationships. In this review article, we highlight the critical role of the mi-

cro/nanostructure formation during AM solidification, aiming to identify research tasks that could be used, among others, to determine the optimal process, solidification, and printability maps for enabling improved process-microstructure-property correlations in AM of metals.

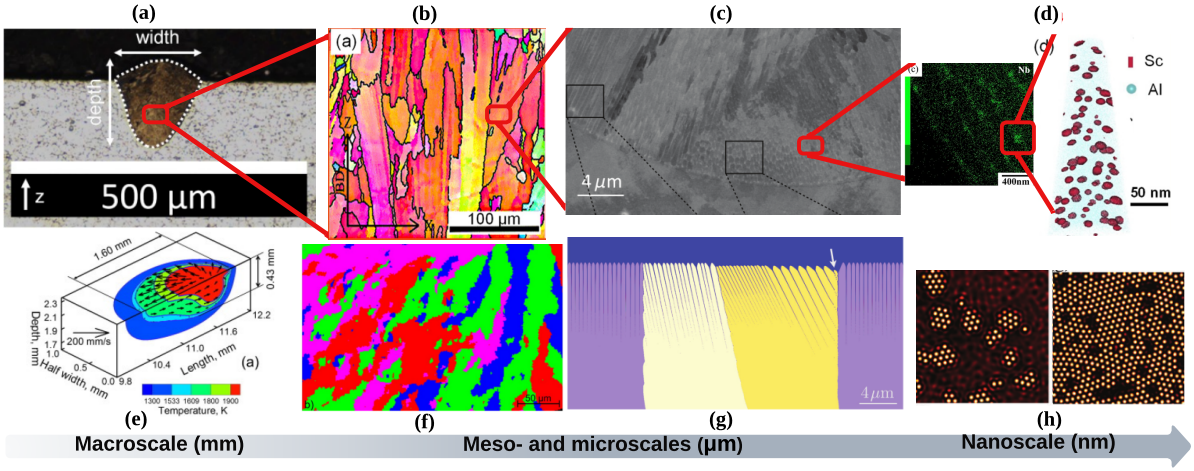

Figure 3: (Color online) Hierarchical nature of the solidification process is presented in the context of microstructure evolution in experiments (top row) and simulations (bottom row) during AM of an Inconel 718 alloy. The hierarchical nature of as-solidified microstructures was investigated through multiscale characterization techniques, including optical microscopy (OM), scanning electron microscopy (SEM), electron backscatter diffraction (EBSD), and transmission electron microscopy (TEM). (a) At the macroscopic scale, melt-pool results during the laser melting process (reproduced from [21], with permission from Elsevier). z is the AM build direction. (b) At the mesoscale, a primary columnar grain structure results due to melt-pool solidification (reproduced from [22], with permission from Elsevier). BD is the build direction. (c) Typical sub-grain-scale cellular and dendritic microstructures are observed in solidified melt-pool (reproduced from [23], with permission from APS). (d) At the atomic scale, interdendritic secondary phases form due to heavy microsegregation during the last stages of solidification (reproduced from [24], with permission from Elsevier) followed by nanoprecipitates formation in the matrix of the primary solidification phase (reproduced from [22], with permission from Elsevier). (e) The temperature distribution and mechanical history during melt-pool solidification can be predicted using a macroscale finite element analysis model (reproduced from [25], with permission from Elsevier). (f) The grain structure in AM is predicted using a cellular automata-finite element (CAFE) model (from [26]). (g) The far-from-equilibrium sub-grain morphologies are quantitatively predicted by a phase-field model (reproduced from [23], with permission from APS). (h) The late stage solidification processes, including the nucleation and growth of secondary phases and subsequent precipitation processes can be predicted, among other approaches, by a phase-field crystal method (reproduced from [27], with permission from Taylor & Francis). Integrating advanced simulation and high-performance computing (HPC) tools will rapidly enable mapping and predicting these hierarchical solidification phenomena at relevant scales.

Another major roadblock in AM is the high degree of variability in the microstructure of the fabricated metal parts, which pose severe challenges to the qualification and certification of critical AM components. This is due to AM-specific microstructural inhomogeneities, solidification defects, and other unique microstructural features not common in traditional manufacturing methods [5]. One of the possible reasons for this variability is the fact that a large portion of prior works on metal AM have focused only on a handful of major material systems (Table 1), with the bulk of focus on titanium, nickel, and stainless steels and other specific alloy systems that were not initially designed to be manufactured using AM technologies. Many of the alloy systems in use today are not necessarily suitable for AM processing because of the complex and highly non-equilibrium nature of melt-pool solidification. Consequently, they become highly sensitive

to variations in location-related solidification conditions, which often introduce unwanted variability in the final microstructure and material properties. Since solidification is the process that controls the subsequent solid-state phase formations and eventually mechanical properties of the AM parts, a thorough understanding of the solidification behavior is most crucial to achieve final microstructural consistency. Solidification microstructure primarily varies as a function of solidification conditions, alloy phase diagram features, interfacial energy, and associated thermodynamic properties. Therefore, it is imperative to critically assess the interplay of these involved parameters on microstructure evolution to guarantee printability[1] and microstructure robustness[2] of metal AM parts.

In the context of AM, it is important to understand why microstructure formation during solidification is most critical. Suppose that severe microstructural heterogeneities remain at the final stages of solidification (Fig. 2d). In that case, they are reduced or eliminated *via* post-solidification operations, such as heat treatment, hot isostatic pressing, homogenization, solution annealing, and aging, which may remove nearly all other AM-related microstructural features, including desirable ones (e.g., γ' and γ'' phases in Inconel 718), and even allow the formation of unexpected and undesired phases (e.g., Laves and δ in Inconel 718) due to the heavily-segregated microstructures found in AM [28–30] (Fig. 2d). Moreover, the post-processing treatments are not only time-consuming and reduce the economic attractiveness of AM but may lead to harmful effects, including excessive grain growth and coarsening. It is noteworthy that according to Wohler's report 2021, the post-processing steps account for approximately 27 % of any metal AM processing costs [31]. Further, several studies [13, 32] report conflicting results on whether or not post-AM heat treatments are suitable for improving the final material properties. Several experimental studies reveal the persistence of as-solidified microstructural heterogeneities in certain regions of the AM material that endure high-temperature annealing [13, 15]. From the above discussion, it is clear that microstructure control during AM solidification is essential so that post-AM effects remain limited in order to exploit the advantages critical to this disruptive technology. Thus, alternate strategies related to AM solidification are required to develop AM-friendly microstructures and material properties. We review these strategies and their effectiveness toward microstructure prediction and control in the present work.

Different classes of solidification microstructure result during AM, including cellular, dendritic, equiaxed, eutectic, peritectic, and banded. Microstructure control during AM solidification can be achieved by analyzing whether these microstructures are beneficial or detrimental in terms of material properties requirements by characterizing the effects of the above-mentioned hierarchical multiphysics phenomena on the microstructure changes. The dynamically-evolving complex phase organizations and interface structures during mi-

[1]Printability is a global indicator of the susceptibility of a given combination of alloy-solidification conditions to develop uncontrollable microstructural heterogeneities that lead to solidification defects.

[2]Microstructure robustness refers to the susceptibility of a given alloy system to become less sensitive to solidification conditions.

crostructure evolution primarily depend on the thermophysical properties of the alloy material, solidification conditions, phase boundary properties, and time. With these interplaying parameters at hand, the following key questions may be important to consider for understanding the underlying mechanisms of microstructure evolution in AM.

- How to quantify the high number of influencing multiphysics conditions to account for the diversity of solidification microstructure and growth morphology obtained in metal AM?
- How to engineer the resultant grain morphologies for improving the composition homogeneity and phase control in AM of metals?
- How do the crystallographic interfacial phenomena influence the as-solidified AM microstructure?
- How do the late stage solidification processes in AM control the type and amount of microstructure-based defects in the final material?
- How do the atomistic nucleation mechanisms affect the grain size and final AM microstructure?
- How do the resultant meso-micro-nano-scale microstructure features interact during alloy solidification in AM?

These are some of the crucial yet poorly understood research directions that we critically address by reviewing computational modeling of hierarchical solidification microstructures produced *via* metal AM.

Owing to the large parameter space in AM solidification, modeling and simulation is essential to gain a detailed understanding of the resultant microstructure evolution. In the literature, computational modeling of microstructure formation and process-microstructure-properties relations in metal AM have been covered in many reviews [14, 33–41]. However, these studies represent only a brief overview of microstructure modeling techniques, with primary focus directed at modeling grain structure formation (coarsest microstructural feature) to illustrate process-structure-properties linkages. However, as discussed before, AM solidification is of hierarchical nature with nanoscale, micron-sized, and sub-millimeter features often co-exist in a solidified melt-pool. Thus, quantitative predictions of AM microstructures, and hence properties and performance, will require combined efforts in solidification modeling spanning several length scales and time scales. With this in mind, we present a comprehensive review to critically address the microstructure formation due to the hierarchical nature of AM solidification by integrating computational, analytical, and data-driven approaches. In particular, the critical role of the microstructure formation is highlighted in a rapid solidification regime (close to the Mullins-Sekerka absolute stability limit [42]) that has never been reviewed in the AM literature. Since the computational cost of large-scale (e.g., on the scale of full-melt-pool), high-fidelity microstructure evolution due to non-equilibrium AM solidification can be prohibitively high, we review high-performance computing tools relevant to exascale computing to address the computational challenges. To

the best of our knowledge, this area has not been addressed in the AM literature. Further, the underlying paradigm for AM is recently shifting from a mere prediction approach to specific *control* of microstructure features (e.g., grain/sub-grain morphology, orientation, composition, interdendritic secondary phases, etc.) that often requires identification of suitable solidification and alloy parameters. In this regard, the present review discusses strategies and their implementation to generate AM-friendly as-solidified microstructures that could potentially minimize the time, cost, and other undesired effects associated with post-solidification treatments for the development of new products using AM. Overall, our review presents a fundamental understanding of what controls the specific solidification microstructure features and, thereby, the possibility of modifying those features through changes in involved parameters. The solidification microstructure selection maps, which graphically represent the stability of microstructures generated under specified parameter ranges, could provide a useful rule of thumb towards microstructural control in AM of metals.

The structure of the article is as follows. In the following Sec. 2, we first describe the estimation of melt-pool solidification conditions followed by their implementation in microstructural simulations. In Sec. 3, we discuss different classes of solidification microstructures and their response to changing hierarchical AM conditions, aiming to provide recipes for controlling the harmful effects of microstructural anisotropy that arise during AM. In Sec. 4, we describe the solid-state microstructure characteristics, including defects, as long as they relate to AM solidification. In Sec. 5.1, we discuss the effect of atomistic nucleation mechanisms in producing the targeted solidification morphology under AM conditions. In Sec. 5.2, we briefly discuss the submicron-scale solidification microstructural features in AM. In Sec. 6, we briefly describe the use of machine learning approaches for the prediction and control of AM solidification microstructures. In Sec. 7, we briefly mention several approaches to estimate the mechanical properties of the as-solidified AM microstructures. Finally, we summarize and conclude with a discussion on future research opportunities in Sec 8.

2. Methods

2.1. General remarks

Difficulties in obtaining measurements at microscopic length scales, which are characteristic of nascent melt-pools in AM, combined with the rapid nature of the ensuing solidification process, make it hard to observe and study the AM process purely through experimental methods. Consequently, the amount of experimental data generated is limited, and so should be complemented with reliable data from computational modeling. A physics-rich solidification microstructure model will serve this purpose. Different numerical methods exist to study the microstructure formation during solidification (Fig. 4). Among them, the phase-field (PF) method is the most versatile and high-fidelity technique to simulate solidification microstructure as it can capture more physical phenomena during the solidification process, like pore formation (for reviews, see [43, 44]). We do not detail other low-to-medium fidelity methods (see Table 2 and Fig. 4), which are

primarily used for simulating grain structure and have limitations regarding AM microstructure simulation. For recent reviews on numerical models used for microstructure simulation in AM, refer to [36, 39–41].

Method	Computational cost/Accuracy	Benefits	Challenges
Phase-field method [43, 44])	Very High	Simulate both solidification and solid-state grain and sub-grain structure evolution at micro- and mesoscales.	It can be computationally expensive since the model uses small length scales and short time steps typical for AM. However, modern GPU and parallel computing approaches are able to overcome these challenges [45].
Cellular Automata [46–48]	Medium-to-High	Simulates solidification and solid-state microstructures at the mesoscale.	(a) The mesh used in simulations can introduce artificial anisotropy; (b) difficulties associated with the estimation of interfacial curvature relevant for AM; (c) accuracy depends on the mesh size.
Kinetic Monte Carlo [49]	Low-to-Medium	Allows for grain structure simulation over large domains only at the mesoscale.	(a) It cannot simulate solidification texture and solid-state processes in AM; (b) does not allow for direct coupling of thermal and microstructural models.

Table 2: A comparison of microstructure simulation methods used in AM.

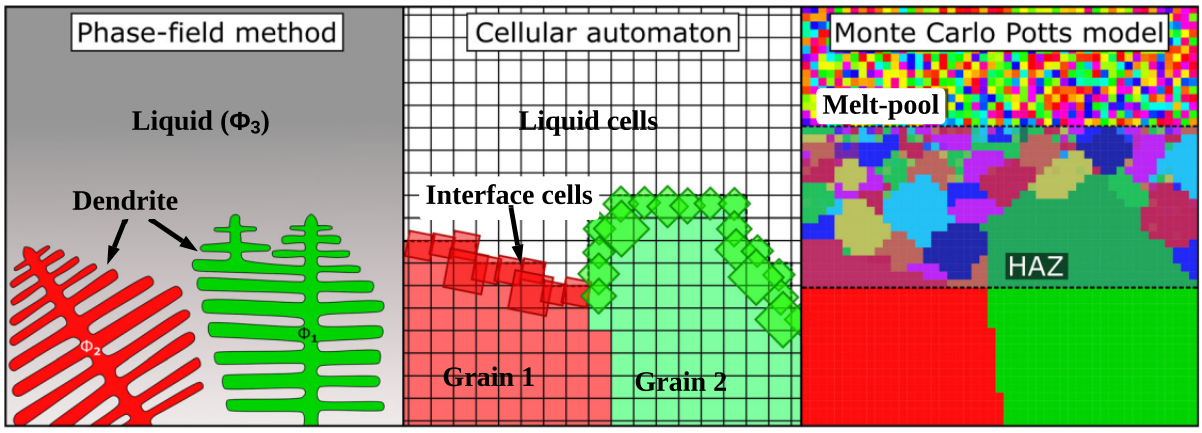

Figure 4: (Color online) Schematic demonstrates the basic idea behind the microstructure simulations using various modeling approaches. With a significantly higher resolution of both the simulation domain and the solid–liquid interface, the phase-field method generates a substantially lower mesh anisotropic error when compared to the cellular automata method. The Potts Kinetic Monte Carlo (KMC) model shows the highest level of abstraction with respect to the physical processes observed during melt-pool solidification with dendrites, segregation, and undercooling are not considered. The KMC method is primarily used to simulate grain evolution during AM [49]. HAZ in the figure (right) stands for the heat affected zone in the material. Adapted from Ref. [14].

The phase-field (PF) method represents the microstructure phases and interfaces by use of the discrete order parameter value φ. While the bulk phases, solid and liquid, are represented by constant values of φ, the solid-liquid interface is described by a continuous transition of φ between bulk phases. This approach avoids explicit interface tracking during PF simulation, making the implementation relatively straightforward when compared to the sharp-interface methods. The PF simulations can be simulated efficiently using massively parallel high-performance computing (HPC) clusters. This will aid in the faster discovery of optimal alloy and solidification parameters by efficiently screening out unsuitable material candidates and/or cooling conditions, leaving only those that warrant further investigation through physical experiments. Supporting experiments are essential to validate and calibrate the developed PF model; to compare it with the simulation results and established trends; to provide insights for further model developments. Microstructure formation during AM solidification could be increasingly better understood *via* validated PF simulations, thus saving

significant time and cost when compared with conducting numerous physical experiments. However, AM solidification is of an inherently multiphysics nature as it involves complex interacting hierarchical physical phenomena (Fig. 3). Therefore, a more predictive physics-rich PF microstructure model needs to be formulated to study materials-specific, location-related microstructure formation under imposed AM solidification conditions. In literature, these conditions are often estimated using a heat transfer finite element analysis (FEA) or flow-based computational fluid dynamics (CFD) model, as described below.

2.2. Macroscale thermal and mechanical analysis: Estimation of solidification parameters

Microstructure simulation requires model input parameters (temperature gradient G and solidification velocity R), which develop during melt-pool solidification [50–52]. They are often linked to the geometry of the dynamically-evolving melt-pool as a function of AM parameters, including the laser power (P) and beam speed (V) [53]. However, the short time scale of the solidification and small length scale of the melting pool hinder *in-situ* study of the solidification phenomena during experiments. Therefore, suitable FEA [54, 55] or CFD [55–57] simulations using commercial codes are often employed to simulate the melt-pool formation in an AM process [3]. The solidification begins at the melt-pool boundary approximated by the liquidus temperature isotherm of the alloy material. Therefore, G and R are often estimated at the melt-pool boundary or the mesoscale solidification interface [51, 58, 59]. Since the current review focuses on melt-pool solidification, only the salient features of numerical simulations related to solidification parameters and involved physics are described below.

2.2.1. Thermal analysis

The macroscopic FEA simulation addresses both the heat flow modeling during an AM process and the mechanical analysis of the AM part [3, 60, 61]. In a LPBF process, the laser scans across the powder bed of a certain thickness deposited on the substrate material. The transient, nonlinear temperature distribution throughout the substrate and the powder (see Fig. 5a) is determined by solving an equation for thermal energy conservation with appropriate initial and boundary conditions and input material properties [51, 58, 60]. When compared to the FEA model, CFD models are generally computationally more intensive due to the additional parameters to be solved for (e.g., pressure and velocity) [62] and the treatment of the free surface of the melt-pool [63]. A detailed overview of the number of possible thermal modeling strategies for metal AM, including the governing equations and boundary conditions, can be found in Ref. [63]. Several heat source models are used in the literature to simulate the laser-material interaction, including a moving pointwise heat source by Rosenthal [52, 64], a surface heat source obeying a Gaussian distribution [51, 58, 60, 65], or a double

[3]Certain commercial equipment, instruments, or materials are identified in this paper in order to specify the experimental procedure adequately. Such identification is not intended to imply recommendation or endorsement by NIST, nor is it intended to imply that the materials or equipment identified are necessarily the best available for the purpose.

ellipsoidal volumetric heat source [66]. Heat losses from natural convection and radiation are often considered. The temperature-dependent material properties, including thermal conductivity, bulk material density, latent heat, specific heat, and absorptivity, are often calculated thermodynamically [38, 67, 68] and used in FEA simulations [50, 51, 58]. Several non-equilibrium multiphysics phenomena, including viscous and buoyancy forces [63, 69, 70], melt flow [63, 70], Marangoni convection [69, 71, 72], evaporation cooling [51, 69, 72], and recoil pressure [69, 71, 73], affect thermal history in the melt-pool. Although computationally expensive, a more realistic thermal history can be obtained when all of these complex phenomena are modeled (Fig. 6). Of particular importance is the keyhole effect [69, 71, 73], which is largely driven by surface tension gradients induced by temperature gradients (the Marangoni effect), and the recoil pressure from evaporating fluid particles on the free surface of the liquid molten pool. These phenomena considerably modify the melt-pool geometry and the resulting thermal history (Fig. 6) [72]. From the steady-state melt-pool temperature profile, G and R values are estimated at the melt-pool boundary (Fig. 7a), as detailed in Refs. [51, 58, 59]. Depending on the alloy and process parameters in a specific metal-AM process, the values of G and R vary, typical ranges of which are given in Table 3. These values are input to the PF solidification model for microstructure simulations.

	LPBF	Electron beam PBF	Laser powder DED	Wire arc DED
G (K/m)	10^4 - 10^8	10^4 - 10^7	10^5 - 10^7	10^4 - 5×10^5
R (m/s)	0.01 - 1	0.001 - 1	0.001 - 0.01	0.001 - 0.1
References	[50–52, 58]	[72, 74, 75]	[76–78]	[79, 80]

Table 3: Typical values of solidification variables in most common fusion-based PBF and DED processes. Directional cooling rate is given by $G \times R$.

Further, the variation in G and R in the melt-pool (a measure of rapid AM processes) is shown in Fig. 7b. This information can be useful to predict the effects of rapid temporal changes in solidification parameters, including G, R, GR, and G/R, on the dynamically-evolving non-equilibrium growth morphologies and defects critical for AM. It is to be noted that these computed solidification parameters are functions of the melt-pool multiphysics phenomena considered. For example, the G and R values are reported to be extremely sensitive to the fluid flow parameters at the solidification front, suppressing the epitaxial growth of solidifying grains and promoting equiaxed grain formation [72]. Further, changes in laser scanning pattern [14, 81] and the number of layers [82, 83] in AM could have strong influence on melt-pool thermal cycles and the resulting solidification microstructures (Figs. 7c, 7d). For example, the computed GR and G/R decrease progressively with the addition of new layers, impacting the grain size and morphology in a multi-layer AM process. Finally, given the complex multiphysics nature of AM processes, the FEA simulation code needs to be validated by benchmark simulations [53, 84] or experiments [85].

2.2.2. Mechanical analysis

Following thermal analysis, stress analysis can be conducted using the temperature distribution obtained from the above FEA thermal analysis [25, 60, 86, 87]. A stress analysis solves a nonlinear stress equation until force equilibrium is reached and provides information on residual stresses and deformation in the AM part. The strain and stress are correlated *via* a mechanical constitutive law. Often elastoplastic behavior of the material is considered. The elastic, plastic, and thermal strains contribute to the total strain (often $<< 1$) in the AM material. The mathematical form of these strain components and the (elastic and plastic) stress-strain behavior of the material can be computed following Refs. [60, 86, 88]. The structural analysis uses the calculated temperature field, temperature-dependent mechanical properties, and phase proportions at the end of a particular step of the heat transfer analysis to compute the mechanical behavior. Although not shown here, the resultant thermal strain is of minimal value while large elastic strain (> 3 %), plastic strain (> 15 %), and residual stresses (> 500 MPa) develop surrounding the solidified melt-pool [25, 60, 89]. The magnitude of the strain is reported to increase with increasing laser power or heat input (P/V) while the maximum residual stress decreases for the same [25, 60, 89]. It is reported in Ref. [25] that doubling the heat input increases total strain by ≈ 2.5 times in Inconel 718 while the maximum residual stress decreases by about 20 % after doubling the heat input. In practice, appropriate processing conditions including laser parameters are to be selected in order to minimize the residual stresses in AM part.

Since the mechanical analysis data is generally not used as input in the solidification model, it cannot be linked directly to study microstructure evolution. This is because, the usual practical approach followed is not a fully-coupled one. It is generally assumed that the FEA thermal analysis results affect the structural calculation, while the reverse case is often not considered. This is done to minimize the overall computational time. Note that each FEA (thermal and mechanical) simulation relies on a set of laser power P and beam speed V values (or heat input P/V), which determines the thermal history and resultant $G - R$ values along the melt-pool solidification boundary. Therefore, $P - V$ and $G - R$ maps can be correlated (compare Figs. 2a and 7e) to microstructural characteristics, including the length scale of features and phase fractions [90]. These plots also signify that the morphology and size of phase/grain can be controlled by exploring the material-specific $G - R$ and $P - V$ maps. The first such integrated thermomechanical FEA and microstructure modeling during AM of Ti-6Al-4V alloys is reported in Ref. [60].

2.3. Physics-rich phase-field solidification model

As mentioned before, PF method is the most versatile, powerful, and accurate tool for microstructure simulation and thus more relevant in the solidification regime of AM. In the context of the multiphysics conditions, the PF method is quite flexible in addressing multiple physical variables (e.g., composition, anisotropy, phase, interface, temperature, orientation, diffusion, elasticity) in the underlying free-energy functional of the system, and the coupled effects of the involved variables can be simulated *via* time-dependent

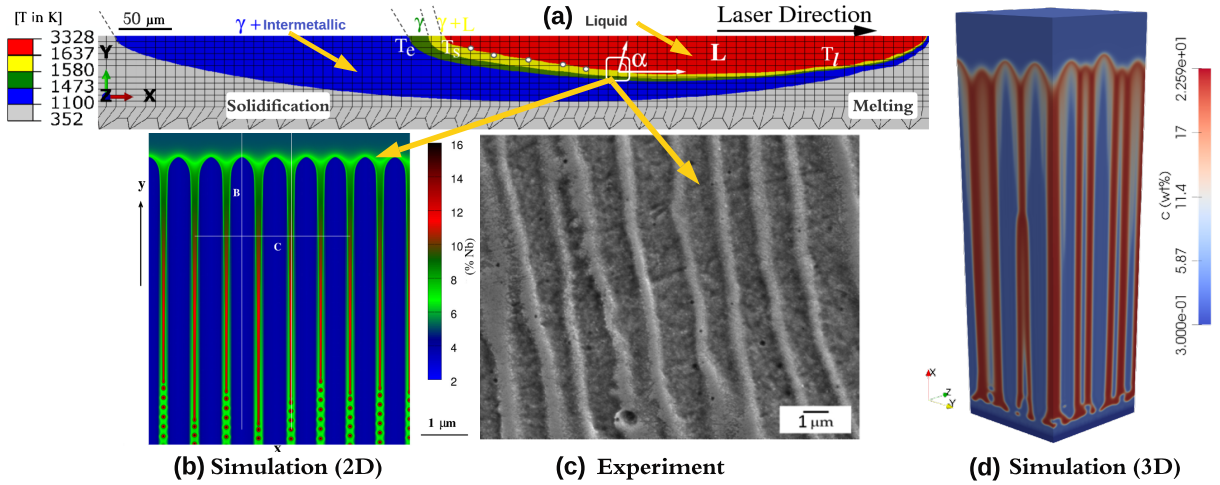

Figure 5: (Color online) Previous work on LPBF of Inconel 625 and 718 alloys [50, 58, 91]. (a) The temperature distribution in the melt-pool was estimated through 3D FEA simulations of a single-track laser scan across a layer of Inconel 718 powder [54]. The laser melt-track is a 2D slice of 3D FEA simulations. The laser power P is 180 W and the beam speed V is 800 mm/s. The values of G and R are determined at different microscopic locations along the mesoscale melt-pool boundary. Here, the temperature boundaries (delineated by different colors) represent various phase transformations, which correspond to the alloy phase diagram. L is liquid, γ is the primary solidification phase, and the intermetallic, in general, represents the interdendritic segregated phases that form during terminal solidification. The macroscopic V can be linked to microscopic interface velocity R through $V \cdot \cos\alpha$, where α is the angle between the velocities. The G at a melt-pool location can be calculated by $||\nabla T||$. (b) The computed G and R values are input to PF simulations, resulting in a cellular microstructure with non-equilibrium composition distribution (shown by the color scale bar); these microscale features are expected to form at the same solidified melt-pool region in AM experiments. (c) Exemplary experimental measurement of cellular microstructure relates to PF simulations (reproduced from [92], with permission from Elsevier). (d) 3D PF simulation of a cellular microstructure with the composition scale bar are shown for the same G and R values as in 2D (Fig. 5b).

partial differential equations (PDEs), resulting in microstructure formation. These PDEs are available in many of our publications and elsewhere [51, 91, 95–97] and hence are not repeated here. A general description of the phase-field model and equations can be found in Sec 2.1 of our publication Ref. [98]. There are challenges to simulate non-equilibrium microstructures under rapid AM conditions. Thus, the accuracy and resolution of the PF model are sacrificed and, hence, further developments of specific model components for more realistic microstructure simulations are warranted.

The coupled effects of heat and solute diffusion during melt-pool solidification should be considered in the PF simulation [99]. Ideally, the mechanical deformation resulting from solidification shrinkage and internal stresses may cause inelastic processes in AM (e.g., dislocation microstructure), hence should be incorporated in the PF model through the mechanical part of the system free energy [100, 101]. In addition, the free energy of the microstructure phases and non-linear diffusion-related terms should be calculated thermodynamically and incorporated in the PF model through the chemical part of the system free energy [38, 67, 68]. Under rapid AM conditions, the local equilibrium assumption ceases to be valid, resulting in strongly out-of-equilibrium compositional effects such as microsegregation and solute-trapping. While the PF method does not enforce local equilibrium, the diffuse interface employed in simulations magnifies the effect. The PF

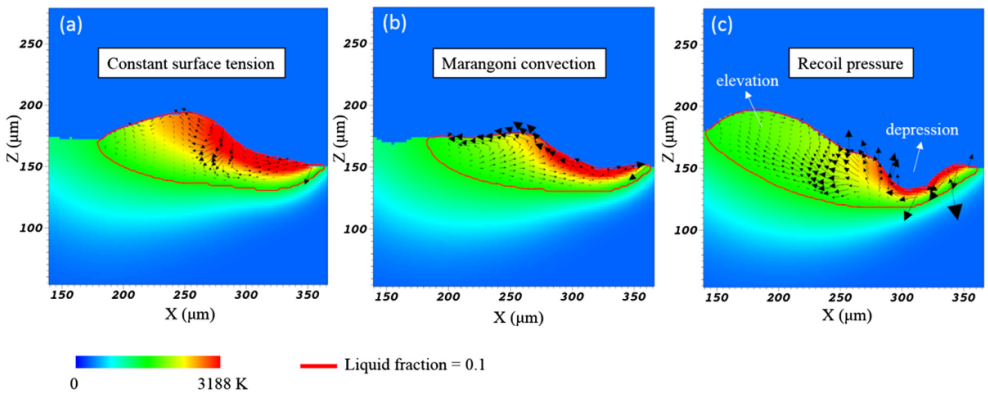

(a)

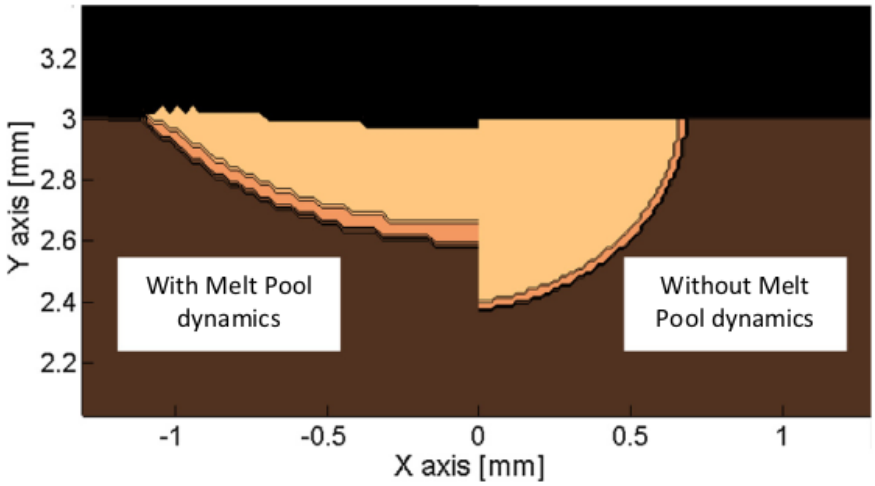

(b)

Figure 6: (Color online) (a) In Inconel 625, melt-pool characteristics are simulated under different physical effects but with the same AM parameters and time. These macroscale physical effects modify the mesoscale melt-pool boundary and consequently the estimated solidification parameters (reproduced from [71], with permission from Elsevier). The scale bar denotes temperature. (b) In 304 stainless steel, the influence of the fluid flow on final melt-pool geometry is illustrated (reproduced from [70], with permission from Elsevier). This affects the resulting solidification parameters, which, in turn, determine the evolution of microstructure and defects. All the above laser melt-tracks are 2D slices of 3D FEA simulations.

method includes an anti-trapping solute flux term to correct unphysical effects that arise due to the use of large numerical interface thickness values at low solidification velocities [102]. This correction is not accurate for higher-order coupling parameters and for high solidification velocities typically required for AM applications; thus, it may artificially modify the simulated microsegregation and solute-trapping effects. This numerical parameter particularly needs refinement, for example, by considering the local interfacial curvature effects and solidification velocity-dependence for the alloy parameters to reflect the non-equilibrium changes at the moving interface. Incorporating solid-state diffusion in the model may be as important as diffusion in the liquid; otherwise, regions with artificially high solute amounts may develop in the as-solidified microstructure. The effects of melt convection on solute and heat transport should be included in the PF

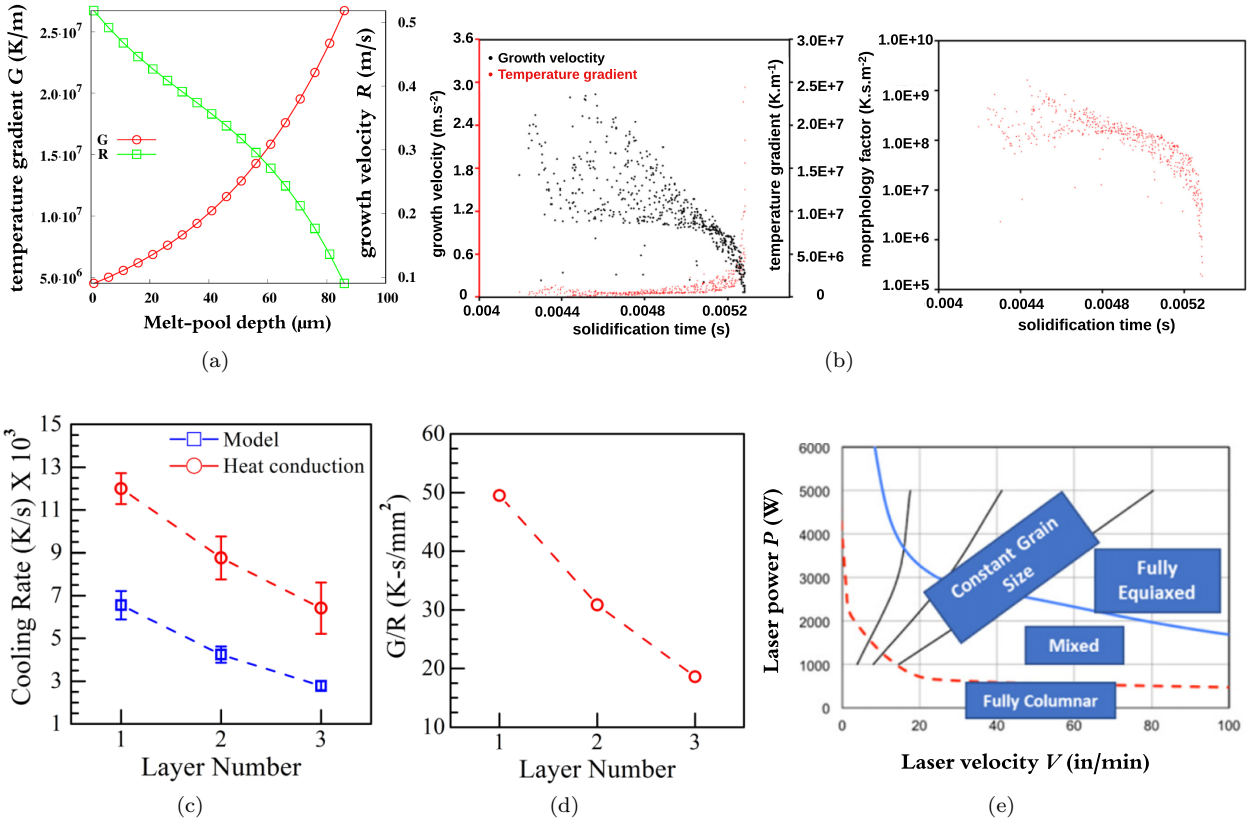

Figure 7: (Color online) (a) FEA simulations estimate G and R in Ti-6Al-4V for $P = 200$ W and $V = 500$ m/s, which vary as a function of melt-pool location [93, 94]. (b) FEA simulations compute different solidification parameters that vary as a function of solidification time. Each point in this plot corresponds to a finite element node within a cross-section of the melt-pool(adapted from [63], with permission from Elsevier). (c, d) FEA simulations estimate decreasing cooling rate and morphology factor with increasing layer number in a multi-layer laser AM process (reproduced from [82], with permission from AIP Publishing). (e) Schematically shown how an AM process map describes the solidification microstructure characteristics as a function of P and V (adapted from [29], with permission from Elsevier). This process map combined with the $G - R$ solidification map (Fig. 2a) demonstrate that the length scale and final microstructure can be controlled by exploring these material-specific maps.

model, for example, *via* coupling with the lattice Boltzmann method [103]. Further, the heat and solute diffusion equations may include the effect of different heat sources during the AM process, including the latent heat rejection, laser melting, and heat extraction from the substrate, that are needed to study the effects of remelting on microstructure evolution, particularly, on the nucleation of new grains/phases at the melt-pool boundary, thus allowing the simulation of microstructures directly from the melt-pool [104, 105]. The microstructure model with the above modifications can then be applied to evaluate the AM solidification process in order to find an effective way to prepare robust microstructures to suit a targeted AM application.

2.4. High-performance computing (HPC) and exascale computing

From the numerical viewpoint, the PF models for AM in general tend to have more variables and equations, which are solved on a large domain with a small mesh size and, hence, a small time step size. This makes PF simulations computationally intensive. Fortunately, the PF codes can be implemented for

massively parallel HPC clusters, making simulations feasible within much shorter time frames. HPC systems typically utilize the latest CPUs[4] and GPUs[5], as well as low-latency networking fabrics and storage devices, to improve processing speeds and computing performance. However, the cost of a multi-CPU cluster, the CPU-parallel implementation, in particular, in three-dimensions, and the calculation efficiency make the HPC approaches utilizing conventional CPU-parallel methods less appealing for intensive AM simulations. Recently, HPC simulations are increasingly powered by GPUs, because of its massive computation capacity and large bandwidth at a relatively low cost. The GPU code is written in the CUDA programming language developed by NVIDIA [106] and the HIP and ROCm languages for AMD GPUs [107], each of which has a parallel extension to C and C++ programming. In a multi-GPU infrastructure, the communication and computation overlap between nodes affects the performance of GPUs. To minimize such computational overhead, CPU+GPU hybrid parallel programming could be adopted [108].

Further, the PF model equations can not only be solved on a desktop computer using single-purpose codes, but also on existing PF software, including `MOOSE` [109], `MICRESS` [110], `OpenPhase` [111], `FiPy` [112], `PRISMS-PF` [113], and `Tusas` [95]. While most of these software packages offer flexibility to incorporate additional AM multiphysics conditions, only `Tusas` [95] offers additional functionality by its implementation within hybrid CPU+GPU parallel HPC architectures, which massively accelerate the computational performance of PF simulations and thus a large number of dendrite and grain structures can be simulated very efficiently (Fig. 3g). For reference, the HPC-enabled `Tusas` phase-field program simulates the 2D and 3D cellular microstructures under AM conditions that are shown in Figs. 5b and 5d. The simulated microstructural features are in good agreement with the experimental measurements shown in Fig. 5c.

Next-generation high-fidelity simulation tools for complex multiscale multiphysics AM solidification in an industrial setting are currently intractable without the power of exascale computers [114, 115]. In the context of exascale computing, the United States Department of Energy (DOE) currently houses three of the top five supercomputers in the world [116]. The Summit [117] and Sierra [118] architectures are based on NVIDIA [106] GPUs. Both HPC machines are currently utilized for AM simulation [95]. The DOE machine Frontier [119] is based on AMD GPU architecture [107]. It is currently the fastest supercomputer in the world, has been deployed and is now publicly available for large-scale AM simulation. New DOE exascale platforms arriving in the coming years include El Capitan [120] and Crossroads [121]. Supporting these platforms, the United States DOE has current investments in efforts for large-scale AM simulation, including the Exascale Computing Project (ECP) [114, 122], and projects funded within the Advanced Scientific Computing Research (ASCR) [123] and the Innovative and Novel Computational Impact on Theory and Experiment (INCITE) [124] programs within the DOE Office of Science. In particular, the Transform-

[4]CPU stands for Central Processing Unit.
[5]GPU stands for Graphics Processing Unit.

ing Additive Manufacturing through Exascale Simulation (ExaAM) project [19, 20] within ECP has been successful [125]. It is to be noted that the `Tusas` program is supported by ECP as it is capable of performing simulations on exascale HPC architectures [95].

2.5. Parameter and alloy selection

As mentioned in Sec. 1, solidification microstructures are highly anisotropic in terms of grain and sub-grain level inhomogeneities due to the rapid nature of heating and cooling conditions in AM. While it is entirely unavoidable to remove the above heterogeneities due to the non-equilibrium nature of AM solidification, the present review considers process recipes in terms of solidification conditions and assumes alloy parameters in terms of phase diagram features to minimize these heterogeneities in order to achieve better printability and microstructure consistency. As described in Sec. 2.2, the input solidification conditions, G and R (hence GR and G/R), are obtained from macroscale FEA simulations. In the view of AM solidification, the critical phase diagram features include the equilibrium partition coefficient (k_e), equilibrium liquidus slope (m), equilibrium freezing range (ΔT), and the nominal composition of the alloy (C_0) [50, 51, 59, 91, 96]. These parameters can be taken from phase diagram databases [126]. There is a strong connection between these topological features of the phase diagram and the sensitivity of resulting microstructures (in terms of phase constitution and phase stability) to variation in AM solidification conditions. Thus, these parameters need to be made solidification velocity-dependant (i.e., k_v, m_v, and ΔT_v) because of the non-equilibrium state of the solid-liquid interface found in AM. These non-equilibrium parameters can be obtained from thermodynamic considerations, as detailed in [58, 127, 128]. Other thermophysical and kinetic parameters relevant for AM microstructure evolution are the solid diffusivity (D_s), liquid diffusivity (D_l), interfacial free energy (γ), capillary length (d_0), Gibbs-Thomson coefficient (Γ), interface kinetic coefficient (μ), and, importantly, time (t) [50, 51, 59, 91, 96]. These parameters are typically estimated by experimental measurements or atomistic simulations such as molecular dynamics [129, 130] and sometimes found in the literature. For γ, the expression:

$$\gamma(\hat{n}) = \gamma_0(1 + \epsilon_4 \cos(4\theta)), \tag{1}$$

is often considered in the PF model to introduce the anisotropy of the solid-liquid interfacial free energy. Here, γ_0 is the orientation-independent average interfacial energy, $\hat{n}$ is the interface normal vector, ϵ_4 is the magnitude of the four-fold anisotropy, and θ is the interface orientation angle [51, 91]. When the microstructural anisotropy leads to faceted interfaces in the solidification microstructure, interfacial stiffness,

$$S(\theta) = \gamma(\hat{n}) + \frac{\partial^2 \gamma(\hat{n})}{\partial \theta^2}, \tag{2}$$

is often incorporated in the PF model to regularize the sharp corners and edges to avoid the model equations becoming ill-posed [131, 132]. The above-mentioned parameters are incorporated in the PF equations,

which are derived either from a phenomenological free energy function or from a realistic materials free energy function calculated thermodynamically [44]. The PF equations are solved with appropriate initial and boundary conditions and numerical parameters such as domain size, grid size, interface thickness, time step size, model relaxation time, and other dimensionless coupling parameters to simulate microstructure evolution [43, 44, 96, 102, 133].

To model microstructure evolution during AM solidification, sample alloy systems should be judiciously selected that show solidification reactions relevant for AM and superior properties at elevated temperatures typical of AM applications. To simplify the physics and computational complexity, one should initially focus on the binary systems before simulating multicomponent alloys, noting that ternary and multicomponent alloys are often studied as pseudo-binary approximations (e.g., Inconel 718 as Ni-Nb and Ti-6Al-4V as Ti-10 % X) to reasonably predict solidification microstructure evolution during AM. In this review, we have selected a few model alloys (Ni-Al, Ni-Zr, Ti-La, and Ni-Nb in Fig. 8) for reference that can be used to evaluate microstructure formation under AM conditions. Binary alloy simulations will efficiently and rapidly assess a wide parameter space and further guide for more detailed PF simulations of multicomponent systems, among others. Depending on the magnitude of G and R, the candidate alloys solidify into different classes of microstructure, including cellular, dendritic, equiaxed, eutectic, peritectic, and banded, which need to be characterized thoroughly to understand parameter-microstructure relationships in AM of metals.

3. Microstructure prediction and control

3.1. Dendritic solidification

Extremely fine cellular and columnar dendritic morphologies are most commonly observed in AM of metals owing to the steep G and high R that develops during melt-pool solidification (Figs. 9a, 9b). In general, the G/R ratio governs the solidification mode while the cooling rate (GR) controls the scale (λ in Fig. 9a $\approx 1\,\mu$m) of the resulting microstructure. The microstructural length scales, including the cell/dendrite spacing, are often approximated by a power law:

$$\lambda = AG^{-m}R^{-n}, \tag{3}$$

where A, m, and n are constants [58, 91]. In the literature, the values of m and n are often reported to be generally between 0 and 0.6 depending upon the alloy system and solidification parameters employed and the geometry of the cellular/dendritic arrays assumed [137]. In this context, there exist different analytical models that correlate λ with the cooling rate (GV) or the $G^{-0.5}V^{-0.25}$ parameter (in Eq. (3)) for families of alloys [138–140]. Among them, the model of Kurz and Fisher [140],

$$\lambda = 4.3(\Gamma \Delta T D_l/k_e)^{0.25} G^{-0.5} R^{-0.25}, \tag{4}$$

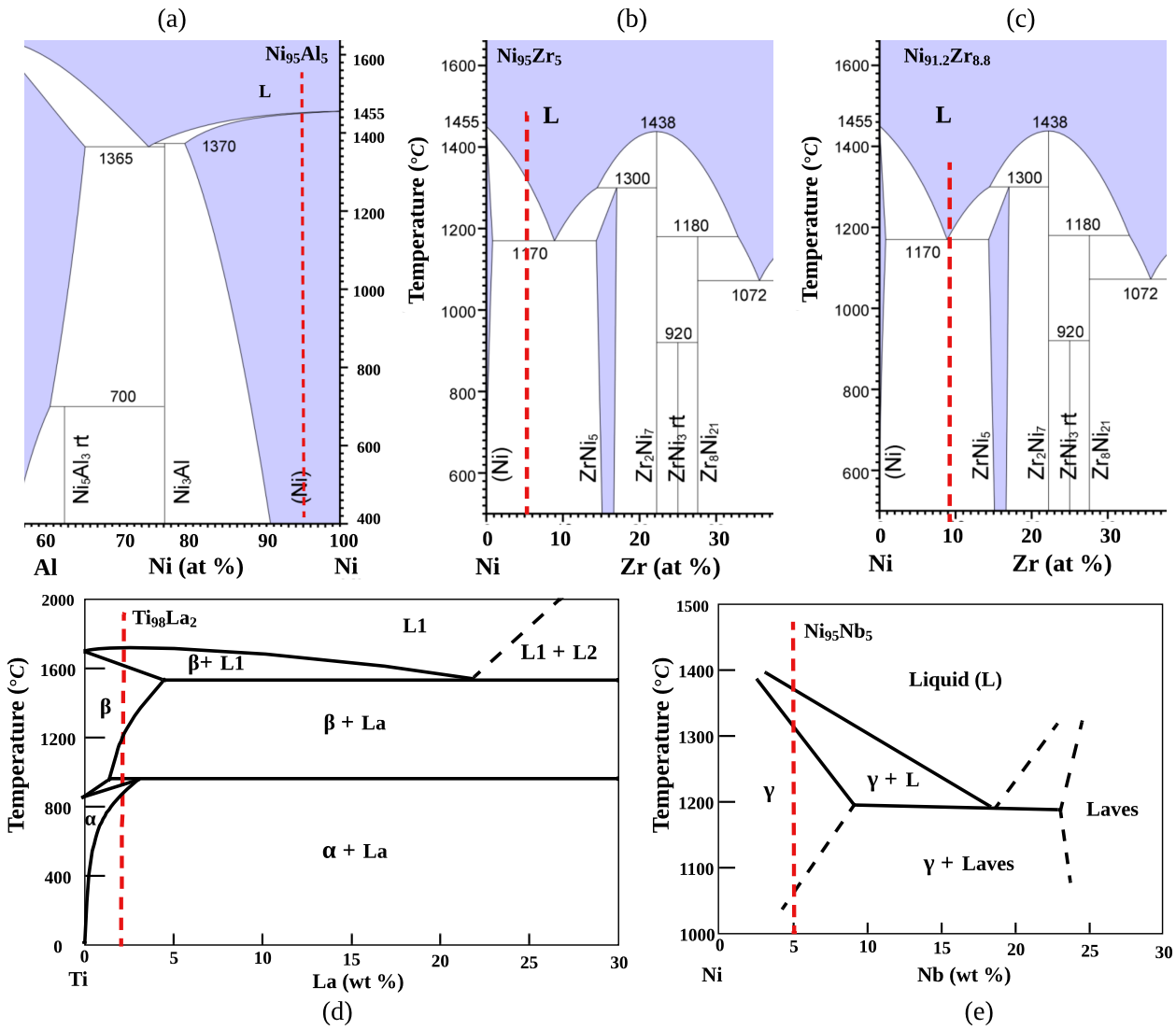

Figure 8: (Color online) Selected binary systems (Ni-Al (partial), Ni-Zr (partial), Ti-La (partial), and Ni-Nb (partial)) are used to explain solidification dynamics and microstructure evolution under AM conditions in the present review [134–136]. The red dashed line on the phase diagram shows the alloy composition (C_0) or alloy material of interest. The alloy phase diagrams are shown for representation purposes only, noting that suitable phase diagram and alloy composition can be used to simulate different classes of solidification microstructures, including dendritic, eutectic, and peritectic, relevant for AM.

has been proven by a body of experimental and numerical evidence to be effective and reasonably accurate in determining λ during AM of Inconel 718 [52, 137, 141–144].

The microsegregation pattern (Fig. 9b) that develops during cellular or dendritic solidification often leads to unexpected and undesirable segregated phases in the final microstructure (Fig. 2d). This phenomenon is known as solute-trapping, which strongly depends on the interface velocity R and the equilibrium partition

coefficient k_e, measured by the partitioning of the solute element in solid and liquid at the interface, i.e.,

$$k_e = \frac{C_s}{C_l}. \tag{5}$$

As demonstrated in Ref. [91], these characteristic compositions can be analytically estimated following different microsegregation models, including the Scheil-Gulliver equation [127, 145],

$$C_s = k_e C_0 (1 - f_s)^{k_e - 1}, \tag{6}$$

where f_s is the fraction of the material in the solid phase, and the Kurz and Fisher model [127, 145],

$$C_s = \frac{k_e C_0}{1 - (1 - k_e) Iv(P_e)}, \tag{7}$$

where $Iv(P_e)$ is the Ivantsov function and P_e is the Péclet number approximated by $Rd/(2D_l)$ with d the cell/dendrite tip radius. Under non-equilibrium solidification conditions, k_e (in Eqs (6) and (7)) becomes velocity-dependent and thus the microsegregation (k_v in Fig. 9a) can be characterized by [146–149]:

$$k_v(R) = \frac{k_e + R/R_D}{1 + R/R_D}, \tag{8}$$

where the characteristic diffusive velocity of atoms at the solid-liquid interface (R_D) is some function of $W_0 R/D_l$, where D_l is the interface diffusion coefficient, W_0 is the characteristic interface width, and R is the interface velocity. When R is very large, k_v approaches unity, meaning that the solubility of the element in both phases is identical, and microsegregation is expected to be minimal. Thus, an increase of R through beam speed is expected to reduce microsegregation. It is predicted that R greater than 10 m/s are required for k_v to approach unity, for example, in the Si-As alloy [150].

Data on D_l and R_D, which are generally found from experimental curve fitting, is not available for many commonly studied AM alloys. Still, it is known that R on the order of 10 m/s could be reached when the beam scan speed is dramatically increased. That said, most studies report R values during AM to be in the range of $\approx$ 0.01 m/s to 1 m/s. This, combined with the unknown R_D for various alloys, makes it uncertain whether increasing R alone would be sufficient to reduce microsegregation without causing additional build defects during AM of metals. For example, large R would correspond to high scan speeds, which are generally associated with a greater tendency to form 'balling' defects [151].

From the phase diagram viewpoint, an alternate technique to control microsegregation comes from k_e itself. If k_e is unity, then the control of R alone becomes a moot point, and the alloy is not expected to experience microsegregation as it solidifies like pure metal. This situation can be investigated using an alloy with a narrow solid + liquid two-phase region, which leads to a very small difference between liquid and

solid solubility. It is then likely that smaller microsegregation would be observed. From this simple feature of the phase diagram, it is then possible to select potential alloy systems that would not be handicapped by solute-trapping, which can lead to the development of undesirable solid phases, negatively impacting the material properties. For reference, let us consider two sample Ni-based alloys with equivalent binary composition in Figs. 8a and 8b, but they have small and large solute partitioning, respectively. It is expected that Ni-Al would show minimal microsegregation as its liquid and solid compositions are nearly identical for all temperatures. On the other hand, significant microsegregation is expected in the Ni-Zr alloy, as demonstrated experimentally in Ref. [134].

In the context of AM, the above-mentioned Ni-alloys are expected to solidify with directionally-growing cells (dendrite without sidearms) and dendrites due to the morphological instability (Mullins-Sekerka instability [42]) that develops at the moving solid-liquid interface (Fig. 9a). It is well-documented in solidification literature that the grain/phase morphology depends on the growth velocity of the interface (R) and liquid thermal gradient at the interface (G). The window of solidification can then be estimated from the plots of G and R (Fig. 9c). From such plots, one can ascertain that an increase in G and decrease in R favors the growth of columnar dendritic morphology while increasing R and decreasing G favors the growth of equiaxed dendritic morphology. However, the typical values of R estimated during AM are between

$$R_{th} < R < R_{ab}. \tag{9}$$

Here, R_{th} (on the order of mm/s) is the critical velocity approximated by the constitutional supercooling criterion,

$$G/R_{th} < \Delta T_v/D_l, \tag{10}$$

beyond which local equilibrium fails; and R_{ab} is the absolute stability velocity,

$$R_{ab} = \Delta T_v D_l/(k_v \Gamma), \tag{11}$$

beyond which morphological instability disappears (see Fig. 9c). A definition of ΔT_v, D_l, k_v, and Γ can be found in Sec. 2.5. In the regime of R (Eq. (9)), the window of solidification gets modified as there is a transition of solid-liquid interface morphology from dendrite (equiaxed mode *vs.* columnar mode) to cellular to plane front as R approaches close to R_{ab} (on the order of m/s) typical of AM. Further, as R becomes closer to R_{ab}, G increasingly plays a minor role in the microstructure selection process [58, 152]. Consequently, growth morphologies can be represented in terms of R *vs.* C_0 maps (Fig. 9d). This map illustrates that under AM conditions, stable solidification microstructure for dilute alloys typically changes with R in the sequence: dendrite $\rightarrow$ banded $\rightarrow$ planar, while for concentrated alloys microstructure changes in the sequence: dendrite $\rightarrow$ eutectic $\rightarrow$ banded $\rightarrow$ planar [128]. Depending on the resultant growth morphology, the degree of

microsegregation and other phase heterogeneities in the final microstructure will vary accordingly, affecting the final material properties. Therefore, in view of the above sequential phase transformations under non-equilibrium conditions, solidification microstructure selection (SMS) maps can be constructed as a function of G *vs.* R or R *vs.* C_0 to guide microstructure prediction and control in AM of metals.

Further, microstructure analysis of solidified melt-pool reveals that cells and dendrites grow epitaxially in the direction of maximum temperature gradient parallel to the build direction (Fig. 9e). However, such preferential growth direction (or texture) of the columnar structure can be different due to the location-related G and R conditions in the solidified melt-pool (Fig. 9c). This affects the spatial and temporal solute partitioning across the solid-liquid interface, leading to microsegregation and solute-trapping patterns (Figs. 9a, 9b) and, subsequently, unwanted anisotropy in the mechanical properties of the AM parts. Such non-equilibrium solidification behavior can be explored efficiently by varying the solidification conditions, interface energy anisotropy, and interface orientation in the underlying chemical free energy of the PF model (Fig. 9f). For more quantitative results, at least two points need to be considered. First, the influence of interface orientation on the microsegregation behavior belonging to the single dendritic grain needs to be quantified (Fig. 9f). Second, simulations should consider several dendritic grains in competition (i.e., competitive growth) to study the question of grain selection [156], which will consider various orientation angles and convergent/divergent growth conditions between dendrite grains that may affect the observed levels of microsegregation and solute-trapping (Fig. 3g). In this way, the underlying mechanisms of microstructural processes in dendrite materials will be better understood, the knowledge of which will guide microstructure control under rapid solidification.

Although not shown here, the layer number, beam scanning and shaping strategies in a multi-track, multi-layer AM process (while maintaining constant laser power and scan speed) affect the G and R conditions (thus GR and G/R) in the melt-pool, controlling the key solidification microstructural features, such as morphology, size, and texture (e.g., equiaxed *vs.* columnar). For example, both G and R decrease with the increasing layer number, modifying the solidification mode and microstructural length scale [41, 82]. Customizing the scanning strategy between the continuous and pulsed beam and further controlling the movement of the beam lead to spatial-temporal variation of G and R, tailoring the solidification modes and thus texture [157]. The local modulation in the laser beam intensity profile (i.e., beam shape such as ellipticity) is also found to strongly affect the resulting solidification microstructural features [48]. This knowledge will aid in developing strategies for microstructure control during AM of dendrite materials and closely related systems described below.

3.2. Eutectic solidification

The eutectics are the second most (after dendrites) commonly observed solidification microstructures found in as-printed AM materials. In alloys that exhibit eutectic transformation (Fig. 8c), the liquid of

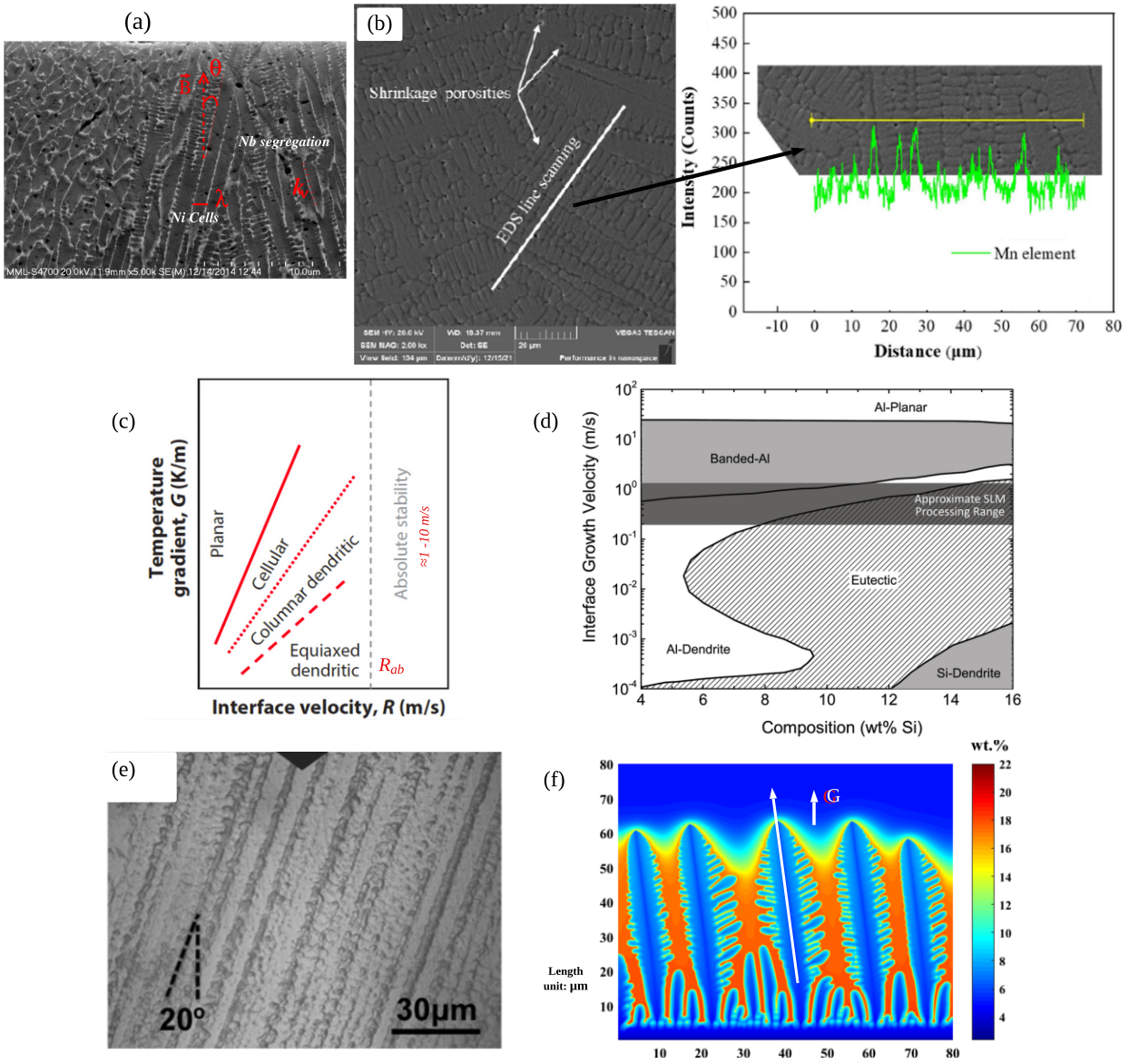

Figure 9: (Color online) Microstructure evolution of metals fabricated by the LPBF process. Build direction $\vec{B}$ is vertical. (a) Columnar dendritic microstructure results during AM of Inconel 625 alloy (reproduced from [50], with permission from Elsevier). Microstructural inhomogeneities result due to microsegregation (k_v) and solidification misorientation/texture (θ). λ is the primary dendrite arm spacing. (b) Rapid cooling rates in AM lead to heavy interdendritic microsegregation of solute particles in the as-solidified microstructure. The energy dispersive spectroscopy (EDS) line scanning analysis of elemental distribution illustrates the microsegregation pattern in the interdendritic channels during AM of steel samples (adapted from [153], with permission from Elsevier). The final stage of solidification often leads to heterogeneities such as shrinkage microporosity in the dendrite material. (c) In a schematic solidification map (Type 1), the solidification modes or morphologies are presented in G *vs.* R plots. R_{ab} is the absolute stability velocity limit, see text for details. (d) In the solidification map (Type 2), various types of solidification microstructure are presented *via* R *vs.* C_0 plots for a quasi-binary Al-Si alloy with $G = 10^6$ K/m (reproduced from [128], with permission from Elsevier). (e) Measurement of the misorientation angle θ (in Eq. (1)) between the columnar growth and build direction is shown (reproduced from [154], with permission from Elsevier). (f) Typical PF simulations show dendritic morphology with interdendritic solute microsegregation that results during AM of Inconel 718 (adapted from [155], with permission from Springer Nature). Similar to experiments, dendrites grow with sidebranches along a preferred growth direction relative to vertical G direction.

eutectic/near-eutectic composition directly solidifies into two distinct solids without passing through a liquid + solid region, and hence phase segregation does not occur. Also, the eutectic growth occurs in a coupled manner as the solids mutually exchange mass ahead of the solid-liquid front, resulting in a regular lamellar structure with alternate arrangements of the phases characterized by the interlamellar spacing (λ). This combined with eutectic undercooling ΔT and R results in the well-known growth relationships [158],

$$\lambda^2 R = \frac{K_2}{K_1} \quad \text{and} \quad \frac{\Delta T^2}{R} = 4K_1K_2, \tag{12}$$

where K_1 and K_2 are material constants. The experimental measurements on Pb-Sn lamellar eutectic [145] show $K_1 = 0.09$ s K µm^{-2} and $K_2 = 2.87$ µm K when $R = 1$ µm s^{-1}, $\lambda \approx 5$ µm, and $\Delta T \approx 1$ K in Eq. (12). Typical value of the constant K_2/K_1 has been reported to be 88 µm^3 s^{-1} for Al-Cu eutectic alloy [159]. The alloy composition and cooling rate (GR) significantly affect the size, morphology, and fraction of the eutectic phases. For example, lamellar spacing becomes increasingly refined with the increasing cooling rate. Ultrarapid AM cooling conditions refine the microstructure even further and lead to nanometer-scale ultrafine eutectics with excellent mechanical properties [159, 160]. For example, a value of $\lambda = 15$ nm (each phase is some 20 atoms wide) seems to be the minimum spacing that can be achieved with R on the order of 0.2 m/s [161]. As is the case with dendrites (Sec. 3.1), the eutectic growth relations under AM conditions also become interface velocity-dependent as given for λ by the relation:

$$\lambda^2 R = \frac{K_2^v(R)}{K_1^v(R)}. \tag{13}$$

Further, alloys with faceted interfaces such as Al-Si result in irregular eutectics, where coupled regular growth does not occur and lamellar spacing can be represented by

$$\lambda_m^2 R = \phi^2 \frac{K_2^v(R)}{K_1^v(R)}, \tag{14}$$

where λ_m is the mean lamellar spacing and ϕ is a material property equal to the ratio of λ_m to the spacing at the extremum (assumed to be minimum undercooling) [128]. Moreover, a partial or complete transition from a regular lamellar microstructure to an anomalous eutectic (often resulting from fragmentation of lamellar phases *via* lamellae $\rightarrow$ stripes $\rightarrow$ cylinders $\rightarrow$ spheres) is found depending on the cooling rate [162, 163]. Interfacial energy involved with extremely fine eutectic scales observed in AM materials may play a critical role in this process [164].

In the view of AM, eutectic formation is further complicated by the complex thermal history in the melt-pool due to the repeated passes of the laser remelting/solidification and the wide range of cooling rates that develop at different melt-pool regions. As a result, the size and morphology of the eutectic phases

deviate significantly at different locations within the laser trace, leading to morphological heterogeneities in the as-solidified microstructure [159, 160]. For example, uncoupling in the eutectic growth can occur under rapid AM conditions close to the bottom of the melt-pool, where a fine lamellar structure is interrupted by large single-phase regions, leading to the so-called anomalous growth (Fig. 10a). During anomalous growth, microstructure evolution is extremely sensitive to the alloy composition and cooling rate. On the other hand, when the anomalous eutectic solidification does not occur, microstructure evolution is dominated by coupled growth of the eutectic phases, leading to lamellar arrays close to the surface of the solidified melt-pool (Fig. 10b). In this region, multiple remelting sequences typical of AM possibly result in final cooling rates that are sufficiently small to maintain the coupled growth of the eutectic phases. Also, a dramatic reduction in the characteristic eutectic spacings is observed between the top and bottom regions of the solidified melt-pool. The average λ observed is $\approx 20\,\mu$m around the surface, while it is only ≈ 100 nm near the base. Such refinement in the eutectic structure leads to dramatic enhancement on strengthening the microstructure (≈ 300 MPa in the surface *vs.* ≈ 1000 MPa in the base). Currently, very limited work on AM of eutectic alloys exist. Therefore, it is essential to explore different eutectic materials and cooling conditions to quantify the coupled/uncoupled eutectic growth transition and associated length-scales in relation to λ *via* PF simulations. In this context, the Al-Cu and Ni-Zr eutectic alloys (Fig. 8c) can be studied that exhibit high-temperature eutectic reactions, which should be relevant for AM. A solidification microstructure selection map (Fig. 9d) combined with a stability analysis, which determines the operating ranges of different eutectic growth structures for the variables lamellar spacing and alloy composition, can be performed for a given specific eutectic material under AM conditions. These studies could potentially help in developing strategies to guide parameter-microstructure control during eutectic phase transformations in AM of metals.

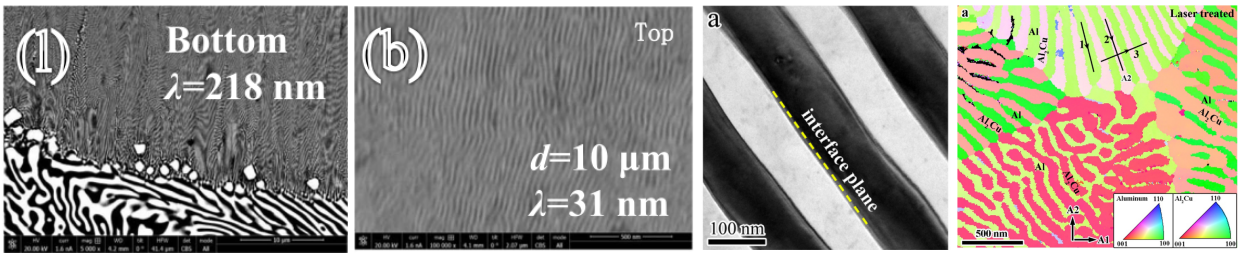

(a) (b) (c) (d)

Figure 10: (Color online) EBSD images of Al-Cu eutectic alloy microstructures (a) near the bottom and (b) near the top of the solidified melt-pool (reproduced from [159], with permission from Elsevier). (c) Interface boundaries grow at an angle with respect to the build direction (vertical) in Al-Al_2Cu eutectic grain. (d) Inverse pole figure map of the laser-treated eutectic alloy shows the orientation selection between multiple eutectic grains. (c) and (d) are reproduced from [165], with permission from Elsevier.

Further, microstructural anisotropy may also result from the orientation (or texture) of the eutectic phases. Non-equilibrium solidification of eutectic materials may strongly depend on the crystal orientation

of the two eutectic phases [127], affecting the material properties. Such crystallographic effects during *microscale* eutectic growth have been appreciated only recently [166, 167]. What happens to these effects on *nanoscale* eutectics that develop during AM? Why do eutectic grains with preferred orientation relationships prevail during AM solidification? These research directions have never been explored using theories or models. It has been recently confirmed that the interface energy and its anisotropic properties significantly affect the orientation of the microscale eutectic phases [166, 167]. This anisotropy depends on the relative orientation of the eutectic phases with respect to each other. Whereas the solid-liquid interface in eutectic-forming metals are only weakly anisotropic and can be described by smooth anisotropy functions, the interfacial energy of the solid-solid boundary can be strongly anisotropic and may exhibit facets [164, 166, 167]. In eutectic grains with special orientation relationships, interfacial energy often exhibits sharp cusp-like minima that correspond to specific low-energy microscopic configurations. The above effects can be explored efficiently by including suitable interface anisotropy functions and interface rotation angles in the chemical free energy part within the underlying free energy functional of the PF model. In these simulations, two key points should be considered. First, within a single eutectic grain (Fig. 10c), the orientation angle of the nanoscale eutectic phases with respect to the temperature gradient direction needs to be estimated. Second, simulations should consider several eutectic grains to examine the competition between multiple orientations (Fig. 10d) in order to study the question of grain selection mechanism. These results may provide an explanation for the prevalence of grains with preferred orientation relationships in nanoscale eutectics [165]. In this way, the mechanisms of eutectic microstructural processes under AM conditions can be understood for a given eutectic material.

3.3. Peritectic solidification

One of the less desirable aspects of fusion-based AM processes is the formation of coarse columnar solidification microstructure/texture attributed to the intrinsic high G and R values in AM [168]. This leads to unwanted anisotropy in the mechanical properties of the AM parts. As mentioned in Sec. 1, it may be impractical to alter the AM microstructure *via* post-processing heat treatments and hot isostatic pressing as they expected to have limited impact on a severely textured as-printed microstructure [169]. Therefore, post-AM operations often do not represent a straightforward alternative to mitigate solidification texture. The best solution is to promote the transformation of the columnar structure into an equiaxed morphology (without forming undesirable intermetallic phases) during AM solidification [168–172].

Grain refinement accompanied by morphology control can be achieved *via* solute additions (i.e., inoculation) and adjusting solidification parameters in AM of alloys. It is generally observed that increasing the cooling rate decreases grain size, improving the mechanical behavior of the alloy but at the expense of the resulting columnar morphology. Therefore, challenges remain to transform this morphology into a fine equiaxed morphology in order to control the harmful effects of solidification texture. As mentioned in

Sec. 3.1, analytical solidification maps in terms of $G - R$ or $R - C_0$ plots can be used as a guide to identify the involved parameters ranges required to enhance columnar-to-equiaxed transition (CET). In general, CET occurs when the favorable interfacial instability and constitutional undercooling parameters trigger a localized heterogeneous nucleation event at the nucleating particles at or ahead of the solidification front, leading to patches of fine equiaxed morphology within a predominantly columnar structure [127]. However, there is an ongoing challenge in AM is to produce a homogeneous microstructure with complete elimination of epitaxial columnar grain/phase morphology [168].

To address the above challenges, an alternative path to produce fine equiaxed morphology is the presence of a peritectic reaction during AM solidification (Fig. 11), the knowledge of which is extremely limited. In contrast to the columnar microstructure (say, δ in Fig. 11a) resulting from monophase solidification (i.e., Liquid $\rightarrow \delta$), peritectic solidification results from multiphase solidification (i.e., Liquid $\rightarrow$ Liquid + $\delta \rightarrow$ γ). Depending on the alloy composition, peritectic reactions frequently result in the pro-peritectic dendritic phase in the liquid (say, Liquid $\rightarrow \delta$) followed by the nucleation and growth of the peritectic phase (γ) around the dendritic arms of the primary δ phase (Fig. 11a). Once the reaction is complete, a peritectic phase with a fine homogeneous equiaxed morphology typically results (Fig. 11b) with $\approx$ 4 to 5 times reduction in grain size [168–170, 172]. Analytically, the average grain size of the alloy material under AM conditions can be estimated by the power law:

$$\bar{d} = K \left(\frac{1}{Q} \right)^n, \tag{15}$$

where K is some function of D_l/R; Q is the growth restriction factor given by

$$Q = m_v c_0 (k_v - 1); \tag{16}$$

and n is a material constant reported to be between 0.33 and 1 in experiments [168]. Often, the peritectic phase acts as heterogeneous nucleation sites, leading to grain refinement and thus improved mechanical properties of the solidified material. Successful applications include Sc- and/or Zr-modified Al alloys having a high-Q value [168, 171]. The peritectic phase (e.g., Al_3Sc, Al_3Zr) in these alloys modifies the highly coarse ($\approx$ 10 µm) columnar microstructure to significantly refined ($\approx$ 0.8 µm) structures separated by an equiaxed morphology at the solidified melt-pool boundaries [173, 174]. However, the volume fraction of the microstructure characterized by equiaxed morphology has been found to depend on the processing conditions employed. For example, an increase in both preheat temperature and heat input (corresponds to a low G/R ratio) during LPBF led to a fully equiaxed microstructure in Al alloys [173]. Also, the solidification crack formation was significantly reduced and even prevented by the grain refining effect caused by the peritectic phases during AM rapid solidification in these peritectic alloys [174].

In addition, the rapid cooling rates in AM often lead to independent simultaneous nucleation of primary

and peritectic phases directly from the melt, hence, they are not in crystallographic orientation relation with each other [169]. As a result, significant texture reduction becomes possible in (quasi-binary) Ti-Al and Ti-La alloys by reducing the columnar microstructures with an equiaxed morphology (Fig. 11b). It is worth noting that the complete elimination of columnar texture will require elements that have a strong effect on raising the melting temperature of the base element/alloy for a particular alloy system. Until currently, no alloy element is known for enabling grain and texture refinement in steels through peritectic reaction. On the other hand, rare earth elements such as La lead to significant texture reduction and the formation of fine equiaxed morphology in Ti alloys (Fig. 8d) [169, 170]. Thus, a Ti-La alloy (Fig. 8d) can be modeled using a multi-phase-field model to understand the above peritectic reaction mechanisms, considering the interplay among alloy composition, alloy phase diagram parameters, and solidification conditions. This may lead to a better understanding of the peritectic mechanisms in AM of metals, the knowledge of which will positively impact commercial Ti and Al alloy compositions and would be applicable for morphology control and thus properties in other major alloy systems.

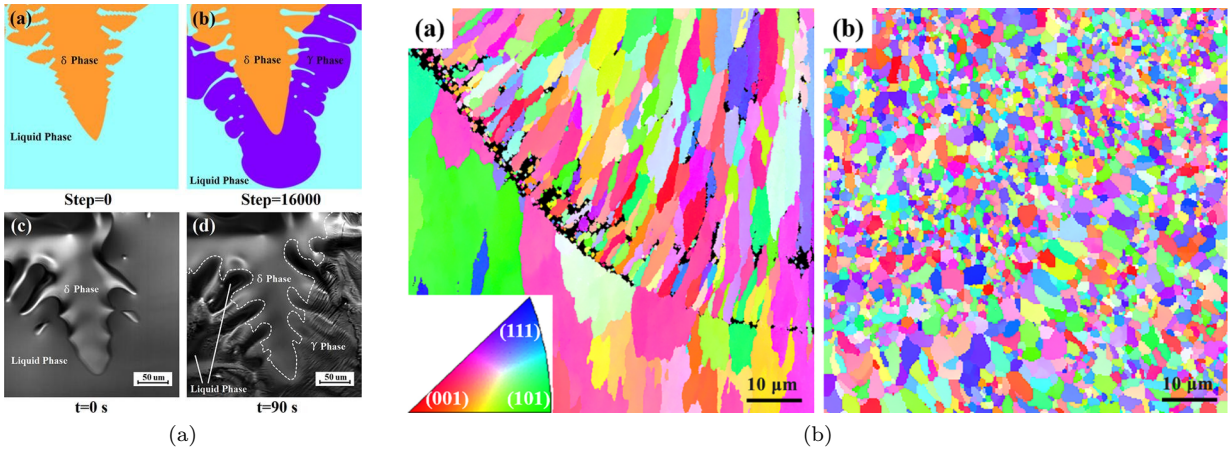

Figure 11: (Color online) (a) Multi-phase-field simulations (top panel) and experimental observations (bottom panel) of peritectic solidification in Fe-C alloys are presented to demonstrate peritectic reaction mechanisms (reproduced from [175], with permission from Elsevier). The peritectic reaction is given by: Liquid + $\delta \rightarrow \gamma$. The δ, γ, and Liquid phases are denoted by orange, purple, and turquoise colors at simulation iteration step = 0 and step = 16000, respectively. Time is denoted by t in experiments. More details is given in the text. (b) The EBSD orientation maps from side view of AM-fabricated Al-Cu-Mg alloy (left) and Ti-modified Al-Cu-Mg alloy (right) are shown. The EBSD maps demonstrate the effect of Ti as a peritectic forming element, which led to the formation of a fine homogeneous equiaxed microstructure without cracks (reproduced from [172], with permission from Elsevier).

3.4. Banded Structures

Following the microstructure selection map (Fig. 12a), the final probable solidification microstructure that could form due to an extremely high R value (close to R_{ab}) is the banded structure [176] (Fig. 12). This type of strongly far-from-diffusion-equilibrium structures are not commonly observed in traditional manufacturing processes. Depending on the features of the alloy phase diagram and rapid solidification

conditions, peritectic microstructures can be present in alternate layers of primary and peritectic phases, leading to harmful band-like phase distribution pattern in the laser-solidified microstructure [127]. Recent work [170] has shown that under specific alloy compositions (often concentrated alloys) and processing conditions, banded structures transform into a fully lamellar eutectic microstructure (see Fig. 12b and the solidification map in Fig. 9d), which provides balanced mechanical properties with sufficient ductility and strength at elevated temperatures typical of AM applications.

Further, depending on the alloy composition (often dilute alloys) and rapid solidification conditions, the formation of bands consisting of plane front and cellular/dendritic morphology is also possible [177, 178] (Fig. 12c). According to an extensive study of several alloy systems, it is found that $R >> R_{ab}$ are needed in order to definitely produce an absolutely stable planar solidification front. Thus, when $R \approx R_{ab}$, we generally do not observe a planar solid-liquid front but rather an oscillating interface, signifying the transition from a columnar dendritic structure to a banded pattern. It is to be noted that banded structures are rarely observed in the final AM microstructure as these structures are expected to form at the highest R regions in the solidified melt-pool (i.e., top surface), which are likely to get eliminated during the printing of subsequent layers or upon post-AM processing. Further, G often plays no role in the rapid solidification regime relevant for banding. Therefore, PF simulations can be performed with highly segregated Ni-Zr, Al-Cu, and Al-Fe alloys (see Figs. 12d, 8b) as a function of initial composition and growth velocity to investigate banding phenomena in AM of metals. The band spacing estimated from these simulations can be compared with experimental measurements, as illustrated in Ref. [179].

4. Prediction and control of solidification microstructure-based defects and heterogeneities

Besides the presence of microstructural inhomogeneities discussed in previous sections, solidification defects such as microporosity and hot tearing (or hot cracking) are commonly observed in the as-printed microstructure [1, 3, 127] (Fig. 13). Microporosity often results during the late stage columnar/dendritic solidification of AM materials when solid dendrites grow toward each other and finally coalesce in the semi-solid mushy zone[6], entrapping the solute-rich liquid in the interdendritic region [58]. As the fraction of the solid in the mushy zone increases to greater than ≈ 0.7, the liquid in the interdendritic channels cannot flow freely and compensate for solidification shrinkage, resulting in microporosity (size of $\approx 1\,\mu m$ and smaller) (Fig. 13a) [91]. Consequently, the semi-solid mush becomes weak and develops microcracks and eventually ruptures under tension at elevated temperatures. This phenomenon is known as hot tearing (Fig. 13b) [8, 181]. Although the influence of solidification defects on the material properties has been studied for years, prediction and control of defects still remain a challenge in the AM community. It is even more

[6]The mushy zone in columnar dendrites is a two-phase solid and liquid coexistence region between the fully solid and the fully liquid states where the majority of the solidification defects form.

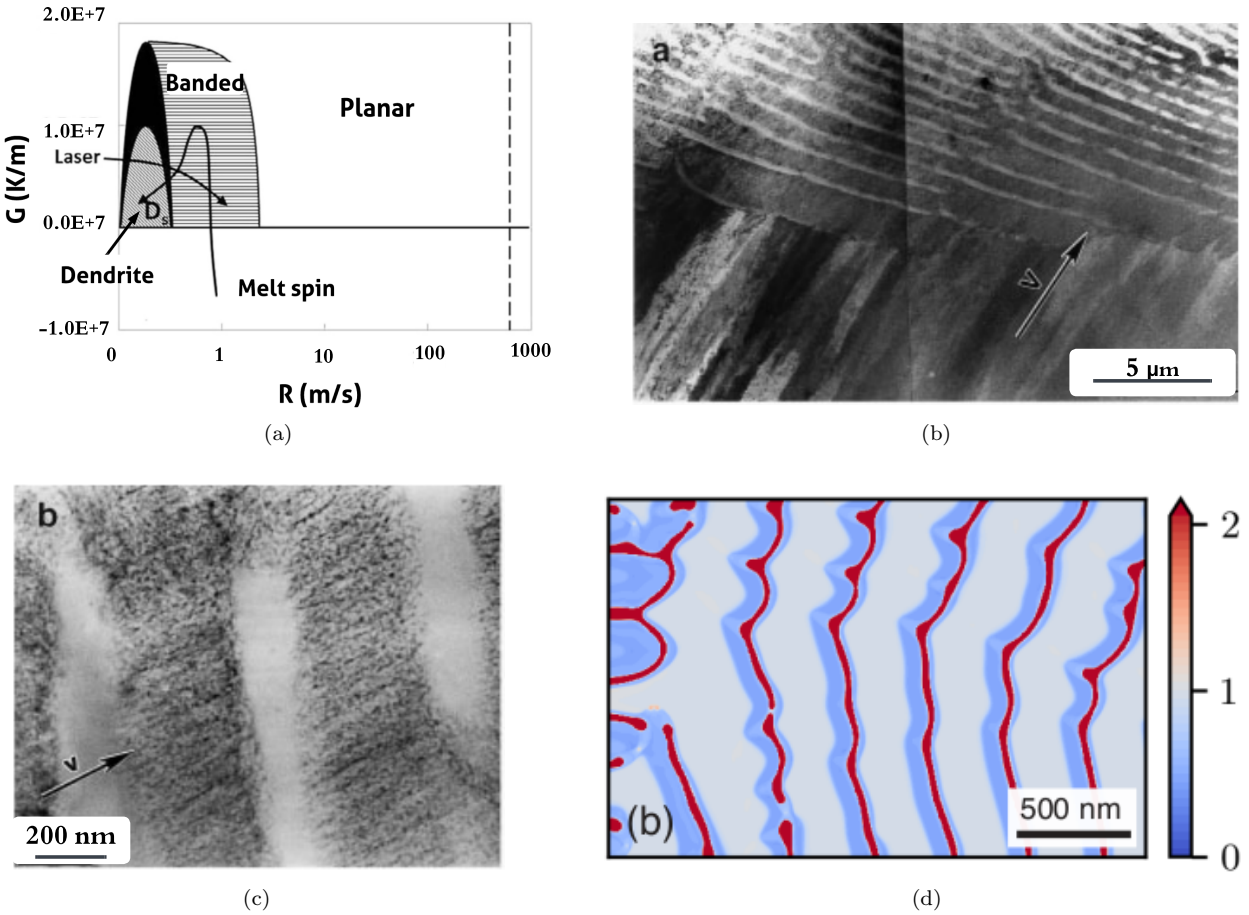

(a) (b) (c) (d)

Figure 12: (a) $G - R$ solidification microstructure selection (SMS) map for typical values of $G = 10^6$ K/m and $R = 0.4$ m/s, adapted from [180]. (b, c) TEM images of banded structure formation in laser AM of metal alloys (reproduced from [177], with permission from Elsevier). (b) Transition from lamellar eutectic morphology to banded structure (upper part) and *vice versa* is observed in a eutectic Al-33 % Cu alloy for $R = 0.5$ m/s. (c) Formation of cellular/dendritic (dark band) and plane front (clear band) banded structure in Al-4 % Fe alloy with $R = 0.7$ m/s. (d) Phase-field simulation of banded microstructure in Al-9 %Cu alloy is shown using a composition colormap (reproduced from [179], with permission from APS). The band spacing in simulation (≈ 400 nm) agrees well with the experiment. Composition is represented in mass fraction.

challenging for controlling defects predominantly during AM solidification, since post-AM operations may introduce many undesirable effects, as discussed in Sec. 1.

4.1. Microporosity

A detailed understanding of the microstructure-based evolution of porosity (Fig. 13a) and its correlation to solidification and alloy parameters will help address the associated challenges in AM. The porosity effects are characterized by the pore size, morphology (e.g., spherical, elliptical, elongated, irregular), volume fraction, distribution, interconnectivity, and tortuosity [182]. Tortuosity describes the impact of the shape of micropores. The dimensionality offers another degree of freedom to pore-microstructure interaction; for example, the interconnectivity in 3D leads to a more enhanced diffusion and percolating pore network

compared to the same in 2D. Also, the elemental microsegregation during rapid AM solidification alters the local compositions surrounding the pore that may later promote heterogeneous nucleation of the solid phases. Further, the volume shrinkage during terminal solidification leads to residual stresses and mechanical deformation, which may have significant impact on the interface structure and porosity evolution and subsequently the material properties [3, 25].

In the AM literature [3, 182, 183], the type and amount of porosity are often correlated to material-specific process energy density, which is some function of laser power P and beam speed V (e.g., heat input P/V) (Fig. 13c). Thus, it would be important to study how does the magnitude of energy input impact pore characteristics. When the energy input is increased from low to high values, the pore morphology changes from irregular to nearly spherical [182]. However, at intermediate energy input values, a pore-free microstructure is obtained [182]. Also for some materials, there exists a critical energy input value above which the amount of porosity increases rapidly [180] (Fig. 13c). These simulated pore microstructures can be characterized using mathematical descriptors such as circularity, sphericity, convexity, and curvature analyses, which may reveal critical information regarding pore formation mechanisms and local pore-microstructure interactions. For example, a pore with sphericity or circularity greater than ≈ 0.7 is found to be more beneficial for material properties when compared to an irregular pore morphology around which spatio-temporal features of the microstructure vary more locally, degrading the mechanical performance of the alloy [182]. Therefore, understanding the porosity dynamics and pore-microstructure interaction is essential.

With a PF solidification model [100] (Sec. 2.3) combined with appropriate starting material and boundary parameter ranges, microstructural evolution of porosity can be predicted efficiently as a function of solidification parameters, alloy phase diagram features, and time. The computational fluid dynamics and volume-of-fluid-based approaches could also be used to study microporosity formation under AM conditions, although their implementation is quite arduous when compared to the PF method [184, 185]. Based on the simulation result, a reliable process window then can be developed using $G - R$ solidification maps or $P - V$ process maps in which an optimal parameter settings will potentially reduce/remove the unwanted effects of the solidification defects (Fig. 13d). Note that a set of $G - V$ parameters can be correlated to $P - V$ process parameters *via* finite element thermal analysis [58] or, as a first approximation, *via* the solution to the Rosenthal equation [64, 183] (Sec. 2.2).

4.2. Hot tearing

During PF simulations of dendrite material, the fundamental parameters that control the onset and subsequent evolution of solidification defects are the dendrite arm spacing, solid and liquid phase fractions, mushy zone thermal history, dendrite coalescence, and alloy composition [8, 91, 127]. By considering the variation of these characteristic features as a function of solidification time t and distance x along the interdendritic channel and their correlations to process thermal gradient G, interface velocity R, and cooling

rate GR will help estimate hot cracking susceptibility (HCS) of a given material. For example, a measurement of df_s/dT near $f_s = 0$ (f_s is the solid fraction) can be used to describe the liquid entrapment behavior in the interdendritic region that may influence solidification shrinkage and cracking phenomena during terminal solidification (Fig. 14a) [91, 181]. In this context, the Kou HCS index [181],

$$\text{HCS} = \max \left| \frac{dT}{d(f_s^{0.5})} \right|, \tag{17}$$

can serve as a useful reference to qualitatively determine if hot cracking will occur. Further, the length of the mushy zone is largest for low R values and decreases with increasing R, which, in turn, reduces the dendrite arm spacing and liquid channel segregation, facilitating earlier coalescence of adjacent dendrites to resist cracking [91, 181, 186]. In a directionally-solidifying dendrite material, when solid fraction increases to a value greater than ≈ 0.7, a transition from a liquid-like to a solid-like behavior of the mushy zone is observed, promoting the formation of solidification defects [91]. Also for some materials, there may exist a critical energy input value around which microcracks originating from hot tearing will appear [180, 187]. The above-mentioned general approaches and parameters can be used to formulate material-specific criteria functions in linear or polynomial forms, which will rapidly determine the effects of changes in involved parameters on the trends of HCS as well as microporosity (Sec. 4.1).

4.3. Interdendritic secondary phases

During columnar solidification under non-equilibrium conditions, the rejection of solute element (when $k_v < 1$) at the solid-liquid interface severely enriches the interdendritic liquid channels (Fig. 14a). As a result, the solute-rich residual liquid in the mushy zone freezes at a much lower temperature. Thus, a solidified columnar structure is produced with interdendritic secondary phases (size of $\approx$ 20 nm to 150 nm) (Figs. 14b, 14c) [11, 24, 30, 189, 190]. These solid phases often result due to a eutectic reaction that occurs below a critical temperature and beyond threshold solute composition values given by the alloy phase diagram (Fig. 8e). The interdendritic secondary particles are often enriched by alloy elements in variable amounts, hence precipitated as different intermetallic phases, such as Laves and δ in Inconel alloys (Figs. 14b, 14c). It is observed that a finer size and discrete distribution of secondary phases are beneficial compared to a coarser and continuous distribution (Fig. 13b) of the same, when resistance to deformation was considered [188, 191, 192]. Moreover, various studies have also recognized the effect of columnar texture and dendrite arm spacing on the precipitation of these phases [193, 194] (Fig. 14c). Further, increasing the cooling rate decreases the degree of microsegregation, giving insufficient time for solute diffusion from the dendrite core to the liquid. As a result, the volume fraction of secondary phases decreases with increasing cooling rate and typically varies between $\approx$ 2 % and 20 % in experiments and numerical simulations [188, 191, 195] (Fig. 14e).

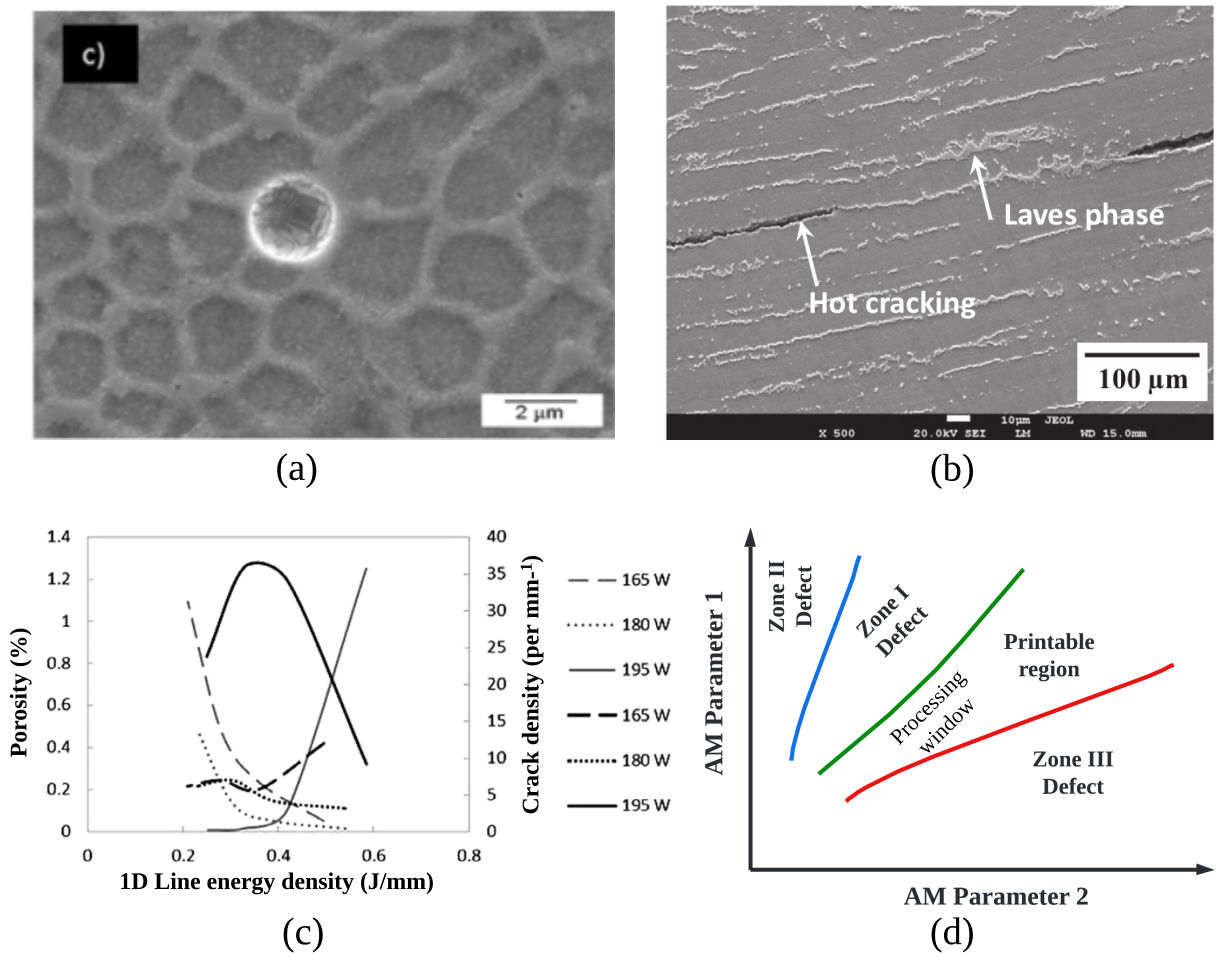

Figure 13: Solidification defects formation in AM of metal alloys. (a) Small, rounded microporosity results during AM of a stainless steel 316L alloy (reproduced from [92], with permission from Elsevier). (b) Hot cracking with a long-chain morphology of the Laves phase form during laser AM of Inconel 718 (reproduced from [188], with permission from Elsevier). (c) Microporosity (grey) and microcrack density (black) in the as-solidified material strongly varied as a function of laser parameters and thus line energy input (from [180]). (d) Schematically shown how process-solidification maps can be constructed for the prediction and control of solidification defects. The combination of (AM parameter 1 *vs.* AM parameter 2) could potentially be (laser power *vs.* beam speed), (thermal gradient *vs.* interface velocity), or (process heat input *vs.* melt-pool geometric terms) [3, 22, 183]. Here, the printable region (or process window) signifies optimal process or solidification parameter ranges that will allow the formation of good-quality solidified material with minimal defects, while other zones (I, II, and III) represent non-optimal parameter settings that lead to defects detrimental to the material properties.

The secondary phases often have a detrimental effect on the mechanical properties of the AM parts. Thus, determination of the influence of the features of alloy phase diagram, interface orientation, and solidification conditions on the size, morphology, distribution, and volume fraction of the secondary phases is essential. For a candidate material, the Ni-Nb alloy can be studied to simulate the secondary eutectic phase formation *via* Liquid $\rightarrow \gamma + Laves$ (Figs. 8e, 14d). Proper implementation of the starting material and threshold composition and temperature boundary conditions in the PF model (Sec. 2.3) would allow quantitative prediction of the type and amount of the secondary phases within the as-solidified interdendritic network

(Fig. 14d). These simulations could also determine the processing window (e.g., a function of time and temperature analogous to heat treatment) for each interdendritic phases, depending on whether it is either beneficial or harmful in terms of final mechanical properties requirements. This knowledge will help in developing solidification strategies to prepare homogeneous microstructures without harmful precipitates as required for structural applications.

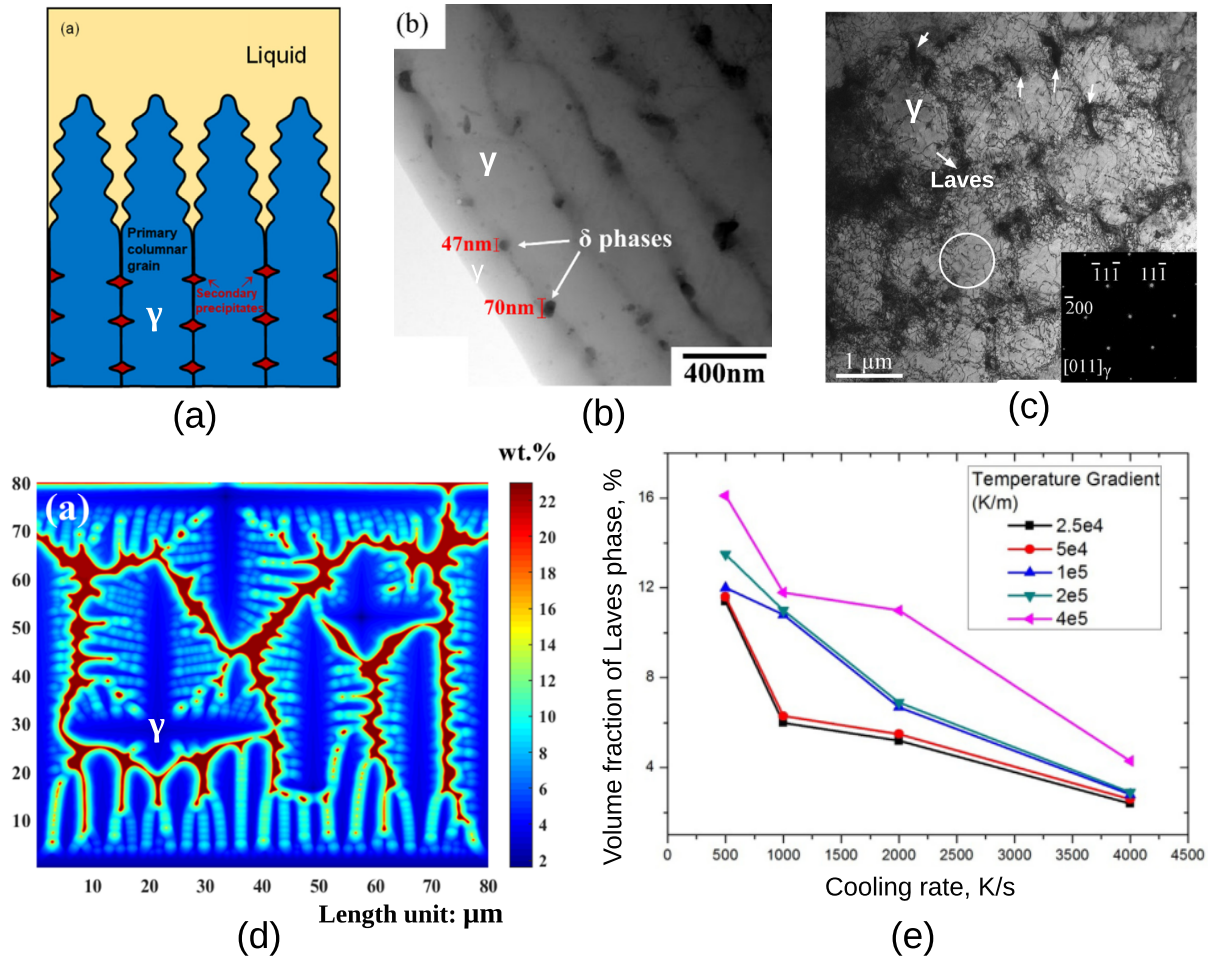

Figure 14: (Color online) (a) Schematic demonstration of the formation of γ dendrites along with secondary/segregated phases at the interdendritic regions. (b) Secondary δ phase forms at the interdendritic boundary (reproduced from [24], with permission from Elsevier). (c) Laves phase along with other defects such as dislocation microstructure form in the as-printed microstructure of Inconel alloys (adapted from [15], with permission from Elsevier). (d) Phase-field simulations of dendritic growth show significant solute enrichment in the interdendritic channels to be solidified during terminal solidification. These solute-rich liquid pockets are expected to form harmful Laves phase following terminal solidification (reproduced from [155], with permission from Springer Nature). (e) The Laves fraction decreases with increasing cooling rate during AM of Inconel alloys (reproduced from [188], with permission from Elsevier).

4.4. Unique microstructural irregularities

In addition to the above solidification defects, microstructure inhomogeneities in the form of unique microstructural irregularities may also be present in the as-solidified microstructure. These microstructural

features are not accessible *via* traditional manufacturing methods such as casting, forging, or rolling. Under non-equilibrium, rapid solidification conditions, significant spatial variations in solute amount are observed across local regions in the solidified melt-pool that led to, among others, zigzag [176], mosaic [196], and periodic columnar-to-equiaxed transition (CET) [197] microstructural patterns (Figs. 15a, 15b, 15c). Complex scanning pattern and multi-layer material deposition during AM have a role in the formation of these microstructural nonuniformities.

Further, the study of the interplay between eutectic and dendritic structures has an enduring popularity in AM of metals, which is influenced by both solidification conditions and alloy composition [198] (see Fig. 9d). Unfortunately, such competitive growth under non-equilibrium solidification conditions is rarely studied. In this context, AM solidification led to a novel *hybrid*, hierarchical microstructure (in an Al-Si alloy, Fig. 15d) - a high amount of eutectic phase mixture and significantly coarsened interdendritic network of the primary dendrite phase – accompanied by an increased amount of microcracks, which negatively impact the properties of the alloy material [18, 199, 200]. The above areas have not been addressed yet in the AM literature. However, these effects can be understood by modeling the effects of complex, nonlinear AM thermal history on microstructure evolution, particularly, considering a deviation of the thermal gradient from the build direction and incorporating competition between multiple thermal gradients during the microstructure simulation of dendrite materials. Interface energy and anisotropy may play a critical role in this competitive solidification microstructure selection process.

5. Effects of submicron-to-nano-scale AM solidification

5.1. Nucleation effects: columnar-to-equiaxed transition

As mentioned previously, the columnar-to-equiaxed transition (CET) removes unwanted anisotropy in mechanical properties of the AM parts. In experiments [14], CET may result due to an increase in the heat input during AM of metals (Fig. 2c). Following the solidification maps (Figs. 9c and 9d), CET can be predicted as a function of solidification conditions and alloy composition as a first approximation. It is well-known that CET is facilitated by atomic-scale nucleation events in the constitutionally undercooled liquid at or ahead of the solidification front (Fig. 16a). Empirical models such as Gäumann's expression [201] building on Hunt's criterion [202] reasonably predict the CET behavior in material under non-equilibrium conditions given by a critical value of G^n/R expressed as:

$$\frac{G^n}{R} = a\left[\frac{1}{n+1}\left(-\frac{4}{3}\frac{\pi N_0}{\ln(1-\phi)}\right)^{1/3}\right]^n, \tag{18}$$

where a and n are material constants, N_0 is the number of available nucleation sites, ϕ is the volume fraction of the equiaxed grain. Comparing with the experiments, Knapp et al. [75] found the constants for

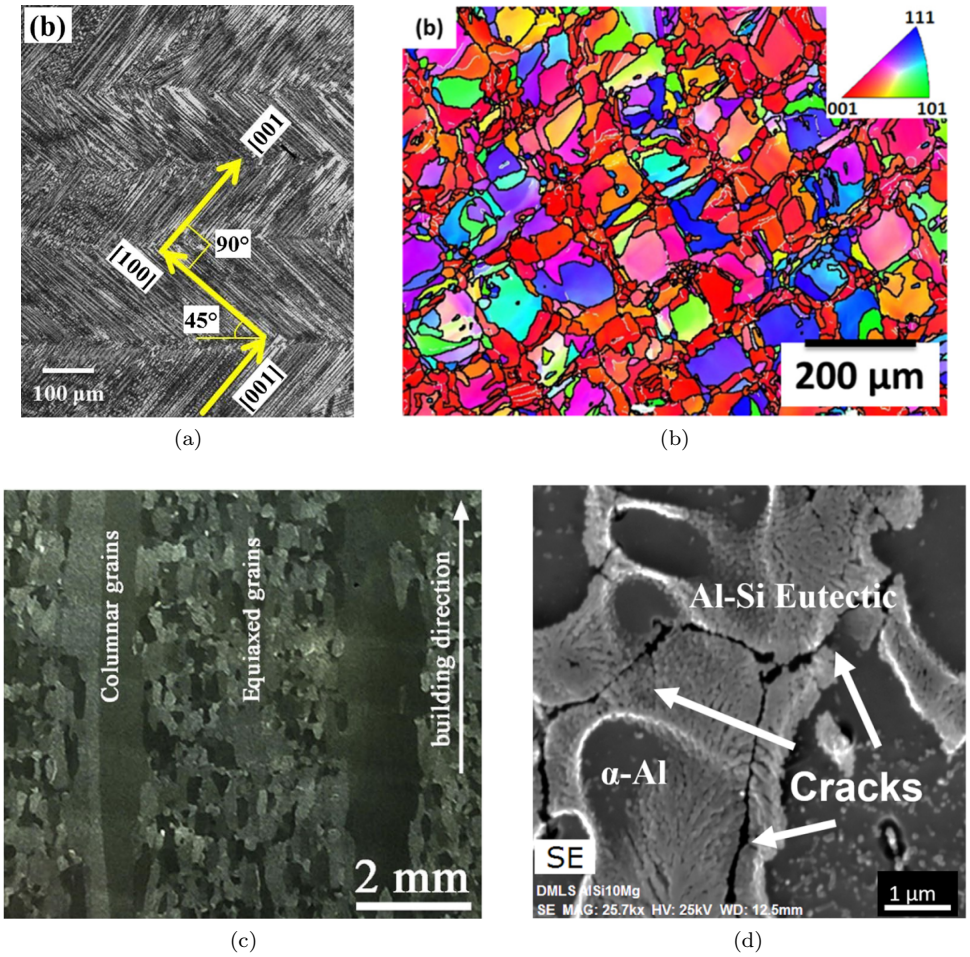

Figure 15: Unique AM microstructures are expected to have unique mechanical properties. (a) A bi-directional laser scanning path leads to the zigzag pattern in the as-printed microstructure of Inconel 718 [81]. (b) EBSD orientation map of the plane perpendicular to the build direction of as-built 17-4 PH steel showing a mosaic-type grain microstructure that can be associated to the heat input and laser scanning strategy employed (reproduced from [196], with permission from Elsevier). (c) Periodic alternate grain morphology composed by coarse columnar morphology and fine equiaxed morphology results due to multistage laser AM of Ti alloys (reproduced from [197], with permission from Elsevier). (d) A hybrid microstructure composed of dendritic, eutectic, and other secondary features result in Al-Si alloys (reproduced from [200], with permission from Springer Nature).

Inconel 718 alloy to be $a = 4.5$ K^2 s m^{-1}, $n = 2$, and $N_0 = 2.65 \times 10^{14}$ m^{-3}. Based on several studies (Fig. 16b) and analyses [202–204] on the growth and interaction of equiaxed grains with the columnar front, a fully equiaxed microstructure is expected to occur with $\phi > 0.49$ while a fully columnar microstructure is expected with $\phi < 0.0066$. A mixed columnar-equiaxed structure is expected for $0.0066 < \phi < 0.49$ [202–204]. The empirical CET models have serious limitations as they do not include many non-equilibrium effects associated with the nucleation undercooling and interface energy and, hence, are used primarily to approximate CET predictions. Therefore, controlling CET in AM of metals still remains a challenge as the underlying mechanisms are poorly understood.

Very recent experimental evidence [205–208] confirmed that the atomic structure of the liquid phase is

not fully disordered and instead develops a short-range ordering (Fig. 16c). Such atomic-scale arrangement of the liquid phase was found to significantly affect the nucleation behavior of the newly-formed phase with an epitaxial relationship developed with the parent phase, controlling the solidification texture in the final microstructure. Such ordering also influenced the attachment kinetics at the solid-liquid interface and significantly slowed down the diffusional microstructural evolution processes. The above atomistic effects can be even more drastic in the AM solidification regime as it can induce strongly out-of-equilibrium events such as solute-trapping and spinodal phase separation [144, 209], leading to unexpected and undesired metastable phases in the as-printed microstructure.

Further, the rapid cooling rate during AM increases the nucleation rate of the active phases and suppresses the grain growth, controlling grain refinement and final microstructure, particularly CET (Fig. 16d). During columnar growth, long channels of interdendritic liquid remain trapped between solidified regions. As the temperature and liquid volume fraction in the mushy region decrease, solidification shrinkage and thermal contraction in these channels produce cavities and hot tearing cracks, which may span the entire length of the columnar grain. In contrast, fine equiaxed grains are more effective in accommodating the thermal contraction strains associated with terminal solidification, leading to low tendency for defect formation [28, 29, 210]. There are observations [210] on grain morphology in Al alloys doped with Zr particles to create heterogeneous nucleation sites ahead of the solidification front that reduce the critical solidification velocity required to induce the equiaxed growth (Fig. 2a). As a result, equiaxed grains are maintained even in solidification conditions under which columnar grains are usually expected to form. Ultrarapid laser heating of Al-Si eutectic alloys led to the Si particles remaining unmolten at the end of solidification which act as heterogeneous nucleation sites in subsequent cooling, promoting equiaxed grain formation and "inoculant-free" grain refinement [211].

In the literature, simulations of heterogeneous nucleation using the PF model have taken several approaches. The most common one [212–214] uses the explicit nucleation method in which the local nucleation probability (P_n) within a sample volume (ΔV) element and a certain time interval (Δt) is given by

$$P_n(\mathbf{r}, t) = 1 - \exp(-J(\mathbf{r}, t)\Delta V \Delta t), \tag{19}$$

where J is the nucleation rate that can be estimated following the classical nucleation theory as

$$J(\mathbf{r}, t) = J_0(\mathbf{r}, t) \exp(-\Delta G^*(\mathbf{r}, t)/k_B T), \tag{20}$$

where J_0 is the prefactor, ΔG^* is the activation energy barrier of nucleation (function of critical radii of the nuclei), k_B is Boltzmann's constant, and T is absolute temperature. If P_n is larger than a numerically generated random number between 0 and 1, the nuclei are explicitly introduced into the metastable liquid

phase through a probabilistic Poisson seeding process. In another approach [213, 215], the conventional Langevin noise terms of certain magnitude satisfying the fluctuation-dissipation theorem are usually added in the PF equations of motion to generate nuclei in the liquid phase. The above approaches, however, have limitations in modeling nucleation in real materials under non-equilibrium conditions since they do not consider the effects of different crystal structures, bulk and interface free energies, anisotropy, and temperature dependence, among others [213].

In another approach [213, 216, 217], PF solidification models (Sec. 2.3) could be assisted by suitable atomistic models such as molecular dynamics (MD) or phase-field crystal (PFC) to simulate the nucleation phenomena for a quantitative study of microstructure development during rapid solidification (see (h) in Fig. 3c). In this context, a PFC model can be preferred over other models in the view of PFC as a multiscale simulation algorithm, which bridges the gap between the MD approach and PF approach by operating on diffusive time scales yet atomic length scales. Therefore, efficient integration between PF and PFC simulations could be possible. A PFC model uses a free energy functional of the density field as the order parameter (similar to the PF method), which takes a constant value in the liquid phase and a periodic function in the solid phase. In this model, any perturbation will increase the free energy, enabling the simulation of atomistic events at much larger spatial and temporal dimensions that are not easily accessible with other atomistic techniques including MD. A large variety of physical phenomena such as grain/sub-grain boundary dynamics, atomic scale structure, bulk and interface free energies, and anisotropy are automatically incorporated into the PFC model [213], thus allowing for quantitative simulation of the nucleation *mechanism* due to the liquid phase ordering discussed earlier. Note that suitable experimental measurements of the atomic-scale nucleation effects on melt-pool solidification will help design the PFC simulations [207, 208]. The PFC model parameters can also be linked to MD simulations [218, 219].

It is worth noting that other atomistic events occur during non-equilibrium AM solidification, which involves the fundamental solid-liquid and solid-solid interface properties, including interfacial energy, anisotropy parameters, attachment kinetics, and solute diffusivity. Specifically designed atomistic simulations could estimate these parameters for input to the PF model for a more predictive simulation of solidification microstructures during AM of metals [129, 130].

5.2. Microstructure features

Let us briefly discuss the submicron-to-atomic-scale microstructural features as they relate to rapid AM solidification. Depending on the alloy material and solidification conditions, a broad range of solidification cell structures, elemental segregation, and nanoprecipitate phases result (Fig. 17) [7, 8, 22, 220–222] in AM of metals. Due to the enhanced spatial and chemical resolution of these microstructural characteristics, high-resolution characterization techniques such as transmission electron microscopy (TEM) and atom probe tomography (APT) are increasingly being utilized for atomic scale microstructure and composition analysis.

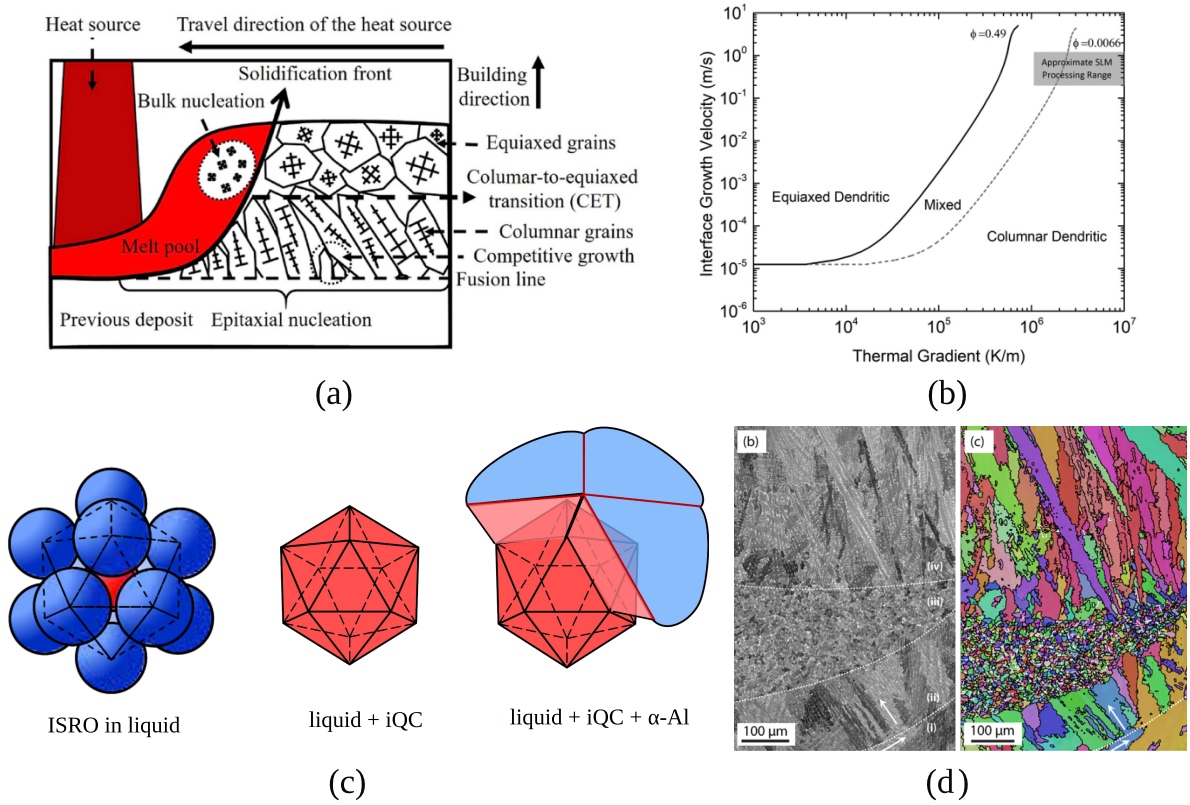

Figure 16: (Color online) (a) Schematic shows the nucleation-mediated CET behavior in the melt-pool. High R and low G values close to the melt-pool surface promote equiaxed microstructure at the end of solidification, while low R and high G values close to the bottom of melt-pool promote columnar microstructure at the beginning of solidification. (b) Solidification microstructure selection map (Type 2) demonstrates the CET behavior of a Al-10Si-Mg alloy (reproduced from [128], with permission from Elsevier) following Hunt and Gäumann [201, 202]. Typical laser parameter ranges are emphasized. SLM stands for selective laser melting. (c) Schematic of how the Icosahedral Short-Range Ordering (ISRO) in liquid affects nucleation mechanism (adapted from [207], with permission from Springer Nature). Quasicrystals (QC) are the most likely candidates to nucleate initially in an undercooled metallic liquid due to their low solid-liquid interfacial energy. Following nucleation, solid phases grow with specific crystallographic relationships. (d) Under AM conditions, many alloys tend to grow with a columnar dendritic morphology. Later, heterogeneous nucleation facilitates equiaxed grain growth at favorable regions in the undercooled liquid, leading to Columnar-to-Equiaxed Transition (CET) during AM of Inconel 718 (adapted from from [208], with permission from Elsevier). Here, the left figure is a SEM image and the right figure is the EBSD crystal orientation map of the left figure.

Due to ultrarapid cooling rates in AM, a unique hierarchical microstructure with solidification cells of size on the order of $\approx 1\,\mu m$ or below are observed within the grain structure (of size on the order of sub-millimeter) [7, 18] (Figs. 17a, 17b). In the AM solidification study of Al10SiMg alloy [18], it is reported that the average size of the grain is $12\,\mu m$, the average size of solidification cell is $0.77\,\mu m$, and the average thickness of cell boundary is $126\,nm$. The TEM studies reveal significant enrichment/microsegregation of solute elements at cell boundary regions [7] (Figs. 17b, 17c). Interestingly, microsegregation, at the atomic scale, may not be detrimental to material properties when compared to its effect on the micrometer scale. The nanoscale cell boundaries and the attending dislocation networks assist in the rapid diffusion of solute atoms, leading to more enhanced microsegregation. This impedes the dislocation motion effectively, resulting in an

outstanding strength-ductility trade-off, which is a longstanding challenge in the materials community [7].

The rapid cooling rates in AM could lead to nanometer-scale non-equilibrium solute partitioning across the solidification cells/dendrites and cell boundary/interdendritic regions [8, 220]. Alloy elements with $k_v > 1$ partition into the dendrite core regions; elements with $k_v < 1$ partition into the interdendritic regions; and some alloy elements exclusively segregate at the interface. The segregation pattern of each alloy element modifies the freezing range of the interdendritic residual liquid and engineers phase formation and stability by modifying local composition. This could lead to the unexpected formation of interdendritic secondary phases during the very end of the solidification, resulting in nucleation of highly metastable phases [223] and many undesirable heterogeneities in the as-solidified AM material [8]. The APT measurements could accurately quantify such solute partitioning behavior across nanometers wide interdendritic regions (Figs. 17d, 17e). A detailed knowledge of the influence of each element's partitioning on phase selection and freezing range could potentially help in developing strategies in terms of appropriate composition and solidification parameters adjustment for solving many longstanding challenges in metallurgical manufacturing, such as hot cracking, as illustrated in Ref. [8].

As mentioned before, depending on k_v and AM cooling rate values, solute atoms of alloy elements severely enrich the dendritic and interdendritic regions [8, 220]. Upon subsequent cooling in the solid-state, the second-phase precipitates (of size $\approx$ 10-150 nm) nucleate heterogeneously at these highly-supersaturated solute-rich regions and subsequently grow to exhibit specific morphology (e.g., globular, acicular, plate, lamellar, etc.) (Fig. 17c). The size, spatial distribution, compositional variation, volume fraction, orientation, and interfacial behavior of the precipitate phases will depend on the extent of elemental partitioning and the texture and scale of the grain/sub-grain features [193, 194]. It is to be noted that principles of solute partitioning across the solid-liquid interface can be extended to the solid-solid phase transformation, including nanoprecipitates formation. Detailed discussion of such post-solidification features is beyond the scope of the present review.

Although computationally expensive, the PF simulations of Ni-Al and Ni-Nb alloys (Fig. 8) in three-dimensions with nanometer-scale input interface thickness parameter values can generate solidification cell structures. Serial sectioning of these structures can reveal valuable information on the resulting microsegregation patterns [91] (Fig. 17f). Atomic scale PFC simulations can also be used to generate such nanoscale solidification microstructural features [216], including the solute-rich cluster formation during the early stages of precipitation [224, 225] (Fig. 17g). The solidification microstructures and the local composition, temperature, and order parameter fields can be used as inputs into a sub-grain scale phase-field model [226–229] for the simulation of subsequent solid-state phase transformation, notably precipitate phases formation as a function of composition, temperature, time, and other solid-state microstructure variables (Fig. 17h).

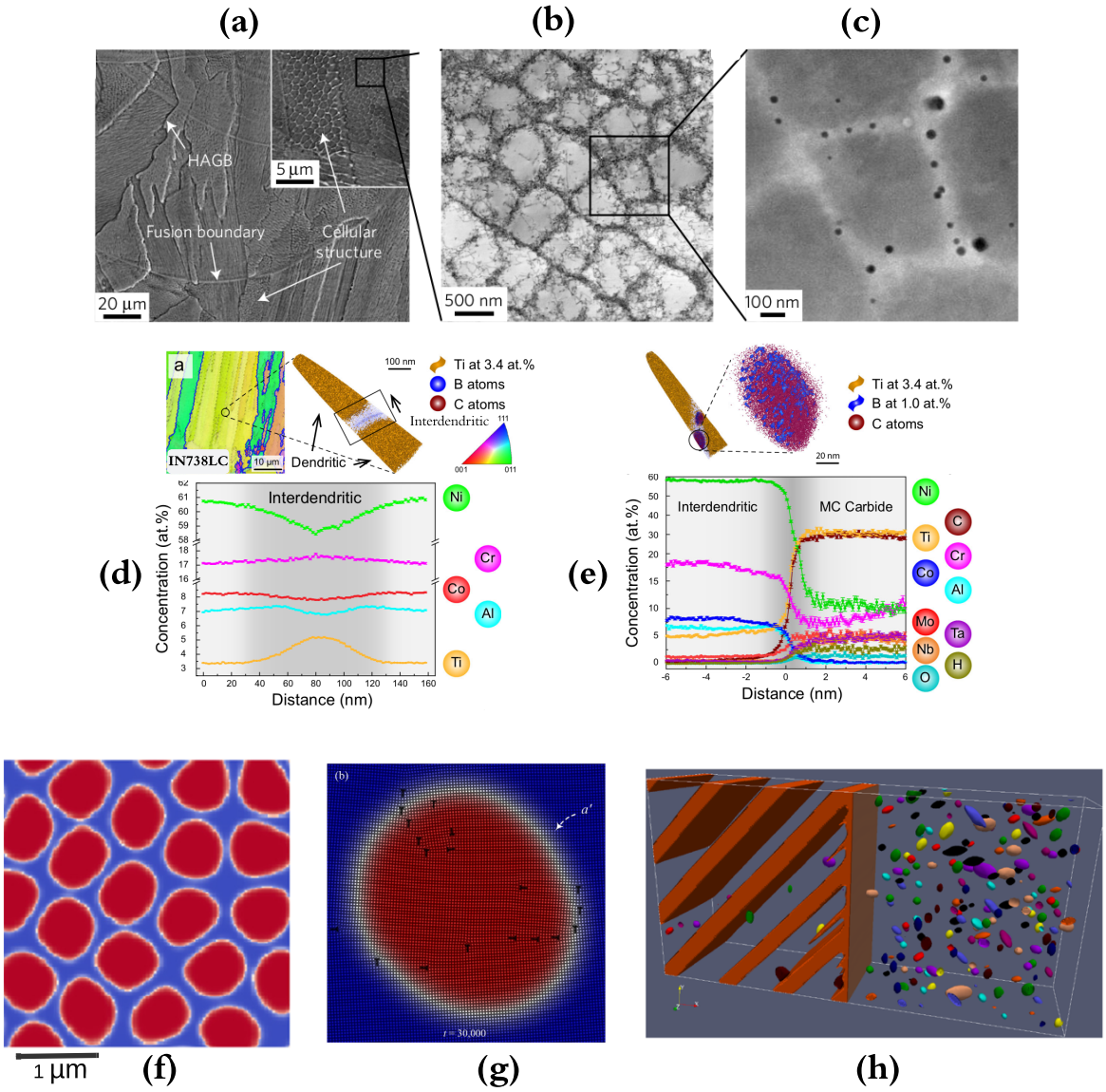

Figure 17: (Color online) Hierarchical microstructural features develop in AM of metal alloys. (a) A SEM image shows a typical melt-pool boundary (sub-millimeter scale), high angle grain boundary (HAGB, microscale), and solidification cell structure (nanoscale) in 316L steel. The inset shows solidification cells at higher magnification. The build direction is vertical. (b) A TEM image shows an enlarged view of solidification cells from Fig. 17a. (c) A TEM image shows an enlarged view of the solidification cells from Fig. 17b. Nanoscale precipitates form in the cell boundary region. (a)-(c) are reproduced from [7], with permission from Springer Nature. (d) The ATP measurements (of the intergranular region of interest as shown in the inverse pole figure map) illustrate the solute partitioning behavior of major elements in Inconel 738LC alloy across the nanoscale interdendritic region (i.e., dark grey region) (from [8]). Atomic measurements are taken from isosurfaces of a given elemental concentration to contrast between dendritic and interdendritic regions. (e) The APT analysis shows compositional variation across the (carbide) precipitate phase within the interdendritic region (from [8]). (f) A PF solidification model simulates the cell structure in AM of Inconel 718 (from [91]). Red represents cell structures and blue represents intercellular liquid. This image is a 2D section of a 3D cellular microstructure. Although not shown here, the secondary phases are expected to form in the solute-rich cell boundary regions at the end of solidification. (g) The PFC simulations of solute-rich cluster (labeled as a') formation prior to the precipitation process in Al-Cu-Mg alloy. Here, black dots indicate atomic positions. T-shaped symbols mark the edge dislocations, which act as high-diffusivity paths for the solute atoms during the process (reproduced from [225], with permission from Elsevier). (h) A sub-grain scale solid-state PF model simulates the growth of precipitate phases at a given cooling rate and temperature in AM of Ti-6Al-4V (reproduced from [227], with permission from Springer Nature). Different color represents the precipitate phase with different morphologies and orientation variants.

6. Data science approaches

Due to the sensitivity of the resulting non-equilibrium microstructures to the high number of influencing solidification and alloy parameters during rapid solidification, machine learning (ML) approaches can be very suitable for estimating the microstructure features [230–232]. The PF simulation input and output data could be a reasonable basis for developing physics-based ML algorithms, including regression, neural networks, and decision trees [231–233]. These algorithms could be reasonable reduced-order models with quantified uncertainty bounds to discover implicit knowledge and identify relationships in microstructure data sets at a much reduced computational cost. Also, the ML approaches could identify the parameters or factors critical for non-equilibrium alloy solidification and even accelerate the solver performance for partial differential equations of PF models, enhancing microstructure simulations by orders of magnitude [234]. The ML approaches might also aid in solving inverse problems [235, 236] for identifying optimal processing, material, and composition parameter windows to produce target microstructure objectives for a given application. The ML methods may also provide upscaling of materials information from atomistic to mesoscale PF models [237, 238]. Finally, the quality control in AM parts can be achieved through the control of variations (i.e., anisotropy and uncertainty) in the as-solidified microstructure. Since alloy composition, solidification conditions, and interface energy primarily contribute to the statistical variation in microstructure characteristics, uncertainty quantification (UQ) of these dynamically-evolving signatures is essential to produce benchmark-quality AM research [84, 85, 93].

7. Estimation of microstructure-properties correlations

Mechanical response of metal alloys is highly dependent on the local microstructural evolution. Therefore, a fundamental understanding of the microstructure-property relationships in AM of metals is crucial. For the sake of completeness, we will briefly mention the key approaches that could be followed to estimate mechanical characteristics (such as stress-strain behavior) of the simulated as-solidified microstructures. Due to space limitations, the present review is limited only to the as-solidified state of AM microstructures as long as they relate to the solidification models. Thus the solid-state microstructure-properties modeling had to be neglected in this review.

- A standard finite-deformation chemo-mechanically coupled phase-field (PF) model consisting of mass conservation equations and other constitutive energy and kinetic equations incorporated with appropriate micromechanical models can be used to estimate mechanical behavior [100].
- Considering the thermomechanical conversion during AM of metals, a suitable thermodynamic dislocation theory (TDT) based approach can be incorporated in the PF framework to study the effects

of several mechanical aspects, including the residual thermal stresses and structural defects, on microstructure formation [239, 240]. Similar to the PF method, TDT is also based on the premise that a dislocation microstructure must evolve following the second law of thermodynamics to a free energy minimum that involves a continuous dislocation density and a thermodynamically-defined configurational thermal history. Thus, it could be possible to predict the dislocation microstructures and interactions by combining the PF and TDT free energy functionals and correctly identifying the coupling between defect densities and PF variables. This approach could be particularly useful for modeling dislocation cells generated in AM solidification (Fig. 14c).

- When the melt-pool solidification is simulated using a solutal or thermo-solutal PF model with no mechanical components included, mechanical behavior of the resulting microstructures then can be evaluated using suitable finite element-based structural analyses [25, 60] or *via* software, e.g., Object Oriented Finite Elements (OOF) [241], which considers the microstructure, material properties, and boundary conditions as input and solves related flux or divergence equations to investigate material properties, including residual stress, distortion, and even hot tearing.

- The stress-strain behavior of as-solidified microstructures can be modeled by a "built-in" mechanical coupling of the phase and temperature fields within the PF framework using the stress equilibrium equation with elastoplastic constitutive equations for the involved solid phases, the numerical solutions of which may reveal the residual stresses in the microstructure [242–245]. Integration of a grain-scale PF model and a fast Fourier transform-based elasto-viscoplastic crystal plasticity model is employed to predict the micromechanical behavior and properties of resultant microstructures [228].

- Micromechanical models can be used to approximate the mechanical behavior of the simulated microstructures. For example, the yield stress of a given material can be correlated to the length scales of the microstructure (such as grain size, dendrite arm spacing, and lamellar spacing) and phase fractions using suitable micromechanical models, including Hall-Petch, dislocation pile-up, and other strength-hardness relations [60, 82, 246].

8. Summary, outlook, and research opportunities

The highly-localized melting, steep temperature gradient, and high growth velocity during AM solidification of metals generate strongly far-from-equilibrium microstructures often accompanied by heterogeneities such as solidification defects and texture. The underlying processes are characterized by the nonlinear interplay of physical, chemical, thermal, and mechanical phenomena that extend across multiple length and time scales, establishing a hierarchical nature of the microstructure formation process. As illustrated in this review, a deeper and more fundamental understanding of the hierarchical processes during sub-grain

and grain scales of alloy solidification is necessary for obtaining "AM-friendly" process-structure-properties connections in AM of metals. We have detailed how advanced multiscale simulation, theory, and data-driven modeling will accelerate the understanding of hierarchical microstructure evolution during AM solidification. Nevertheless, there are still many unexplored research questions and challenges related to rapid solidification dynamics and subsequent microstructure formation in AM that await to be discovered. As detailed in the following, main research opportunities are grouped into quantitative simulations; computational challenges related to high-performance computing; roles of nucleation toward columnar-to-equiaxed transition; novel classes of microstructures; roles of microstructure selection maps; the influence of crystallographic effects; as well as the processability of new alloys.

- The present review demonstrates how benchmark heat transfer FEA simulations incorporating non-equilibrium melt-pool physics will quantitatively estimate time-dependent thermal history and hence actual rapid solidification conditions in the melt-pool; and subsequent FEA structural analysis will determine residual stresses and distortions in the solidified AM part. Since these topics are quite challenging and thus rarely explored, we have discussed simple yet effective general approaches for connecting thermomechanical FEA simulations to microstructure simulations by correlating laser process parameters and solidification conditions to microstructure features, including morphological descriptors of the solidification process (e.g., dendritic, equiaxed, eutectic), length scale of the features (e.g., dendrite arm spacing), and feature volume fractions. However, there are tremendous computational challenges associated with conducting a fully-coupled computational fluid dynamics, heat transfer, structural mechanics, and microstructural evolution calculations for an AM build part. The present review highlights a practical approach, which can be undertaken to conduct above computations in a sequential (semi-coupled) manner under certain practical assumptions. Although such a strategy poses data mapping challenges associated with transferring computed data among different types of computational grids and/or finite elements (e.g., finite volume computational fluid dynamics to finite element heat transfer analysis), it can provide valuable insights into the influence of the AM process parameters on the solidification microstructure, distortions, residual stresses, and mechanical properties of the AM part. Additionally, this approach allows for incorporation of advanced constitutive models that may be needed to describe adequately the thermomechanical behavior of AM parts of complex, multicomponent alloys.

- The phase-field model has the highest fidelity among all microstructure simulation methods. A physics-rich phase-field model will allow quantitatively accurate simulation of alloy solidification under highly non-equilibrium AM conditions. The physics governing melt convection, heat flow, solute transport, solid-liquid interfacial energy, crystal anisotropy, and curvature effects must be modeled with non-equilibrium parameter settings for microstructure simulation during AM solidification. However, this

makes the phase-field simulations computationally very intensive. Thus, it becomes prohibitive to simulate the AM solidification problem on the scale of the full-melt-pool or a large AM part, demanding the simulation run time to be significantly reduced. To solve these challenges, the emerging exascale heterogeneous (CPU+GPU) HPC architectures with their modern software design and algorithm and enhanced computational methodology could be deployed for conducting large scale, high-fidelity microstructural evolution simulation. Such capability would enable calculations that require solving equations involving billions of variables (degrees of freedom) and significant number of micro time steps for the first time [125, 247]. Thus, micro- and mesoscale (i.e., sub-grain and grain scale) phase-field simulations will no longer need to be restricted to the scale of representative volume element, but may allow performing microscale-resolved full-melt-pool simulations on continuum scales [248]. The `Tusas` phase-field code (developed by the authors) mentioned in this review is part of the ExaAM (and parent ECP) project [19], which utilizes advanced software (MPI+Kokkos parallelization with hybrid CPU+GPU implementation) and exascale hardware and has demonstrated ideal strong and weak parallel scaling with over four billion degrees-of-freedom on over 25 thousand GPUs on Summit supercomputer [95]. Currently, `Tusas` is being used for quantitatively accurate full-melt-pool phase-field simulations of microstructure evolution during alloy solidification in 3D (Fig. 18) [249], allowing comparison between real-time predictive modeling results of AM with suitable experimental measurements. To the best of our knowledge, such a study has not been done.

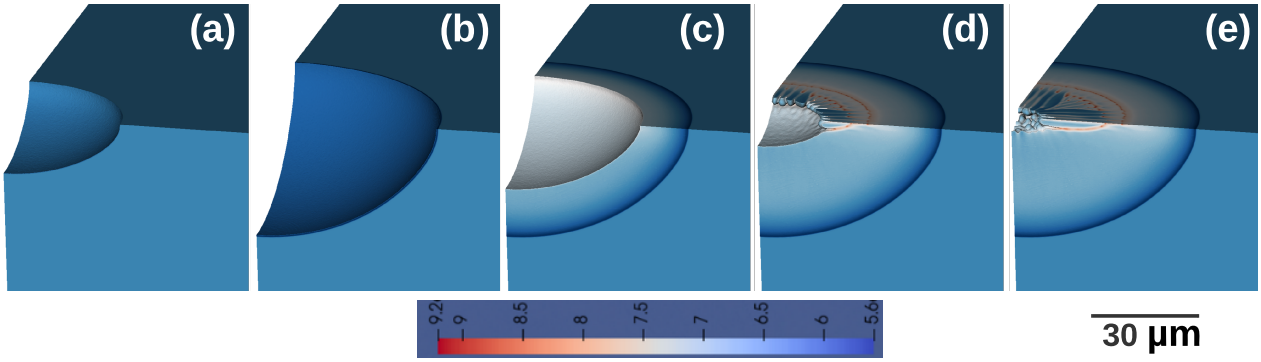

Figure 18: (Color online) Exascale-ready `Tusas` phase-field framework [45] is used to simulate the solidification behavior of an entire laser spot melt of Ni-7.34 % Al alloy in 3D. In a simulation domain of 0.5 mm × 0.5 mm × 0.5 mm) [249], we only show the zoomed details of melting and solidification regions within the domain. The temporal evolution of the composition field (shown by the color scale bar) demonstrates the time-dependent microstructure evolution due to the variation of G and R in the solidifying melt-pool: (a) early melting; (b) transition from melting to freezing; (c) plane front solidification; (d) transition from planar to cellular/dendritic morphology; and (e) steady-state cellular/dendritic morphology develops over the entire solidified melt-pool. Here, the composition is presented in mass fraction. The simulation utilizes 3072 GPUs for a total run time of 42 hours on Summit [117].

- As explained earlier, the as-solidified microstructure is most critical for AM since post-AM operations (e.g., heat treatment) not only reduce the economic attractiveness of AM but they may lead to harmful

consequences such as grain growth and coarsening and hence they may not represent a straightforward choice for mitigating microstructural heterogeneities including solidification defects and texture. To solve these challenges, we detail in this review that a thorough understanding of microstructure selection (e.g., columnar, dendritic, equiaxed, eutectic, peritectic, banded, and hybrid) and their interactions in relation to the length-scale, type, and amount of the microstructure features; solidification defects; competitive growth among different classes of microstructures; morphological transition; compositional variation; crystallographic interfacial effects; and nucleation events during AM solidification will guide microstructure design of the as-solidified material to suit a specific application. Also, extremely large values of solid-liquid interface velocity (or cooling rate) typical of non-equilibrium AM solidification generate sub-grain and grain features of ultra-fine length scales; in this regime, new microstructure physics and equations such as crystallographic effects are yet to be investigated, making them a worthwhile goal for basic research.

- In the context of AM, an essential task is to study the formation of defects such as microporosity, precipitation of secondary phases of eutectics or peritectics, and hot cracking during the late stages of solidification. A subsequent related task is to model the solid-state phase transformation processes such as competitive precipitation and residual stresses in the as-solidified microstructure that require input from solidification microstructure calculations [50, 190, 250]. With an integrated solidification and solid-state transformation phase-field modeling, the whole AM process can be evaluated in order to find a better way to prepare the as-solidified microstructure suitable for meeting service requirements. Such a quantitatively accurate modeling framework could also be used for process design, that is, to accurately predict the effect of processing conditions on microstructure formation, the knowledge of which will accelerate the processability/printability of many metallic alloys, which are not yet suitable for non-equilibrium AM processing.

- Of practical importance is to predict the process-structure relationships when numerical simulations are not feasible or become computationally unaffordable. In this review, we have systematically detailed the analytical expressions that could be used as reduced-order models (ROMs) to rapidly approximate the morphological descriptors of the solidification process (e.g., dendritic, eutectic, and peritectic), the length scale of features (e.g., dendrite arm spacing, lamellar spacing), and compositional variation (e.g., microsegregation). Although these analytical expressions may have limitations during the non-equilibrium AM solidification, they could be quite informative in the frame of AM when the sub-grain and grain structures become very sensitive to processing conditions. Collectively, these analytical expressions can also be used to create a variety of solidification microstructure selection (SMS) maps (G *vs.* R and R *vs.* C_0 or G/R *vs.* C_0) for a concise representation of the solidification morphology and defects that may form for a set of alloy composition and solidification conditions. These maps

can further be correlated to processability/printability maps (P *vs.* V) to evaluate the optimal process, solidification, and alloy parameter windows in terms of microstructure selection, morphological transition, compositional variation, and defects. The SMS maps also allow for rapid assessment of a vast parameter space and act as a guide for more detailed numerical simulations, enabling alloy, microstructure, and processing development during AM.

- Alloys that solidify in cubic crystal structures are usually affected by strong anisotropy due to the formation of coarse columnar microstructure with a preferred orientation/texture. Novel microstructure development in AM could be possible *via* making use of suitable phase transformation, e.g., peritectic reactions, which may lead to a homogeneous fine-grained microstructure without preferred crystallographic grain/phase orientation. Also, the deformation-induced phase transformations may lead to microstructure refinement and weak texture formation beneficial for AM applications [251]. It is important to model the gradient microstructure formation in functionally graded materials (FGMs), which are characterized by spatial variations in compositions/constituents and/or microstructure features (e.g., grain size, texture, etc.) along single or multiple directions to achieve exceptional mechanical properties along the desired gradient direction [7, 10, 252]. Also, the study of as-solidified microstructures in which the 'soft' and 'hard' regions correspond to the coarse grains/soft phase and fine grains/hard phase may also lead to new research insights toward improved strength-ductility synergy in heterogeneous materials [252]. Significant spatial deviation in local chemical composition across the microstructure still is a major issue in AM of specialty alloys as it may lead to unique microstructure irregularities such as periodic columnar-to-equiaxed transition; and as has been demonstrated, e.g., for shape memory alloys (SMA), where phase transformation is strongly affected by microstructural and compositional heterogeneity [253, 254]. As discussed in this review, carefully designed phase-field simulations could be used to obtain precise information on the above microstructure evolution mechanisms. Note that the above new classes of microstructures are not accessible through conventional manufacturing methods *via* casting, forging, or rolling.

- Ultrarapid cooling rates ($\approx 10^5$ K/s to 10^8 K/s) during AM often lead to a highly non-equilibrium solidification process, altering the solidification path and final microstructure. This may even result in the so-called "skipping" of thermodynamically stable phases that do not have enough time to form *via* diffusion-controlled growth processes. Recent experiments [196, 255, 256] demonstrate the possibility of partially or entirely by-passing the austenite phase and resulting in a stable ferritic microstructure at the end of solidification of δ ferrite in LPBF of 17–4PH steels. Thus, the final microstructure observed in these and related alloy systems is the one obtained directly after melt-pool solidification, without any further phase transformation occurring in the subsequent solid-state AM processing. Interestingly, when R exceeds R_{ab} (Eq. (11)), a diffusionless, plane-front solidification with

complete solute-trapping and a segregation-free microstructure is obtained in these alloy systems. Also, a unique, highly anisotropic "mosaic-type" microstructure (Fig. 15b) results in these alloys in which the grains/phases inside each mosaic has different crystallographic orientations as compared to those of grains/phases in the adjacent mosaics [196, 257]. The above observations demonstrate the range of microstructure and phase control options available in metal AM. A phase-field model with a judicious selection of composition, different G and R conditions, and an appropriate description of interfacial anisotropy may explain the formation of such diversity of microstructures obtained in metal AM.

- New insights are also expected from the investigation of the atomistic mechanisms behind nucleation which are not yet well understood in the regime of AM solidification. Very recent measurements confirm that metastable quasicrystals of icosahedral phase nucleate first in the heterogeneous liquid molten pool that leads to the development of grain structure in AM, particularly columnar-to-equiaxed transition [207, 208]. Consequently, new analytical models will be required to predict CET since Hunt's and other derivative CET models may become inappropriate under such highly non-equilibrium solidification conditions. Moreover, the knowledge of solidification pathways and the morphological transition is considerably less advanced in the AM solidification regime (high G and high R limit close to R_{ab}). With extremely large values of temperature gradient in AM when the zone of undercooled liquid head of the solid-liquid interface reaches a few nanometer long, are the analytical criteria to predict morphological transition still remain valid? A detailed investigation is required to shed light on the above technical issue. As discussed in this review, phase-field models must be assisted by specifically designed atomistic simulations such as *via* phase-field crystal technique to model the effects of nucleation and other interfacial phenomena on the microstructure formation during AM solidification.

- We present a comprehensive review to critically address the solidification microstructure evolution in AM, the prediction and control of which can be quantitatively studied using numerical simulations. According to the best knowledge of the authors, such a review has not been conducted before. We have detailed that phase-field simulations under appropriate physical and numerical conditions can produce quantitatively accurate microstructure formation for given AM conditions, enabling a more accurate evaluation of process-microstructure relationships in AM of metals. We have also mentioned various numerical means of estimating the mechanical behavior of the as-solidified microstructures. Collectively, process-structure-properties connections can be made for a given material under non-equilibrium AM solidification. Such information could be helpful for alloy, microstructure, and process design to suit a given application.

Finally, the research findings and potential future enhancements mentioned above are expected to develop a detailed understanding of the underlying mechanisms of non-equilibrium solidification dynamics and mi-

crostructure formation during AM of metals. Consequently, these studies will potentially advance strategies to identify "AM-friendly" robust microstructures to achieve target material properties (e.g., those needed for single crystal turbine blades, hot-section gas turbine components etc.). Though the present review focuses only on metallic alloys, the overall microstructure control principles discussed here could be applied to diverse families of materials, including superalloys, intermetallics, and composites. These materials could be modeled efficiently using a multi-component multi-phase-field model, accelerating broad adoption of AM for industry use and enabling the design of new alloy systems within the rapid solidification regime.

Acknowledgments

S. Ghosh acknowledges the support of Faculty Initiation Grant from Sponsored Research & Industrial Consultancy Office, Indian Institute of Technology Roorkee and Science and Engineering Research Board, Government of India. R. Arroyave acknowledges the support of the NASA-ESI Program under Grant Number 80NSSC21K0223. C. K. Newman's work was supported by the U.S. Department of Energy through Los Alamos National Laboratory. Los Alamos National Laboratory is operated by Triad National Security, LLC, for the National Nuclear Security Administration of the U.S. Department of Energy (Contract No. 89233218CNA000001) and by the Exascale Computing Project (17-SC-20-SC), a joint project of the U.S. Department of Energy's Office of Science and National Nuclear Security Administration, responsible for delivering a capable exascale ecosystem, including software, applications, and hardware technology, to support the nation's exascale computing imperative (LA-UR-22-32341).

References

[1] S. Ghosh, Predictive modeling of solidification during laser additive manufacturing of nickel superalloys: recent developments, future directions, Materials Research Express 5 (1) (2018) 012001.

[2] D. Herzog, V. Seyda, E. Wycisk, C. Emmelmann, Additive manufacturing of metals, Acta Materialia 117 (2016) 371 – 392.

[3] T. DebRoy, H. Wei, J. Zuback, T. Mukherjee, J. Elmer, J. Milewski, A. Beese, A. Wilson-Heid, A. De, W. Zhang, Additive manufacturing of metallic components–process, structure and properties, Progress in Materials Science 92 (2018) 112–224.

[4] B. Blakey-Milner, P. Gradl, G. Snedden, M. Brooks, J. Pitot, E. Lopez, M. Leary, F. Berto, A. du Plessis, Metal additive manufacturing in aerospace: A review, Materials & Design 209 (2021) 110008.

[5] P. Gradl, D. C. Tinker, A. Park, O. R. Mireles, M. Garcia, R. Wilkerson, C. Mckinney, Robust metal additive manufacturing process selection and development for aerospace components, Journal of Materials Engineering and Performance (2022) 1–32.

[6] P. Collins, D. Brice, P. Samimi, I. Ghamarian, H. Fraser, Microstructural control of additively manufactured metallic materials, Annu. Rev. Mater. Res 46 (1) (2016) 63–91.

[7] Y. M. Wang, T. Voisin, J. T. McKeown, J. Ye, N. P. Calta, Z. Li, Z. Zeng, Y. Zhang, W. Chen, T. T. Roehling, et al., Additively manufactured hierarchical stainless steels with high strength and ductility, Nature materials 17 (1) (2018) 63–71.

[8] Z. Sun, Y. Ma, D. Ponge, S. Zaefferer, E. A. Jägle, B. Gault, A. D. Rollett, D. Raabe, Thermodynamics-guided alloy and process design for additive manufacturing, Nature Communications 13 (1) (2022) 1–12.

[9] S. Chen, Y. Tong, P. K. Liaw, Additive manufacturing of high-entropy alloys: a review, Entropy 20 (12) (2018) 937.

[10] C. Zhang, F. Chen, Z. Huang, M. Jia, G. Chen, Y. Ye, Y. Lin, W. Liu, B. Chen, Q. Shen, et al., Additive manufacturing of functionally graded materials: A review, Materials Science and Engineering: A 764 (2019) 138209.

[11] L. Zhou, A. Mehta, B. McWilliams, K. Cho, Y. Sohn, Microstructure, precipitates and mechanical properties of powder bed fused Inconel 718 before and after heat treatment, Journal of Materials Science & Technology 35 (6) (2019) 1153–1164.

[12] A. Gamon, E. Arrieta, P. R. Gradl, C. Katsarelis, L. E. Murr, R. B. Wicker, F. Medina, Microstructure and hardness comparison of as-built Inconel 625 alloy following various additive manufacturing processes, Results in Materials 12 (2021) 100239.

[13] W. M. Tucho, P. Cuvillier, A. Sjolyst-Kverneland, V. Hansen, Microstructure and hardness studies of Inconel 718 manufactured by selective laser melting before and after solution heat treatment, Materials Science and Engineering: A 689 (2017) 220–232.

[14] C. Körner, M. Markl, J. A. Koepf, Modeling and simulation of microstructure evolution for additive manufacturing of metals: a critical review, Metallurgical and Materials Transactions A 51 (10) (2020) 4970–4983.

[15] N. Kouraytem, J. Varga, B. Amin-Ahmadi, H. Mirmohammad, R. A. Chanut, A. D. Spear, O. T. Kingstedt, A recrystallization heat-treatment to reduce deformation anisotropy of additively manufactured Inconel 718, Materials & Design 198 (2021) 109228.

[16] W. J. Sames, F. A. List, S. Pannala, R. R. Dehoff, S. S. Babu, The metallurgy and processing science of metal additive manufacturing, International Materials Reviews 61 (5) (2016) 315–360.

[17] A. Hadadzadeh, B. S. Amirkhiz, A. Odeshi, M. Mohammadi, Dynamic loading of direct metal laser sintered AlSi10Mg alloy: Strengthening behavior in different building directions, Materials & Design 159 (2018) 201–211.

[18] A. Hadadzadeh, B. S. Amirkhiz, A. Odeshi, J. Li, M. Mohammadi, Role of hierarchical microstructure of additively manufactured AlSi10Mg on dynamic loading behavior, Additive Manufacturing 28 (2019) 1–13.

[19] ExaAM: Transforming Additive Manufacturing through Exascale Simulation, `https://www.exascaleproject.org/research-project/exaam/` (2022).

[20] ExaAM: Transforming Additive Manufacturing through Exascale Simulation, `https://www.ornl.gov/project/exaam-transforming-additive-manufacturing-through-exascale-simulation` (2022).

[21] L. Scime, J. Beuth, Melt pool geometry and morphology variability for the Inconel 718 alloy in a laser powder bed fusion additive manufacturing process, Additive Manufacturing 29 (2019) 100830.

[22] Z. Liu, D. Zhao, P. Wang, M. Yan, C. Yang, Z. Chen, J. Lu, Z. Lu, Additive manufacturing of metals: Microstructure evolution and multistage control, Journal of Materials Science & Technology 100 (2022) 224–236.

[23] G. Boussinot, M. Apel, J. Zielinski, U. Hecht, J. Schleifenbaum, Strongly out-of-equilibrium columnar solidification during laser powder-bed fusion in additive manufacturing, Physical Review Applied 11 (1) (2019) 014025.

[24] Y.-L. Kuo, S. Horikawa, K. Kakehi, The effect of interdendritic δ phase on the mechanical properties of alloy 718 built up by additive manufacturing, Materials & Design 116 (2017) 411–418.

[25] T. Mukherjee, W. Zhang, T. DebRoy, An improved prediction of residual stresses and distortion in additive manufacturing, Computational Materials Science 126 (2017) 360–372.

[26] O. Lopez-Botello, U. Martinez-Hernandez, J. Ramírez, C. Pinna, K. Mumtaz, Two-dimensional simulation of grain structure growth within selective laser melted AA-2024, Materials & Design 113 (2017) 369–376.

[27] L. Gránásy, G. Tegze, G. I. Tóth, T. Pusztai, Phase-field crystal modelling of crystal nucleation, heteroepitaxy and patterning, Philosophical Magazine 91 (1) (2011) 123–149.

[28] Y. Tian, D. McAllister, H. Colijn, M. Mills, D. Farson, M. Nordin, S. Babu, Rationalization of microstructure heterogeneity in Inconel 718 builds made by the direct laser additive manufacturing process, Metallurgical and Materials Transactions A 45 (10) (2014) 4470–4483.

[29] Y. Kok, X. P. Tan, P. Wang, M. Nai, N. H. Loh, E. Liu, S. B. Tor, Anisotropy and heterogeneity of microstructure and mechanical properties in metal additive manufacturing: A critical review, Materials & Design 139 (2018) 565–586.

[30] T. G. Gallmeyer, S. Moorthy, B. B. Kappes, M. J. Mills, B. Amin-Ahmadi, A. P. Stebner, Knowledge of process-structure-property relationships to engineer better heat treatments for laser powder bed fusion additive manufactured inconel 718, Additive Manufacturing 31 (2020) 100977.

[31] M. Laleh, E. Sadeghi, R. I. Revilla, Q. Chao, N. Haghdadi, A. E. Hughes, W. Xu, I. De Graeve, M. Qian, I. Gibson, et al., Heat treatment for metal additive manufacturing, Progress in Materials Science (2022) 101051.

[32] E. Chlebus, K. Gruber, B. Kuźnicka, J. Kurzac, T. Kurzynowski, Effect of heat treatment on the microstructure and mechanical properties of Inconel 718 processed by selective laser melting, Materials Science and Engineering: A 639 (2015) 647–655.

[33] M. M. Francois, A. Sun, W. E. King, N. J. Henson, D. Tourret, C. A. Bronkhorst, N. N. Carlson, C. K. Newman, T. S. Haut, J. Bakosi, et al., Modeling of additive manufacturing processes for metals: Challenges and opportunities, Current Opinion in Solid State and Materials Science 21 (4) (2017) 198–206.

[34] S. A. H. Motaman, F. Kies, P. Köhnen, M. Létang, M. Lin, A. Molotnikov, C. Haase, Optimal design for metal additive manufacturing: an integrated computational materials engineering (ICME) approach, JOM 72 (2020) 1092–1104.

[35] S. M. Hashemi, S. Parvizi, H. Baghbanijavid, A. T. Tan, M. Nematollahi, A. Ramazani, N. X. Fang, M. Elahinia, Computational modelling of process–structure–property–performance relationships in metal additive manufacturing: A review, International Materials Reviews 67 (1) (2022) 1–46.

[36] J. H. K. Tan, S. L. Sing, W. Y. Yeong, Microstructure modelling for metallic additive manufacturing: A review, Virtual and Physical Prototyping 15 (1) (2020) 87–105.

[37] W. Yan, Y. Lian, C. Yu, O. L. Kafka, Z. Liu, W. K. Liu, G. J. Wagner, An integrated process–structure–property modeling framework for additive manufacturing, Computer Methods in Applied Mechanics and Engineering 339 (2018) 184–204.

[38] J. Smith, W. Xiong, W. Yan, S. Lin, P. Cheng, O. L. Kafka, G. J. Wagner, J. Cao, W. K. Liu, Linking process, structure, property, and performance for metal-based additive manufacturing: computational approaches with experimental support, Computational Mechanics 57 (4) (2016) 583–610.

[39] T. Gatsos, K. A. Elsayed, Y. Zhai, D. A. Lados, Review on computational modeling of process–microstructure–property relationships in metal additive manufacturing, JOM 72 (1) (2020) 403–419.

[40] J. Li, X. Zhou, M. Brochu, N. Provatas, Y. F. Zhao, Solidification microstructure simulation of Ti-6Al-4V in metal additive manufacturing: A review, Additive Manufacturing 31 (2020) 100989.

[41] Z. Zhang, Z. Tan, X. Yao, C. Hu, P. Ge, Z. Wan, J. Li, Q. Wu, Numerical methods for microstructural evolutions in laser additive manufacturing, Computers & Mathematics with Applications 78 (7) (2019) 2296–2307.

[42] W. W. Mullins, R. F. Sekerka, Stability of a planar interface during solidification of a dilute binary alloy, Journal of Applied Physics 35 (2) (1964) 444–451.

[43] W. J. Boettinger, J. A. Warren, C. Beckermann, A. Karma, Phase-field simulation of solidification, Annu. Rev. Mater. Res. 32 (2002) 163–194.

[44] I. Steinbach, Phase-field models in materials science, Modelling and Simulation in Materials Science and Engineering 17 (2009) 073001.

[45] C. Newman, et al., Tusas, `https://github.com/chrisknewman/tusas` (2020).

[46] A. Zinoviev, O. Zinovieva, V. Ploshikhin, V. Romanova, R. Balokhonov, Evolution of grain structure during laser additive manufacturing. simulation by a cellular automata method, Materials & Design 106 (2016) 321–329.

[47] A. Rai, M. Markl, C. Körner, A coupled Cellular Automaton-Lattice Boltzmann model for grain structure simulation during additive manufacturing, Computational Materials Science 124 (2016) 37–48.

[48] R. Shi, S. A. Khairallah, T. T. Roehling, T. W. Heo, J. T. McKeown, M. J. Matthews, Microstructural control in metal laser powder bed fusion additive manufacturing using laser beam shaping strategy, Acta Materialia 184 (2020) 284–305.

[49] T. M. Rodgers, J. D. Madison, V. Tikare, Simulation of metal additive manufacturing microstructures using kinetic Monte Carlo, Computational Materials Science 135 (2017) 78–89.

[50] T. Keller, G. Lindwall, S. Ghosh, L. Ma, B. Lane, F. Zhang, U. R. Kattner, E. A. Lass, J. C. Heigel, Y. Idell, M. E. Williams, A. J. Allen, J. E. Guyer, L. E. Levine, Application of Finite Element,

Phase-field, and CALPHAD-based Methods to Additive Manufacturing of Ni-based Superalloys, Acta Materialia 139 (2017) 244–253.

[51] K. Karayagiz, L. Johnson, R. Seede, V. Attari, B. Zhang, X. Huang, S. Ghosh, T. Duong, I. Karaman, A. Elwany, et al., Finite interface dissipation phase field modeling of Ni-Nb under additive manufacturing conditions, Acta Materialia 185 (2020) 320–339.

[52] P. Promoppatum, S.-C. Yao, P. C. Pistorius, A. D. Rollett, A comprehensive comparison of the analytical and numerical prediction of the thermal history and solidification microstructure of Inconel 718 products made by laser powder-bed fusion, Engineering 3 (5) (2017) 685–694.

[53] S. Ghosh, L. Ma, L. E. Levine, R. E. Ricker, M. R. Stoudt, J. C. Heigel, J. E. Guyer, Single-track melt-pool measurements and microstructures in Inconel 625, JOM 70 (6) (2018) 1011–1016.

[54] ABAQUS, version 6.14, Dassault Systémes simulia Corp., Providence, RI., USA (2013).

[55] ANSYS Academic Research, Release 17.2 (2015).

[56] FLOW-3D, version 2023R1, Santa Fe, NM (2023).

[57] COMSOL Multiphysics, version 6.1, Stockholm, Sweden (2022).

[58] S. Ghosh, L. Ma, N. Ofori-Opoku, J. E. Guyer, On the primary spacing and microsegregation of cellular dendrites in laser deposited Ni-Nb alloys, Modelling and simulation in materials science and engineering 25 (6) (2017) 065002.

[59] A. Farzadi, M. Do-Quang, S. Serajzadeh, A. Kokabi, G. Amberg, Phase-field simulation of weld solidification microstructure in an Al-Cu alloy, Modelling and Simulation in Materials Science and Engineering 16 (6) (2008) 065005.

[60] S. Ghosh, K. McReynolds, J. E. Guyer, D. Banerjee, Simulation of temperature, stress and microstructure fields during laser deposition of Ti-6Al-4V, Modelling and simulation in materials science and engineering 26 (7) (2018) 075005.

[61] C. Li, C. Fu, Y. Guo, F. Fang, A multiscale modeling approach for fast prediction of part distortion in selective laser melting, Journal of materials processing technology 229 (2016) 703–712.

[62] O. D. L. Strack, Finite Differences and Finite Elements, Cambridge University Press, Cambridge, UK, 2017, pp. 403–422. doi:10.1017/9781316563144.011.

[63] M. Bayat, S. Mohanty, J. H. Hattel, A systematic investigation of the effects of process parameters on heat and fluid flow and metallurgical conditions during laser-based powder bed fusion of Ti6Al4V alloy, International Journal of Heat and Mass Transfer 139 (2019) 213–230.

[64] D. Rosenthal, The theory of moving sources of heat and its application to metal treatments, Trans. ASME 68 (1946) 849–866.

[65] W. Guo, A. Kar, Determination of weld pool shape and temperature distribution by solving three-dimensional phase change heat conduction problem, Science and Technology of Welding and Joining 5 (5) (2000) 317–323.

[66] J. Goldak, A. Chakravarti, M. Bibby, A new finite element model for welding heat sources, Metallurgical Transactions B 15 (2) (1984) 299–305.

[67] J. Smith, W. Xiong, J. Cao, W. K. Liu, Thermodynamically consistent microstructure prediction of additively manufactured materials, Computational Mechanics 57 (3) (2016) 359–370.

[68] J.-O. Andersson, T. Helander, L. Höglund, P. Shi, B. Sundman, Thermo-Calc & DICTRA, computational tools for materials science, Calphad 26 (2) (2002) 273 – 312.

[69] Y.-H. Siao, C.-D. Wen, Examination of molten pool with marangoni flow and evaporation effect by simulation and experiment in selective laser melting, International Communications in Heat and Mass Transfer 125 (2021) 105325.

[70] J. I. Arrizubieta, A. Lamikiz, F. Klocke, S. Martínez, K. Arntz, E. Ukar, Evaluation of the relevance of melt pool dynamics in laser material deposition process modeling, International Journal of Heat and Mass Transfer 115 (2017) 80–91.

[71] M. Zheng, L. Wei, J. Chen, Q. Zhang, C. Zhong, X. Lin, W. Huang, A novel method for the molten pool and porosity formation modelling in selective laser melting, International Journal of Heat and Mass Transfer 140 (2019) 1091–1105.

[72] Y. Zhao, Y. Koizumi, K. Aoyagi, D. Wei, K. Yamanaka, A. Chiba, Molten pool behavior and effect of fluid flow on solidification conditions in selective electron beam melting (SEBM) of a biomedical Co-Cr-Mo alloy, Additive Manufacturing 26 (2019) 202–214.

[73] S. A. Khairallah, A. T. Anderson, A. Rubenchik, W. E. King, Laser powder-bed fusion additive manufacturing: Physics of complex melt flow and formation mechanisms of pores, spatter, and denudation zones, Acta Materialia 108 (2016) 36–45.

[74] S. Al-Bermani, M. Blackmore, W. Zhang, I. Todd, The origin of microstructural diversity, texture, and mechanical properties in electron beam melted Ti-6Al-4V, Metallurgical and materials transactions a 41 (2010) 3422–3434.

[75] G. L. Knapp, N. Raghavan, A. Plotkowski, T. Debroy, Experiments and simulations on solidification microstructure for Inconel 718 in powder bed fusion electron beam additive manufacturing, Additive Manufacturing 25 (2019) 511–521.

[76] M. L. Griffith, M. T. Ensz, J. D. Puskar, C. V. Robino, J. A. Brooks, J. A. Philliber, J. E. Smugeresky, W. Hofmeister, Understanding the microstructure and properties of components fabricated by laser engineered net shaping (lens), MRS Online Proceedings Library (OPL) 625 (2000) 9.

[77] Y. Zhai, D. A. Lados, E. J. Brown, G. N. Vigilante, Understanding the microstructure and mechanical properties of ti-6al-4v and inconel 718 alloys manufactured by laser engineered net shaping, Additive Manufacturing 27 (2019) 334–344.

[78] R. Ye, J. E. Smugeresky, B. Zheng, Y. Zhou, E. J. Lavernia, Numerical modeling of the thermal behavior during the lens® process, Materials Science and Engineering: A 428 (1-2) (2006) 47–53.

[79] N. Shamsaei, A. Yadollahi, L. Bian, S. M. Thompson, An overview of direct laser deposition for additive manufacturing; part ii: Mechanical behavior, process parameter optimization and control, Additive manufacturing 8 (2015) 12–35.

[80] M. Bermingham, D. StJohn, J. Krynen, S. Tedman-Jones, M. Dargusch, Promoting the columnar to equiaxed transition and grain refinement of titanium alloys during additive manufacturing, Acta Materialia 168 (2019) 261–274.

[81] H. Wei, J. Mazumder, T. DebRoy, Evolution of solidification texture during additive manufacturing, Scientific reports 5 (1) (2015) 1–7.

[82] V. Manvatkar, A. De, T. DebRoy, Heat transfer and material flow during laser assisted multi-layer additive manufacturing, Journal of Applied Physics 116 (12) (2014) 124905.

[83] Z. Gan, H. Liu, S. Li, X. He, G. Yu, Modeling of thermal behavior and mass transport in multi-layer laser additive manufacturing of Ni-based alloy on cast iron, International Journal of Heat and Mass Transfer 111 (2017) 709–722.

[84] Z. Gan, Y. Lian, S. E. Lin, K. K. Jones, W. K. Liu, G. J. Wagner, Benchmark study of thermal behavior, surface topography, and dendritic microstructure in selective laser melting of Inconel 625, Integrating Materials and Manufacturing Innovation 8 (2) (2019) 178–193.

[85] L. Levine, B. Lane, J. Heigel, K. Migler, M. Stoudt, T. Phan, R. Ricker, M. Strantza, M. Hill, F. Zhang, et al., Outcomes and conclusions from the 2018 am-bench measurements, challenge problems, modeling submissions, and conference, Integrating Materials and Manufacturing Innovation 9 (1) (2020) 1–15.

[86] Z. Luo, Y. Zhao, A survey of finite element analysis of temperature and thermal stress fields in powder bed fusion additive manufacturing, Additive Manufacturing 21 (2018) 318–332.

[87] E. R. Denlinger, J. C. Heigel, P. Michaleris, Residual stress and distortion modeling of electron beam direct manufacturing Ti-6Al-4V, Proceedings of the Institution of Mechanical Engineers, Part B: Journal of Engineering Manufacture 229 (10) (2015) 1803–1813.

[88] E. R. Denlinger, M. Gouge, J. Irwin, P. Michaleris, Thermomechanical model development and in situ experimental validation of the laser powder-bed fusion process, Additive Manufacturing 16 (2017) 73–80.

[89] X. Lu, X. Lin, M. Chiumenti, M. Cervera, J. Li, L. Ma, L. Wei, Y. Hu, W. Huang, Finite element analysis and experimental validation of the thermomechanical behavior in laser solid forming of Ti-6Al-4V, Additive Manufacturing 21 (2018) 30–40.

[90] X. Huang, R. Seede, K. Karayagiz, B. Zhang, I. Karaman, A. Elwany, R. Arróyave, Hybrid microstructure-defect printability map in laser powder bed fusion additive manufacturing, Computational Materials Science 209 (2022) 111401.

[91] S. Ghosh, N. Ofori-Opoku, J. E. Guyer, Simulation and analysis of γ-Ni cellular growth during laser powder deposition of Ni-based superalloys, Computational Materials Science 144 (2018) 256–264.

[92] L.-E. Rännar, A. Koptyug, J. Olsén, K. Saeidi, Z. Shen, Hierarchical structures of stainless steel 316L manufactured by electron beam melting, Additive Manufacturing 17 (2017) 106–112.

[93] S. Ghosh, M. Mahmoudi, L. Johnson, A. Elwany, R. Arroyave, D. Allaire, Uncertainty analysis of microsegregation during laser powder bed fusion, Modelling and Simulation in Materials Science and Engineering 27 (3) (2019) 034002.

[94] S. Ghosh, R. Seede, J. James, I. Karaman, A. Elwany, D. Allaire, R. Arroyave, Statistical modelling of microsegregation in laser powder-bed fusion, Philosophical Magazine Letters 100 (6) (2020) 271–282.

[95] S. Ghosh, C. K. Newman, M. M. Francois, Tusas: A fully implicit parallel approach for coupled phase-field equations, Journal of Computational Physics 448 (2022) 110734.

[96] J. Kundin, L. Mushongera, H. Emmerich, Phase-field modeling of microstructure formation during rapid solidification in Inconel 718 superalloy, Acta Materialia 95 (2015) 343 – 356.

[97] A. Mullis, J. Rosam, P. Jimack, Solute trapping and the effects of anti-trapping currents on phase-field models of coupled thermo-solutal solidification, Journal of Crystal Growth 312 (11) (2010) 1891–1897.

[98] S. Ghosh, C. K. Newman, M. M. Francois, Tusas: A fully implicit parallel approach for coupled phase-field equations, Journal of Computational Physics 448 (2022) 110734.

[99] J. Ramirez, C. Beckermann, A. Karma, H.-J. Diepers, Phase-field modeling of binary alloy solidification with coupled heat and solute diffusion, Physical Review E 69 (5) (2004) 051607.

[100] Y. Bai, J. R. Mianroodi, Y. Ma, A. K. da Silva, B. Svendsen, D. Raabe, Chemo-mechanical phase-field modeling of iron oxide reduction with hydrogen, Acta Materialia 231 (2022) 117899.

[101] R. Wu, Z. Yue, M. Wang, Effect of initial γ/γ' microstructure on creep of single crystal nickel-based superalloys: A phase-field simulation incorporating dislocation dynamics, Journal of Alloys and Compounds 779 (2019) 326–334.

[102] B. Echebarria, R. Folch, A. Karma, M. Plapp, Quantitative phase-field model of alloy solidification, Physical Review E 70 (6) (2004) 061604.

[103] R. Rojas, T. Takaki, M. Ohno, A phase-field-lattice boltzmann method for modeling motion and growth of a dendrite for binary alloy solidification in the presence of melt convection, Journal of Computational Physics 298 (2015) 29–40.

[104] M. Uddagiri, O. Shchyglo, I. Steinbach, B. Wahlmann, C. Koerner, Phase-field study of the history-effect of remelted microstructures on nucleation during additive manufacturing of ni-based superalloys, Metallurgical and Materials Transactions A 54 (5) (2023) 1825–1842.

[105] M. Tegeler, O. Shchyglo, R. D. Kamachali, A. Monas, I. Steinbach, G. Sutmann, Parallel multiphase field simulations with openphase, Computer physics communications 215 (2017) 173–187.

[106] NVIDIA Corporation, NVIDIA CUDA C programming guide, version 3.2 (2010).

[107] Advanced Micro Devices, Inc., AMD HIP programming guide, publication 1.0 Rev. 1210 (2021).

[108] S. Ghosh, C. K. Newman, GPU-Accelerated Dendritic Solidification Toward Exascale, to be published (2023).

[109] D. Gaston, C. Newman, G. Hansen, D. Lebrun-Grandie, MOOSE: A parallel computational framework for coupled systems of nonlinear equations, Nuclear Engineering and Design 239 (10) (2009) 1768–1778.

[110] MICRESS (The Microstructure Evolution Simulation Software), `https://micress.rwth-aachen.de/` (2019).

[111] OpenPhase, OpenPhase software library for phase-field simulations (2023).
URL `https://openphase.rub.de`

[112] J. E. Guyer, D. Wheeler, J. A. Warren, Fipy: Partial differential equations with python, Computing in Science & Engineering 11 (3) (2009) 6–15.

[113] S. DeWitt, S. Rudraraju, D. Montiel, W. B. Andrews, K. Thornton, PRISMS-PF: A general framework for phase-field modeling with a matrix-free finite element method, npj Computational Materials 6 (29) (2020).

[114] D. Kothe, S. Lee, I. Qualters, Exascale computing in the united states, Computing in Science & Engineering 21 (1) (2018) 17–29.

[115] F. Alexander, et al., Exascale applications: skin in the game, Philos. Trans. R. Soc. A 378 (2166) (2020).

[116] Top500 Project, `https://www.top500.org/` (2022).

[117] Summit, `https://www.olcf.ornl.gov/olcf-resources/compute-systems/summit/`.

[118] Sierra, `https://computing.llnl.gov/computers/sierra/`.

[119] Frontier, `https://www.olcf.ornl.gov/frontier/` (2022).

[120] El capitan, `https://computing.llnl.gov/projects/exascale/` (2022).

[121] Crossroads, `https://www.lanl.gov/projects/crossroads/` (2022).

[122] Exascale computing project, `https://exascaleproject.org/` (2019).

[123] Advanced Scientific Computing Research (ASCR) Program, `https://science.osti.gov/ascr` (2022).

[124] Novel Computational Impact on Theory and Experiment Program, `https://science.osti.gov/ascr/Facilities/Accessing-ASCRFacilities/INCITE/About-incite` (2022).

[125] J. A. Turner, J. Belak, N. Barton, M. Bement, N. Carlson, R. Carson, S. DeWitt, J.-L. Fattebert, N. Hodge, Z. Jibben, et al., ExaAM: Metal additive manufacturing simulation at the fidelity of the microstructure, The International Journal of High Performance Computing Applications 36 (1) (2022) 13–39.

[126] ASM Alloy Phase Diagrams Database, `http://www.asminternational.org/apd/`, P. Villars, editor-in-chief; H. Okamoto and K. Cenzual, section editors, ASM International, Materials Park, OH (2016).

[127] M. Rappaz, J. A. Dantzig, Solidification, EFPL Press, Lausanne, 2009.

[128] P. Mohammadpour, A. Plotkowski, A. B. Phillion, Revisiting solidification microstructure selection maps in the frame of additive manufacturing, Additive Manufacturing 31 (2020) 100936.

[129] J. Hoyt, M. Asta, A. Karma, Atomistic and continuum modeling of dendritic solidification, Materials Science and Engineering: R: Reports 41 (6) (2003) 121 – 163.

[130] Y. Mishin, M. Asta, J. Li, Atomistic modeling of interfaces and their impact on microstructure and properties, Acta Materialia 58 (4) (2010) 1117–1151.

[131] S. Torabi, J. Lowengrub, A. Voigt, S. Wise, A new phase-field model for strongly anisotropic systems, Proceedings of the Royal Society A: Mathematical, Physical and Engineering Sciences 465 (2105) (2009) 1337–1359.

[132] S. Ghosh, A. Karma, M. Plapp, S. Akamatsu, S. Bottin-Rousseau, G. Faivre, Influence of morphological instability on grain boundary trajectory during directional solidification, Acta Materialia 175 (2019) 214–221.

[133] L. Zhang, I. Steinbach, Phase-field model with finite interface dissipation: Extension to multi-component multi-phase alloys, Acta Materialia 60 (6-7) (2012) 2702–2710.

[134] R. Seede, J. Ye, A. Whitt, W. Trehern, A. Elwany, R. Arroyave, I. Karaman, Effect of composition and phase diagram features on printability and microstructure in laser powder bed fusion: Development and comparison of processing maps across alloy systems, Additive Manufacturing 47 (2021) 102258.

[135] P. Jencus, C. Siemers, M. Kopsidis, J. Rösler, Influence of lanthanum addition on the α- β transformation kinetics in the Ti6Al4V alloy, Ti-2007 Science and Technology (2007) 407–410.

[136] G. Knorovsky, M. Cieslak, T. Headley, A. Romig, W. Hammetter, Inconel 718: a solidification diagram, Metallurgical transactions A 20 (10) (1989) 2149–2158.

[137] H. S. Whitewell, L. Li, R. A. Overfelt, Influence of solidification variables on the dendrite arm spacings of Ni-based superalloys, Metallurgical and Materials Transactions B 31B (2000) 546 – 551.

[138] J. D. Hunt, Cellular and primary dendrite spacings, in: Proc. Int. Conf. on Solidification and Casting of Metal (London:The Metal Society), 1979, pp. 3–9.

[139] R. Trivedi, Interdendritic spacing: Part II. A comparison of theory and experiment, Metallurgical and Materials Transactions A 15 (1984) 977–982.

[140] W. Kurz, D. J. Fisher, Dendrite growth at the limit of stability: tip radius and spacing, Acta Metallurgica 29 (1) (1981) 11–20.

[141] D. Ma, P. R. Sham, Primary spacing in directional solidification, Metallurgical and Materials Transactions A 29 (13) (1998) 1113–1119.

[142] P. N. Quested, M. McLean, Solidification morphologies in directionally solidified superalloys, Materials Science and Engineering 65 (1) (1984) 171 – 180.

[143] D. Bouchard, J. S. Kirkaldy, Prediction of dendrite arm spacings in unsteady-and steady-state heat flow of unidirectionally solidified binary alloys, Metallurgical and Materials Transactions B 28 (4) (1997) 651–663.

[144] S. Ghosh, A. Mukherjee, T. Abinandanan, S. Bose, Particles with selective wetting affect spinodal decomposition microstructures, Physical Chemistry Chemical Physics 19 (23) (2017) 15424–15432.

[145] W. Kurz, D. J. Fisher, Fundamentals of Solidification, Trans Tech Publications, Zurich, Switzerland, 1998.

[146] M. J. Aziz, Model for solute redistribution during rapid solidification, Journal of Applied Physics 53 (2) (1982) 1158–1168.

[147] K. A. Jackson, K. M. Beatty, K. A. Gudgel, An analytical model for non-equilibrium segregation during crystallization, Journal of crystal growth 271 (3-4) (2004) 481–494.

[148] S. L. Sobolev, Effects of local non-equilibrium solute diffusion on rapid solidification of alloys, physica status solidi (a) 156 (2) (1996) 293–303.

[149] P. Galenko, Phase-field model with relaxation of the diffusion flux in nonequilibrium solidification of a binary system, Physics Letters A 287 (3-4) (2001) 190–197.

[150] D. Danilov, B. Nestler, Phase-field modelling of solute trapping during rapid solidification of a Si-As alloy, Acta Materialia 54 (18) (2006) 4659 – 4664.

[151] L. Johnson, M. Mahmoudi, B. Zhang, R. Seede, X. Huang, J. T. Maier, H. J. Maier, I. Karaman, A. Elwany, R. Arróyave, Assessing printability maps in additive manufacturing of metal alloys, Acta Materialia 176 (2019) 199–210.

[152] W. Kurz, R. Trivedi, Rapid solidification processing and microstructure formation, Materials Science and Engineering: A 179 (1994) 46–51.

[153] M. Du, W. Wang, X. Zhang, J. Niu, L. Liu, Influence of laser power on microstructure and mechanical properties of laser welded twip steel butted joint, Optics & Laser Technology 149 (2022) 107911.

[154] S. Li, H. Xiao, K. Liu, W. Xiao, Y. Li, X. Han, J. Mazumder, L. Song, Melt-pool motion, temperature variation and dendritic morphology of Inconel 718 during pulsed-and continuous-wave laser additive manufacturing: A comparative study, Materials & design 119 (2017) 351–360.

[155] X. Wang, P. Liu, Y. Ji, Y. Liu, M. Horstemeyer, L. Chen, Investigation on microsegregation of IN718 alloy during additive manufacturing via integrated phase-field and finite-element modeling, Journal of Materials Engineering and Performance 28 (2) (2019) 657–665.

[156] D. Tourret, A. Karma, Growth competition of columnar dendritic grains: A phase-field study, Acta Materialia 82 (2015) 64–83.

[157] R. R. Dehoff, M. Kirka, W. Sames, H. Bilheux, A. Tremsin, L. Lowe, S. Babu, Site specific control of crystallographic grain orientation through electron beam additive manufacturing, Materials Science and Technology 31 (8) (2015) 931–938.

[158] K. Jackson, J. Hunt, Lamellar and rod eutectic growth, in: Dynamics of Curved Fronts, Elsevier, 1988, pp. 363–376.

[159] Q. Lei, B. P. Ramakrishnan, S. Wang, Y. Wang, J. Mazumder, A. Misra, Structural refinement and nanomechanical response of laser remelted Al-Al_2Cu lamellar eutectic, Materials Science and Engineering: A 706 (2017) 115–125.

[160] B. P. Ramakrishnan, Q. Lei, A. Misra, J. Mazumder, Effect of laser surface remelting on the microstructure and properties of Al-Al_2Cu-Si ternary eutectic alloy, Scientific reports 7 (1) (2017) 1–10.

[161] M. Zimmermann, M. Carrard, W. Kurz, Rapid solidification of Al-Cu eutectic alloy by laser remelting, Acta Metallurgica 37 (12) (1989) 3305–3313.

[162] R. Goetzinger, M. Barth, D. Herlach, Mechanism of formation of the anomalous eutectic structure in rapidly solidified Ni-Si, Co-Sb and Ni-Al-Ti alloys, Acta materialia 46 (5) (1998) 1647–1655.

[163] A. Karma, Model of grain refinement in solidification of undercooled melts, International Journal of Non-Equilibrium Processing(UK) 11 (2) (1998) 201–233.

[164] S. Ghosh, M. Plapp, Influence of interphase boundary anisotropy on bulk eutectic solidification microstructures, Acta Materialia 140 (2017) 140 – 148.

[165] S. J. Wang, G. Liu, J. Wang, A. Misra, Characteristic orientation relationships in nanoscale Al-Al_2Cu eutectic, Materials Characterization 142 (2018) 170–178.

[166] S. Akamatsu, S. Bottin-Rousseau, M. Şerefoğlu, G. Faivre, Lamellar eutectic growth with anisotropic interphase boundaries: Experimental study using the rotating directional solidification method, Acta Materialia 60 (6-7) (2012) 3206–3214.

[167] S. Ghosh, A. Choudhury, M. Plapp, S. Bottin-Rousseau, G. Faivre, S. Akamatsu, Interphase anisotropy effects on lamellar eutectics: A numerical study, Physical Review E 91 (2) (2015) 022407.

[168] D. Zhang, A. Prasad, M. J. Bermingham, C. J. Todaro, M. J. Benoit, M. N. Patel, D. Qiu, D. H. StJohn, M. Qian, M. A. Easton, Grain refinement of alloys in fusion-based additive manufacturing processes, Metallurgical and Materials Transactions A 51 (9) (2020) 4341–4359.

[169] P. Barriobero-Vila, J. Gussone, A. Stark, N. Schell, J. Haubrich, G. Requena, Peritectic titanium alloys for 3D printing, Nature communications 9 (1) (2018) 1–9.

[170] D. Wimler, J. Lindemann, M. Reith, A. Kirchner, M. Allen, W. G. Vargas, M. Franke, B. Klöden, T. Weißgärber, V. Güther, et al., Designing advanced intermetallic titanium aluminide alloys for additive manufacturing, Intermetallics 131 (2021) 107109.

[171] W. Zhai, W. Zhou, S. M. L. Nai, Grain refinement of 316L stainless steel through in-situ alloying with Ti in additive manufacturing, Materials Science and Engineering: A 840 (2022) 142912.

[172] J. Zhang, J. Gao, B. Song, L. Zhang, C. Han, C. Cai, K. Zhou, Y. Shi, A novel crack-free Ti-modified Al-Cu-Mg alloy designed for selective laser melting, Additive Manufacturing 38 (2021) 101829.

[173] K. V. Yang, Y. Shi, F. Palm, X. Wu, P. Rometsch, Columnar to equiaxed transition in Al-Mg (-Sc)-Zr alloys produced by selective laser melting, Scripta Materialia 145 (2018) 113–117.

[174] J. R. Croteau, S. Griffiths, M. D. Rossell, C. Leinenbach, C. Kenel, V. Jansen, D. N. Seidman, D. C. Dunand, N. Q. Vo, Microstructure and mechanical properties of Al-Mg-Zr alloys processed by selective laser melting, Acta Materialia 153 (2018) 35–44.

[175] C. Yang, S. Li, X. Wang, J. Wang, H. Huang, Phase-field simulation of multi-phase interactions in Fe-C peritectic solidification, Computational Materials Science 171 (2020) 109220.

[176] L. Thijs, F. Verhaeghe, T. Craeghs, J. Van Humbeeck, J.-P. Kruth, A study of the microstructural evolution during selective laser melting of Ti-6Al-4V, Acta materialia 58 (9) (2010) 3303–3312.

[177] M. Carrard, M. Gremaud, M. Zimmermann, W. Kurz, About the banded structure in rapidly solidified dendritic and eutectic alloys, Acta metallurgica et materialia 40 (5) (1992) 983–996.

[178] H. Müller-Krumbhaar, W. Kurz, E. Brener, Phase transformations in materials, Wiley-VCH Verlag GmbH & Co. KGaA Weinheim, FRG, 2001, Ch. Solidification, pp. 81–170.

[179] K. Ji, E. Dorari, A. J. Clarke, A. Karma, Microstructural pattern formation during far-from-equilibrium alloy solidification, Physical Review Letters 130 (2) (2023) 026203.

[180] N. J. Harrison, I. Todd, K. Mumtaz, Reduction of micro-cracking in nickel superalloys processed by selective laser melting: A fundamental alloy design approach, Acta Materialia 94 (2015) 59–68.

[181] S. Kou, A criterion for cracking during solidification, Acta Materialia 88 (2015) 366–374.

[182] G. Kasperovich, J. Haubrich, J. Gussone, G. Requena, Correlation between porosity and processing parameters in TiAl6V4 produced by selective laser melting, Materials & Design 105 (2016) 160–170.

[183] M. Tang, P. C. Pistorius, J. L. Beuth, Prediction of lack-of-fusion porosity for powder bed fusion, Additive Manufacturing 14 (2017) 39–48.

[184] C. Panwisawas, C. Qiu, M. J. Anderson, Y. Sovani, R. P. Turner, M. M. Attallah, J. W. Brooks, H. C. Basoalto, Mesoscale modelling of selective laser melting: Thermal fluid dynamics and microstructural evolution, Computational Materials Science 126 (2017) 479–490.

[185] C. Qiu, C. Panwisawas, M. Ward, H. C. Basoalto, J. W. Brooks, M. M. Attallah, On the role of melt flow into the surface structure and porosity development during selective laser melting, Acta Materialia 96 (2015) 72–79.

[186] P. Jiang, S. Geng, X. Shao, G. Mi, C. Wang, H. Wu, C. Han, S. Gao, Fine grains reduce cracking susceptibility during solidification: insights from phase-field simulations, JOM 71 (9) (2019) 3223–3229.

[187] L.-X. Lu, N. Sridhar, Y.-W. Zhang, Phase field simulation of powder bed-based additive manufacturing, Acta Materialia 144 (2018) 801–809.

[188] P. Nie, O. Ojo, Z. Li, Numerical modeling of microstructure evolution during laser additive manufacturing of a nickel-based superalloy, Acta Materialia 77 (2014) 85–95.

[189] A. Strondl, R. Fischer, G. Frommeyer, A. Schneider, Investigations of mx and γ'/γ" precipitates in the nickel-based superalloy 718 produced by electron beam melting, Materials Science and Engineering: A 480 (1-2) (2008) 138–147.

[190] E. A. Lass, M. R. Stoudt, M. E. Williams, M. B. Katz, L. E. Levine, T. Q. Phan, T. H. Gnaeupel-Herold, D. S. Ng, Formation of the Ni_3Nb δ-phase in stress-relieved Inconel 625 produced via laser powder-bed fusion additive manufacturing, Metallurgical and Materials Transactions A 48 (11) (2017) 5547–5558.

[191] C. Radhakrishna, K. Prasad Rao, The formation and control of laves phase in superalloy 718 welds, Journal of Materials Science 32 (8) (1997) 1977–1984.

[192] G. Janaki Ram, A. Venugopal Reddy, K. Prasad Rao, G. Madhusudhan Reddy, Control of laves phase in Inconel 718 GTA welds with current pulsing, Science and technology of welding and joining 9 (5) (2004) 390–398.

[193] S. Ghosh, M. R. Stoudt, L. E. Levine, J. E. Guyer, Formation of Nb-rich droplets in laser deposited Ni-matrix microstructures, Scripta Materialia 146 (2018) 36–40.

[194] S.-H. Sun, Y. Koizumi, S. Kurosu, Y.-P. Li, H. Matsumoto, A. Chiba, Build direction dependence of microstructure and high-temperature tensile property of Co–Cr–Mo alloy fabricated by electron beam melting, Acta Materialia 64 (2014) 154–168.

[195] Y. C. Zhang, Z. G. Li, P. L. Nie, Y. X. Wu, Effect of ultrarapid cooling on microstructure of laser cladding IN718 coating, Surface Engineering 29 (6) (2013) 414–418.

[196] M. Alnajjar, F. Christien, K. Wolski, C. Bosch, Evidence of austenite by-passing in a stainless steel obtained from laser melting additive manufacturing, Additive Manufacturing 25 (2019) 187–195.

[197] T. Wang, Y. Zhu, S. Zhang, H. Tang, H. Wang, Grain morphology evolution behavior of titanium alloy components during laser melting deposition additive manufacturing, Journal of Alloys and Compounds 632 (2015) 505–513.

[198] Y. Guo, L. Jia, J. He, S. Zhang, Z. Li, H. Zhang, Interplay between eutectic and dendritic growths dominated by si content for Nb-Si-Ti alloys via rapid solidification, Journal of Manufacturing Science and Engineering 144 (6) (2022).

[199] G. Dinda, A. Dasgupta, S. Bhattacharya, H. Natu, B. Dutta, J. Mazumder, Microstructural characterization of laser-deposited Al 4047 alloy, Metallurgical and Materials Transactions A 44 (5) (2013) 2233–2242.

[200] M. Rafieazad, A. Chatterjee, A. Nasiri, Effects of recycled powder on solidification defects, microstructure, and corrosion properties of DMLS fabricated AlSi10Mg, JOM 71 (9) (2019) 3241–3252.

[201] M. Gäumann, C. Bezencon, P. Canalis, W. Kurz, Single-crystal laser deposition of superalloys: processing–microstructure maps, Acta materialia 49 (6) (2001) 1051–1062.

[202] J. D. Hunt, Steady state columnar and equiaxed growth of dendrites and eutectic, Materials science and engineering 65 (1) (1984) 75–83.

[203] W. Kurz, C. Bezençon, M. Gäumann, Columnar to equiaxed transition in solidification processing, Science and technology of advanced materials 2 (1) (2001) 185.

[204] M. Haines, A. Plotkowski, C. L. Frederick, E. J. Schwalbach, S. S. Babu, A sensitivity analysis of the columnar-to-equiaxed transition for ni-based superalloys in electron beam additive manufacturing, Computational Materials Science 155 (2018) 340–349.

[205] G. Kurtuldu, P. Jarry, M. Rappaz, Influence of cr on the nucleation of primary al and formation of twinned dendrites in al–zn–cr alloys: Can icosahedral solid clusters play a role?, Acta Materialia 61 (19) (2013) 7098–7108.

[206] G. Kurtuldu, A. Sicco, M. Rappaz, Icosahedral quasicrystal-enhanced nucleation of the fcc phase in liquid gold alloys, Acta Materialia 70 (2014) 240–248.

[207] M. Rappaz, P. Jarry, G. Kurtuldu, J. Zollinger, Solidification of metallic alloys: Does the structure of the liquid matter?, Metallurgical and Materials Transactions A 51 (6) (2020) 2651.

[208] I. Cazic, J. Zollinger, S. Mathieu, M. El Kandaoui, P. Plapper, B. Appolaire, New insights into the origin of fine equiaxed microstructures in additively manufactured Inconel 718, Scripta Materialia 195 (2021) 113740.

[209] S. Ghosh, A. Mukherjee, R. Arroyave, J. F. Douglas, Impact of particle arrays on phase separation composition patterns, The Journal of chemical physics 152 (22) (2020) 224902.

[210] J. H. Martin, B. D. Yahata, J. M. Hundley, J. A. Mayer, T. A. Schaedler, T. M. Pollock, 3D printing of high-strength aluminium alloys, Nature 549 (7672) (2017) 365–369.

[211] M. Okugawa, Y. Ohigashi, Y. Furishiro, Y. Koizumi, T. Nakano, Equiaxed grain formation by intrinsic heterogeneous nucleation via rapid heating and cooling in additive manufacturing of aluminum-silicon hypoeutectic alloy, Journal of Alloys and Compounds 919 (2022) 165812.

[212] J. Simmons, Y. Wen, C. Shen, Y. Wang, Microstructural development involving nucleation and growth phenomena simulated with the phase field method, Materials Science and Engineering: A 365 (1-2) (2004) 136–143.

[213] L. Gránásy, G. I. Tóth, J. A. Warren, F. Podmaniczky, G. Tegze, L. Rátkai, T. Pusztai, Phase-field modeling of crystal nucleation in undercooled liquids–a review, Progress in Materials Science 106 (2019) 100569.

[214] W. Wu, D. Montiel, J. E. Guyer, P. W. Voorhees, J. A. Warren, D. Wheeler, L. Gránásy, T. Pusztai, O. G. Heinonen, Phase field benchmark problems for nucleation, Computational Materials Science 193 (2021) 110371.

[215] M. Ode, I. Ohnuma, A thermal fluctuation-based nucleation method for phase-field models, Computational Materials Science 194 (2021) 110448.

[216] N. Wang, N. Smith, N. Provatas, Investigating gas-phase defect formation in late-stage solidification using a novel phase-field crystal alloy model, Physical Review Materials 1 (4) (2017) 043405.

[217] K. R. Elder, N. Provatas, J. Berry, P. Stefanovic, M. Grant, Phase-field crystal modeling and classical density functional theory of freezing, Physical Review B 75 (6) (2007) 064107.

[218] E. Asadi, M. Asle Zaeem, M. I. Baskes, Phase-field crystal model for Fe connected to MEAM molecular dynamics simulations, JOM 66 (3) (2014) 429–436.

[219] M. Guerdane, F. Wendler, D. Danilov, H. Teichler, B. Nestler, Crystal growth and melting in NiZr alloy: Linking phase-field modeling to molecular dynamics simulations, Physical Review B 81 (22) (2010) 224108.

[220] V. C. I. Strutt, B. Jenkins, J. Woolrich, M. Appleton, M. Moody, P. Bagot, Effect of microsegregation and heat treatment on localised γ and γ'compositions in single crystal ni-based superalloys, Journal of Alloys and Compounds 949 (2023) 169861.

[221] C. Dharmendra, K. Rice, B. Amirkhiz, M. Mohammadi, Atom probe tomography study of κ-phases in additively manufactured nickel aluminum bronze in as-built and heat-treated conditions, Materials & Design 202 (2021) 109541.

[222] W. Ren, C. Niu, B. Ding, Y. Zhong, J. Yu, Z. Ren, W. Liu, L. Ren, P. K. Liaw, Improvement in creep life of a nickel-based single-crystal superalloy via composition homogeneity on the multiscales by magnetic-field-assisted directional solidification, Scientific Reports 8 (1) (2018) 1452.

[223] I. Cazic, J. Zollinger, M. Engstler, J. Ghanbaja, T. Schenk, M. El Kandaoui, B. Appolaire, Nucleation burst in additively manufactured Inconel 718: 3D characterization of ISRO-induced equiaxed microstructure, Additive Manufacturing 66 (2023) 103458.

[224] M. Murayama, K. Hono, Three dimensional atom probe analysis of pre-precipitate clustering in an Al-Cu-Mg-Ag alloy, Scripta materialia 38 (8) (1998) 1315–1319.

[225] V. Fallah, N. Ofori-Opoku, J. Stolle, N. Provatas, S. Esmaeili, Simulation of early-stage clustering in ternary metal alloys using the phase-field crystal method, Acta materialia 61 (10) (2013) 3653–3666.

[226] Y. Ji, L. Chen, L.-Q. Chen, Understanding microstructure evolution during additive manufacturing of metallic alloys using phase-field modeling, in: Thermo-mechanical modeling of additive manufacturing, Elsevier, 2018, pp. 93–116.

[227] R. Shi, S. Khairallah, T. W. Heo, M. Rolchigo, J. T. McKeown, M. J. Matthews, Integrated simulation framework for additively manufactured Ti-6Al-4V: melt pool dynamics, microstructure, solid-state phase transformation, and microelastic response, Jom 71 (2019) 3640–3655.

[228] P. Liu, Z. Wang, Y. Xiao, R. A. Lebensohn, Y. Liu, M. F. Horstemeyer, X. Cui, L. Chen, Integration of phase-field model and crystal plasticity for the prediction of process-structure-property relation of additively manufactured metallic materials, International Journal of Plasticity 128 (2020) 102670.

[229] N. Zhou, D. Lv, H. Zhang, D. McAllister, F. Zhang, M. Mills, Y. Wang, Computer simulation of phase transformation and plastic deformation in IN718 superalloy: Microstructural evolution during precipitation, Acta Materialia 65 (2014) 270–286.

[230] D. R. Gunasegaram, A. B. Murphy, A. Barnard, T. DebRoy, M. J. Matthews, L. Ladani, D. Gu, Towards developing multiscale-multiphysics models and their surrogates for digital twins of metal additive manufacturing, Additive Manufacturing 46 (2021) 102089.

[231] T. DebRoy, T. Mukherjee, H. Wei, J. Elmer, J. Milewski, Metallurgy, mechanistic models and machine learning in metal printing, Nature Reviews Materials 6 (1) (2021) 48–68.

[232] N. Johnson, P. Vulimiri, A. To, X. Zhang, C. Brice, B. Kappes, A. Stebner, Invited review: Machine learning for materials developments in metals additive manufacturing, Additive Manufacturing 36 (2020) 101641.

[233] G. James, D. Witten, T. Hastie, R. Tibshirani, An Introduction to Statistical Learning, Springer, New York, 2013.

[234] J. R. Mianroodi, N. H Siboni, D. Raabe, Teaching solid mechanics to artificial intelligence—a fast solver for heterogeneous materials, npj Computational Materials 7 (1) (2021) 1–10.

[235] R. Arróyave, D. L. McDowell, Systems approaches to materials design: past, present, and future, Annual Review of Materials Research 49 (2019) 103–126.

[236] A. Tran, J. A. Mitchell, L. P. Swiler, T. Wildey, An active learning high-throughput microstructure calibration framework for solving inverse structure–process problems in materials informatics, Acta Materialia 194 (2020) 80–92.

[237] J. Fish, G. J. Wagner, S. Keten, Mesoscopic and multiscale modelling in materials, Nature materials 20 (6) (2021) 774–786.

[238] A. Hunter, B. A. Moore, M. Mudunuru, V. Chau, R. Tchoua, C. Nyshadham, S. Karra, D. O'Malley, E. Rougier, H. Viswanathan, et al., Reduced-order modeling through machine learning and graph-theoretic approaches for brittle fracture applications, Computational Materials Science 157 (2019) 87–98.

[239] J. Nieto-Fuentes, S. Osovski, A. Venkert, D. Rittel, Reassessment of the dynamic thermomechanical conversion in metals, Physical Review Letters 123 (25) (2019) 255502.

[240] C. K. Lieou, C. A. Bronkhorst, Thermomechanical conversion in metals: dislocation plasticity model evaluation of the Taylor-Quinney coefficient, Acta Materialia 202 (2021) 170–180.

[241] OOF: Finite Element Analysis of Microstructures, Version 3.2.2, NIST, Gaithersburg, 2019.

[242] A. G. Khachaturyan, Theory of structural transformations in solids, Dover Pubications, Mineola, NY, 2013.

[243] M. Bellet, B. G. Thomas, Ch. 27 Solidification macroprocesses-Thermal-mechanical Modeling of Stress, Distortion and Hot Tearing in Materials Processing Handbook, CRC Press, Taylor and Francis, Boca Raton, FL, 2007.

[244] T. Uehara, M. Fukui, N. Ohno, Phase field simulations of stress distributions in solidification structures, Journal of Crystal Growth 310 (7) (2008) 1331 – 1336.

[245] I. Steinbach, O. Shchyglo, Phase-field modelling of microstructure evolution in solids: Perspectives and challenges, Current Opinion in Solid State and Materials Science 15 (3) (2011) 87 – 92.

[246] X. Tan, Y. Kok, Y. J. Tan, M. Descoins, D. Mangelinck, S. B. Tor, K. F. Leong, C. K. Chua, Graded microstructure and mechanical properties of additive manufactured Ti-6Al-4V via electron beam melting, Acta Materialia 97 (2015) 1–16.

[247] M. Rolchigo, S. T. Reeve, B. Stump, G. L. Knapp, J. Coleman, A. Plotkowski, J. Belak, Exaca: A performance portable exascale cellular automata application for alloy solidification modeling, Computational Materials Science 214 (2022) 111692.

[248] Y. Qin, Y. Bao, S. DeWitt, B. Radhakrishnan, G. Biros, Dendrite-resolved, full-melt-pool phase-field simulations to reveal non-steady-state effects and to test an approximate model, Computational Materials Science 207 (2022) 111262.

[249] S. DeWitt, C. Newman, S. Nichols, J.-L. Fattebert, B. Radhakrishnan, J. Coleman, G. Knapp, J. Belak, J. Turner, Testing analytic models and heuristics for microstructure evolution with 3D, dendrite-resolved phase-field simulations of entire spot melts, TMS, San Diego, CA (2023).

[250] N. Haghdadi, M. Laleh, M. Moyle, S. Primig, Additive manufacturing of steels: a review of achievements and challenges, Journal of Materials Science 56 (1) (2021) 64–107.

[251] J. Günther, F. Brenne, M. Droste, M. Wendler, O. Volkova, H. Biermann, T. Niendorf, Design of novel materials for additive manufacturing-isotropic microstructure and high defect tolerance, Scientific reports 8 (1) (2018) 1298.

[252] C. Tan, Y. Chew, R. Duan, F. Weng, S. Sui, F. L. Ng, Z. Du, G. Bi, Additive manufacturing of multi-scale heterostructured high-strength steels, Materials Research Letters 9 (7) (2021) 291–299.

[253] B. Franco, J. Ma, B. Loveall, G. Tapia, K. Karayagiz, J. Liu, A. Elwany, R. Arroyave, I. Karaman, A sensory material approach for reducing variability in additively manufactured metal parts, Scientific reports 7 (1) (2017) 3604.

[254] A. P. Stebner, G. S. Bigelow, J. Yang, D. P. Shukla, S. M. Saghaian, R. Rogers, A. Garg, H. E. Karaca, Y. Chumlyakov, K. Bhattacharya, et al., Transformation strains and temperatures of a nickel–titanium–hafnium high temperature shape memory alloy, Acta materialia 76 (2014) 40–53.

[255] F. Villaret, X. Boulnat, P. Aubry, J. Zollinger, D. Fabrègue, Y. de Carlan, Modelling of delta ferrite to austenite phase transformation kinetics in martensitic steels: application to rapid cooling in additive manufacturing, Materialia 18 (2021) 101157.

[256] Y. Sun, R. J. Hebert, M. Aindow, Effect of laser scan length on the microstructure of additively manufactured 17-4PH stainless steel thin-walled parts, Additive Manufacturing 35 (2020) 101302.

[257] K. Saeidi, L. Kevetkova, F. Lofaj, Z. Shen, Novel ferritic stainless steel formed by laser melting from duplex stainless steel powder with advanced mechanical properties and high ductility, Materials Science and Engineering: A 665 (2016) 59–65.